Mechanical behaviours of periodic lattices

Huaiyuan Gu

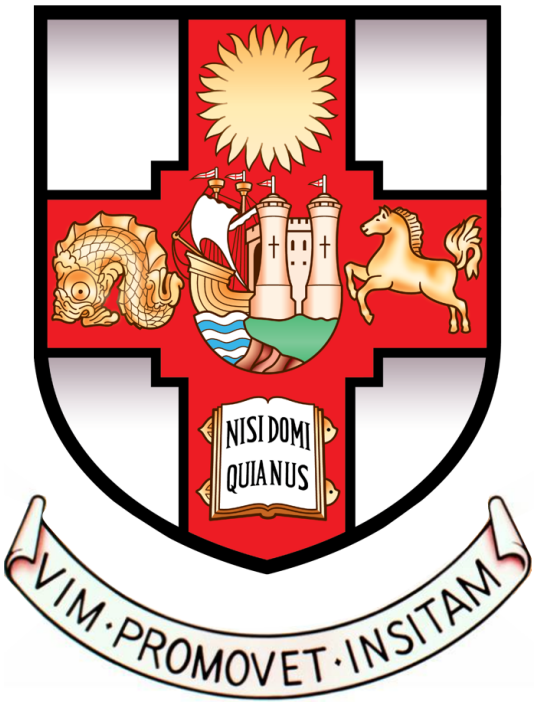

A dissertation submitted to the University of Bristol in accordance with the requirements for award of the degree of Doctor of Philosophy in the Faculty of Engineering

Department of Mechanical Engineering

July 2019

c. 35 000 words

Abstract

This dissertation provide a comprehensive study of the mechanical properties of lattice structures. Two types of topologies were considered including two-dimensional triangular lattice and three-dimensional octet-truss lattice. Prior analytical and numerical studies have shown that the triangular lattice is one of the stiffest geometries of two-dimensional lattices. In this work the modulus, tensile strength and fracture toughness of the lattice have been measured experimentally using the specimens cut from an Aluminium sheet. The dependence of the mechanical properties on the orientation of the lattice has also been revealed. It has been found that the tensile strengths and fracture behaviours vary markedly with the lattice orientation, while the modulus was almost isotropic. A significant property anisotropy was also observed in the octet-truss lattices that its modulus can be varied by 20% and the strength can be double when lattice orientation was changed. The validity of linear elastic fracture mechanics (LEFM) was examined on three-dimensional lattices. It shows that the LEFM can be adequately adopted in the lattices with straight crack fronts, while a curved crack front generates more complexity in the structure configuration ahead of the crack tip, and results in a significant discrepancy in the measured toughness compared to the models with linear crack fronts. Experimentation has been performed to characterise the fracture behaviour of three-dimensional octet-truss lattices manufactured using a Selective Laser Melting(SLM) technique. The fracture toughness and K_R curves have been measured. An increase in fracture resistance was observed during the crack extension. Furthermore the influence of lattice orientation on the fracture behaviour has been illustrated. It shows that a change in orientation will result in a different crack path, but the effect on fracture toughness is small. Numerical approaches were applied to simulate the progressive damage behaviour of the lattices, where a fairly well agreement was achieved between the numerical predictions and experimental measurements.

Acknowledgements

I am very grateful to my academic supervisor Professor Martyn Pavier for his patient guidance, smart advices and great inspiration. I would also like to thank my second supervisor Dr Anton Shterenlikht who offered his generous technical support and constant encouragement throughout my PhD journey.

I would never forget Professor David Smith, my first academic supervisor who guided me through the final year of my undergraduate degree and offered me the PhD position. His untimely death cost me all, I am grateful for the chance to work with him and proud to be his student.

I thank all members of Solid Mechanics Research Group, for providing a great and supportive research environment. The experience of working with my colleagues are unforgeable. A special mention to Dr Andreas Andriotis and Dr Sam Oliver for welcoming me to this group, Dr Charilaos Paraskevoulakos for his assistance in experimental matters.

I acknowledge the tremendous support provided by the Faculty of Engineering technicians at the University of Bristol Ricky Billingham, Rich Bragg, Mike Bracey, Ian Plummer, who manufactured my specimens and experimental apparatus. I would also like to thank Steve Harding, Guy Pearn and Peter Whereat for all the experimental support.

I would like to thank Professor Moataz Attallah and Dr Sheng Li from the Metallurgy and Materials Research group at the University of Birmingham for providing specimens and valuable guidance on the additive manufacturing process.

Last, I extremely grateful for the support from my parents and other family members. They encouraged me undertake the 8 years oversea study and supported me as what they always do. Unfortunately my grandma passed away while I am drafting the dissertation. I hope I made her proud.

Huaiyuan Gu
July 2019

Author's declaration

I declare that the work in this dissertation was carried out in accordance with the requirements of the University's Regulations and Code of Practice for Research Degree Programmes and that it has not been submitted for any other academic award. Except where indicated by specific reference in the text, the work is the candidate's own work. Work done in collaboration with, or with the assistance of, others, is indicated as such. Any views expressed in the dissertation are those of the author.

Signed: Date:

Publications

The following journal papers were based on the work presented in this dissertation:

- Huaiyuan Gu, Martyn Pavier, Anton Shterenlikht, Experimental study of modulus,strength and toughness of 2D triangular lattices, *International Journal of Solids and Structures*, 152-153: 207-216, 2018

- Huaiyuan Gu, Anton Shterenlikht, Martyn Pavier, Brittle fracture of three-dimensional lattice structure, *Engineering Fracture Mechanic, 219, 2019*.

- Huaiyuan Gu, Sheng Li, Martyn Pavier, Moataz M. Attallah, Charilaos Paraskevoulakos, Anton Shterenlikht, (In press), Fracture of three-dimensional lattices manufactured by selective laser melting, *International Journal of Solids and Structures, 180-181: 147-159,2019*.

Additionally, the following manuscript is in preparation for submission:

- Yifan Li, Huaiyuan Gu, Martyn Pavier, Compressive behaviour of three-dimensional lattices under static loading, *Experimental Mechanics*, In preparation.

List of Abbreviations

AWJC	Abrasive Water Jet Cutting
AM	Additive Manufacturing
ASTM	American Society for Testing and Materials
BLA	Boundary Layer Analysis
CT	Compact Tension
CMOD	Crack Mouth Opening Displacement
DIC	Digital Image Correlation
DLF	Direct Laser Fabrication
EDM	Electrical Discharge Machining
EBM	Electron Beam Melting
EIGA	Electrode Induction Melting Gas Atomiser
LEFM	Linear Elastic Fracture Mechanics
SL	StereoLithography
SENT	Single Edge Notch Tension
SENB	Single Edge Notch Bending
SLM	Selective Laser Melting
XCT	X-ray Computed Tomography

List of Latin Characters

a	Crack length
a_0	Initial crack length
a_T	Transition crack length
B	Damage variable
d	Strut diameter
E	Young's modulus
E^*	Effective Young's modulus of lattices
E_s	Young's modulus of strut material
G	Shear rigidity
l	Cell length
K_I	Mode I stress intensity
K_{IC}	Mode I fracture toughness
K_R	Fracture resistance
K_Y	Characteristic toughness
r	Strut radius
r_p	Maximum extent of plastic zone

n	Hardening coefficient
V_m	Crack mouth opening displacement
P	Applied load
P_m	Fracture load
t	Strut thickness
T	T-stress
T_c	Critical T-stress
W	Specimen width
W_s	Work required to create new surface
Z	Nodal connectivity
$f(a/W)$	Dimensionless shape factor

List of Greek Characters

σ_y	Yield stress
σ_f	Failure stress/strength
σ_t	Tensile strength of lattices
σ_b	Buckling stress of lattices
σ_∞	Remote applied stress
α	Normalised model width
β	Unit cell width
γ_s	Surface energy
$\overline{\rho}$	Relative density
ε_y	Yield strain
ε_T	Maximum local tensile strain
v_{xy}, v_{xz}, v_{yz}	Poisson's ratios
ω	Rotation of nodes
θ	Angle of lattice orientation
τ	Shear stress

Contents

List of Figures

List of Tables

Chapter 1

Introduction

1.1 Background

Superior mechanical properties are discovered from natural cellular materials such as woods [8], bamboo[9], honeycombs and bones which are evolved to a carry particular loading condition. For example bamboo and wood exhibit particular high strength along the longitudinal direction to withstand wind [10, 11]. These natural materials exhibit high efficiency, where the required properties can be achieved at a small weight. The improved mechanical performance is achieved by strategical arrangement of components.

Lattice structures are artificial cellular structures inspired by natural materials. The structures are made up by interconnected beams and arranged in periodic manner. Hence, various superior material properties such as high stiffness and strength are able to be obtained at a low density shown in Figure 1.1.

Lattice components are increasingly used in various engineering and medical applications such as bone replacements [12, 13], lightweight multifunctional structures [14, 15, 16, 17]. With advances in modern manufacturing technique, complex geometries are able to be directly fabricated from computer aided design(CAD) models. A wide range of structures may be created with unique properties by manipulating cell configurations, for example auxetic structures[18] which exhibit negative Poisson's ratio.

In recent years, there has been an increasing interest in mechanical performances of lattices such as stiffness, strength, energy absorption, and fracture properties. Analytical and numerical methods are developed aiming for a better prediction of lattice behaviours, and meanwhile seeking for a way to optimise existing structures [19, 20, 21]. However, due to the difficulties in specimen fabrication techniques, not many experimental works have been performed on lattices particularly for fracture. Therefore, a comprehensive study is needed to achieve a better understanding of the accuracy of existing prediction techniques.

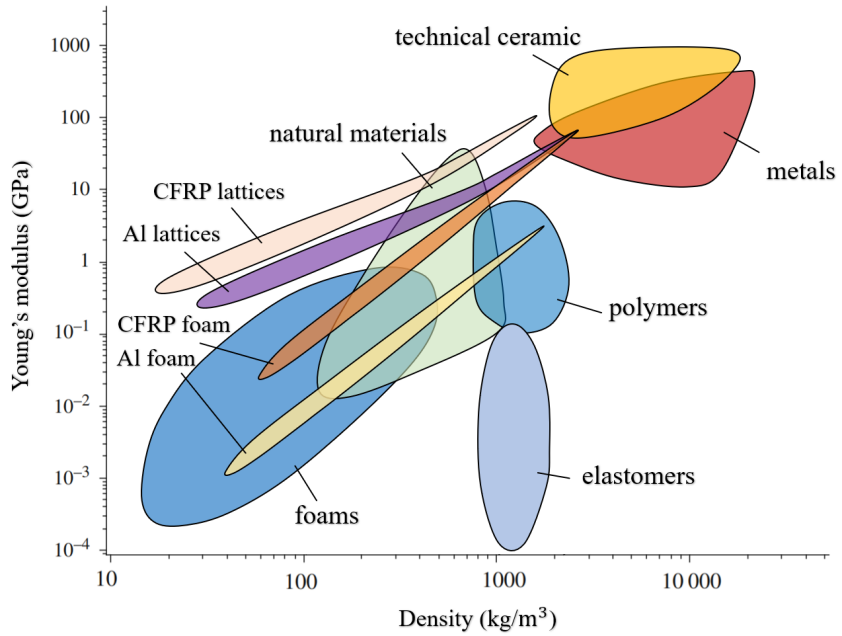

(a)

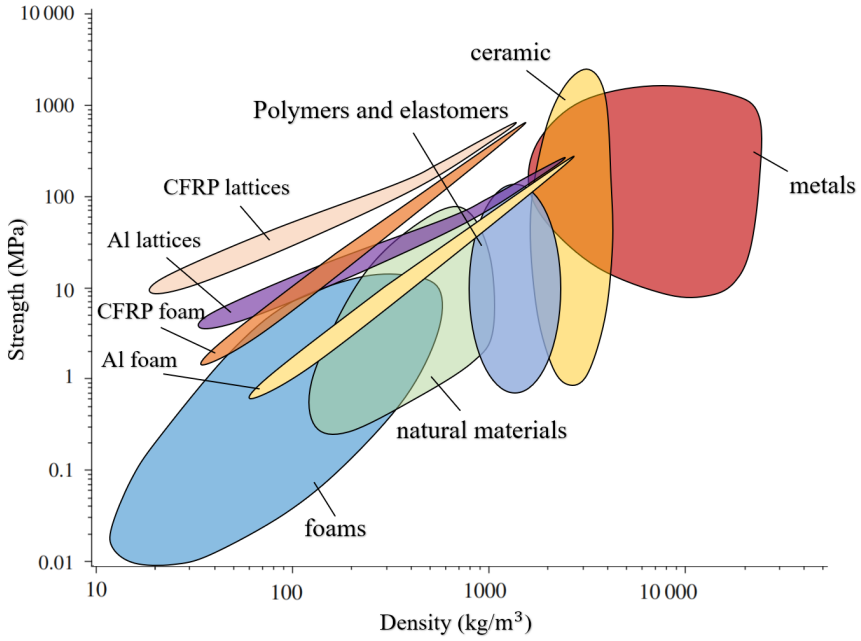

(b)

Figure 1.1: Material property chart for (a) Young's modulus (b) strength. Material values were sourced from [1]

1.2 Thesis outline

Overall, the work presented in this dissertation is to develop a greater understanding of the mechanical properties of lattice structures including modulus, strength and fracture behaviours. This work expands on the outcomes from previous studies on numerical evaluation of lattice properties [5, 3] and provides accurate experimental measurements on two and three-dimensional lattices fabricated though modern manufacturing techniques. There are two main objectives: (i) experimentally determine the mechanical properties of the lattices and assess the validity of the existing prediction techniques including numerical and analytical approaches. (ii) assess the validity of using linear elastic fracture mechanics for predicting fracture strength of lattices.

An overview of the published work in the field of mechanical properties of lattices is provided in Chapter 2. The Chapter presents lattice properties in four aspects including modulus, tensile strength, fracture behaviours and fabrication processes.

An comprehensive study of mechanical behaviours of two-dimensional triangular lattice is presented in Chapter 3. The modulus, strength and fracture toughness are experimentally characterised. The fracture behaviours such as crack paths and load-displacement responses are reported. The significance of lattice orientation is demonstrated to explore the anisotropy of each properties. This study provides a better understanding of the mechanical performances of two-dimensional triangular lattices and reveals the validity of numerical predictions.

In Chapter 4, the properties of the three-dimensional octet-truss lattice is determined including modulus, strength and Poisson's ratio. An analytical approach is provided to derive properties of the lattice, followed by a numerical analysis which is performed to assess the size and orientation effect. Finally, an experiment is presented to validate the accuracy of the numerical predictions.

In Chapter 5, an experimental study is presented to demonstrate fracture behaviours of the octet-truss lattices. This work implements an additive manufacturing technique in the specimen fabrication process. The quality of the specimens in terms of the porosity and dimensional accuracy has been revealed by the results of X-ray computed tomography(XCT). The fracture toughness of the lattice has been measured from different lattice orientations. The crack paths and K_R curves have also been determined experimentally. Finally, conclusions are presented in Chapter 6, where recommendations for future works are also made, based on the outcomes of this thesis.

Chapter 2

Literature review

2.1 Introduction

This chapter introduces a review of previous work on the mechanical properties of both two and three-dimensional lattices including modulus, strength and fracture toughness.

The first section introduces the concept of lattice structures and describes lattice deformation under macroscopic loading. The lattice classification is provided based on the deformation mode of a unit cell. An overview of modulus and strength of lattices is provided next including their scaling relationships with strut dimensions and material properties. The significance of model size and lattice imperfection on their mechanical properties are also considered.

The next section begins with a summary of linear elastic fracture mechanics(LEFM), followed by evaluation of the fracture toughness of brittle two-dimensional lattices. The expression for the fracture toughness is formulated as a function of the relative density and failure strength of the material. Next the criterion for the mixed-mode fracture is revealed using a numerical technique. Then it goes on to the fracture of ductile lattices where the fracture resistance is characterised based on the ultimate tensile strain and yield stress.

A numerical approach is described to assess the validity of using LEFM on two-dimensional lattices. An overview of post-fracture behaviours of lattices is also introduced where crack patterns for different topologies under Mode I loading are presented. The final section describes the fabrication techniques for two and three-dimensional lattices where the limitations of current manufacturing processes are also reported.

2.2 Lattice deformation

A lattice structure is a category of material made by periodic arrangement of beam components typically in a few millimetres. Thereby, it is also known as architectured material or reticular structures. Figure2.1 and 2.2 illustrate several two and three-dimensional lattice topologies and their unit cells. Some unit cell is made of a compound geometry for example unit cell of the kagome lattice is created by a hexagon with 6 triangles distributed on each edge.

When a macroscopic load is applied to such a structure, individual beam component carries bending or axial stress. The macroscopic behaviour of lattice is associated with the stress state and deformation modes of each unit cell. From this point of view, lattice structures offer an opportunity to design macroscopic material properties through a careful manipulation of unit cell configurations. Consequently, useful material properties such as high toughness, high strength, and high energy absorption can be achieved at a very low density.

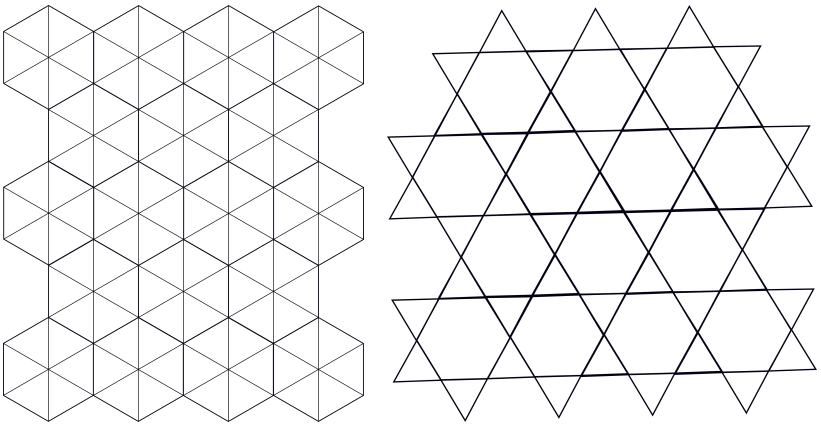

(a) Triangular lattice (b) Kagome lattice

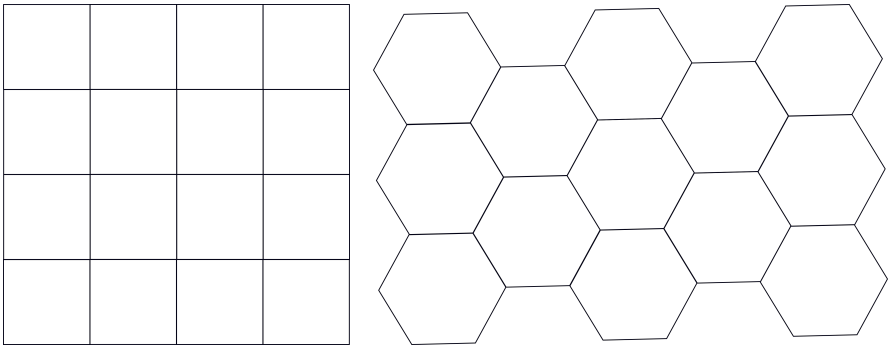

(c) Square lattice (d) Hexagonal lattice

Figure 2.1: Two-dimensional periodic lattices

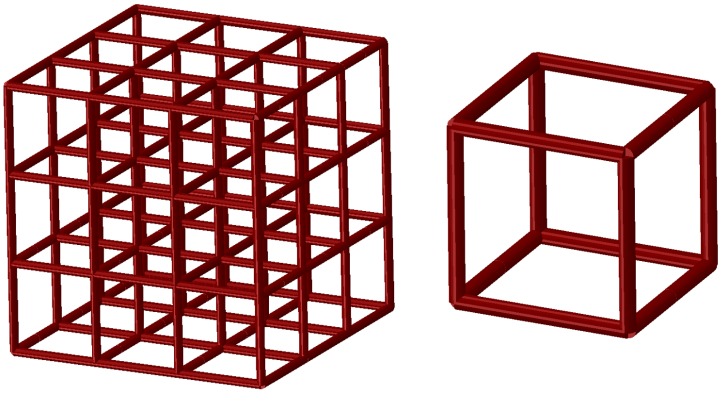

(a) Cubic lattice

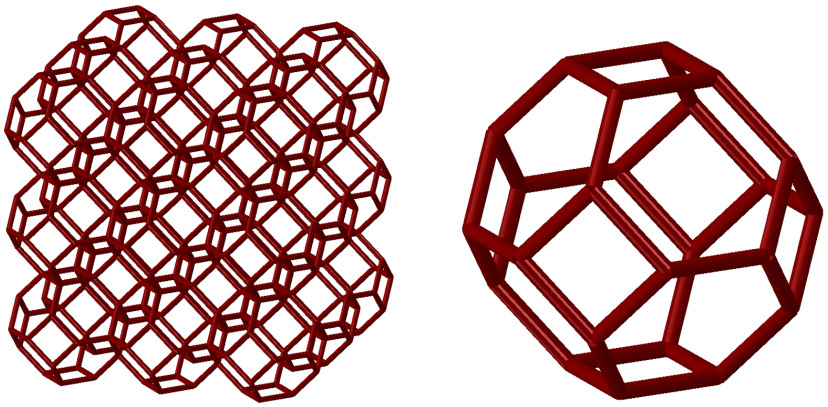

(b) Tetrakaidecadron lattice

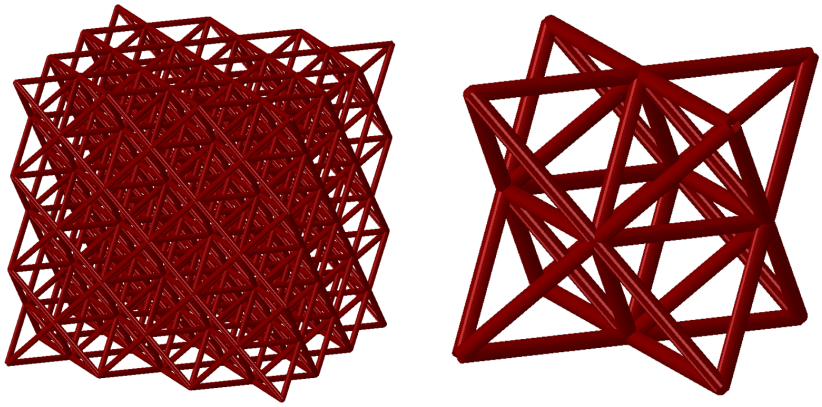

(c) Octet-truss lattice

Figure 2.2: Three-dimensional periodic lattices

Deshpande et al.[22] established the relationship between lattice deformation and nodal connectivity, Z. From their work, lattices are classified based on the strut deformation mode, and consequently two types of lattices are defined including stretch-dominated and bending-dominated topologies. Criterion has been developed to identify the deformation mode of the lattices. The stretch-dominated lattices are rigid structures which are both kinematically and statically determinate, as shown in Figure2.10, while bending-dominated lattices comprise a mechanism and the struts are free to rotate about the joints. Hence, the types of lattice deformation are examined by the Maxwell's criterion. The criteria for two and three-dimensional topologies are expressed as:

$$b = 2j - 3 \tag{2.1}$$

and

$$b = 3j - 6 \tag{2.2}$$

where b is the number of struts and j is the number of nodes. For an infinite periodic structure, the number of struts b can be approximated as:

$$b = Zj/2 \tag{2.3}$$

Hence the condition of rigidity is related to the nodal connectivity Z. Deshpande et al. concludes that $Z = 6$ and $Z = 12$ are the necessary and sufficient condition for two and three-dimensional lattices to be stretch-dominated. Generally, a stretch-dominated lattice offers high stiffness and strength, suggesting a significant benefit for them to be used in lightweight structure applications, while bending dominated structures are more compliant and often be used as an energy-absorber particularly for re-entrant structures[23, 24] which exhibit superior deformability.

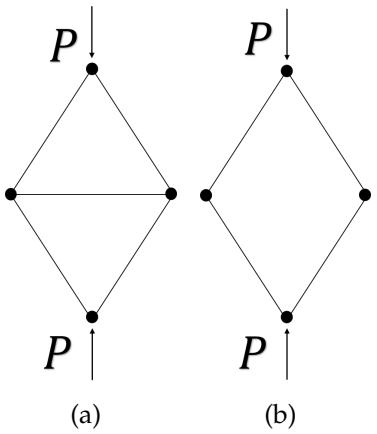

Figure 2.3: (a) Example of a rigid structure and (b) a mechanism

2.3 Lattice modulus and strength

Gibson and Ashby[2] explored mechanical properties of two-dimensional lattices. From their work, the macroscopic properties are analytically derived using beam theory, where each strut behaviour is treated as a Bernoulli-Euler beam. This beam model assumes the plane section always remain as a plane and is perpendicular to the neutral axis before and after deformation, while shear stress is neglected[25]. The mechanical properties of the lattices such as modulus and strength are expressed in terms of strut dimensions and material properties. However these expressions include unknown coefficients which are determined from experiment results. Fleck [5] conducted numerical analysis and expressed the in-plane modulus of two-dimensional isotropic lattices, E^*, as:

$$\frac{E^*}{E_s} = B\overline{\rho}^b \tag{2.4}$$

where E_s is modulus of the material, B and b are constants dependent on lattice topology given in Table 2.1. t and l are the strut thickness and length. The parameter $\overline{\rho}$ is the relative density, which is the ratio between the density of the lattice, ρ^*, and the parent material, ρ_0:

$$\overline{\rho} = \frac{\rho^*}{\rho_0} \tag{2.5}$$

and can be related to strut dimensions as:

$$\overline{\rho} = A\frac{t}{l} \tag{2.6}$$

The exponent b indicates the sensitivity of lattice modulus on the change of relative density, $\overline{\rho}$. It has been noticed that $b = 1$ for stretch-dominated structures i.e. two-dimensional triangular and kagome lattices. Greater value of b is found for bending-dominated structures i.e. hexagonal lattices, as the macroscopic deformation is related to the bending deflection of the struts.

Topology	A	B	b	v	C	c
Hexagonal	$2/\sqrt{3}$	$3/2$	3	1	$1/3$	2
Triangular	$2\sqrt{3}$	$1/3$	1	$1/3$	$1/3$	1
Kagome	$\sqrt{3}$	$1/3$	1	$1/3$	$1/2$	1

Table 2.1: Property coefficients for isotropic lattices [5].

Anisotropy of in-plane modulus of two-dimensional lattices was described in a schematic drawing by Gibson and Ashby[2] shown in Figure2.4. It indicates the modulus of triangular, kagome and hexagonal lattices are isotropic, while the modulus of the square lattice is significantly dependent on lattice orientation; The lattice exhibits high modulus when load applies in the strut direction, and drops dramatically with an increase in angle between the loading and strut directions. For the isotropic lattices, the shear rigidity is expressed as[26]:

$$G = \frac{E^*}{2(1+v)} \tag{2.7}$$

Gurtner[27] analytically derived the existence of a theoretical upper bound for modulus of isotropic lattices based on the principle of minimum potential energy[28]. The predicted result for a two-dimensional lattice topology agreed well with the Hashin-Shtrikman(HS) bound[29], which also coincided with the modulus of two-dimensional triangular lattices. It indicates that for a given density, the triangular lattice is the stiffest topology among two-dimensional structures. The study also provided the prediction of the upper bound for the modulus of three-dimensional lattices:

$$\frac{E^*}{E_s} = \frac{1}{6}\bar{\rho} \tag{2.8}$$

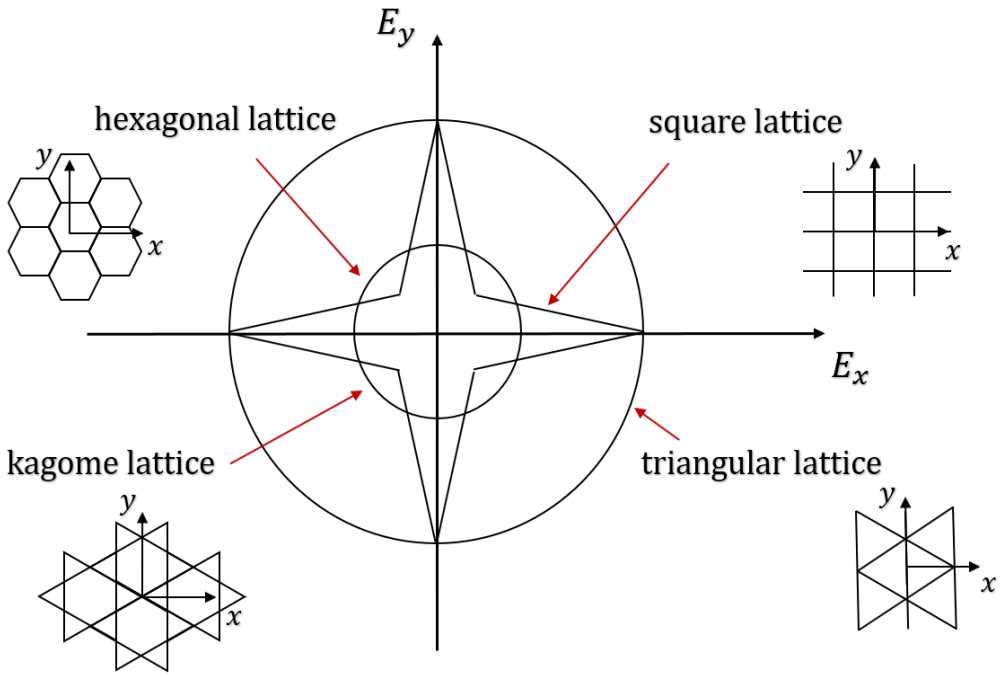

Figure 2.4: Anisotropy of lattice modulus, Reproduced from Gibson and Ashby[2]

The above prediction was found to be significantly lower than the HS upper bound, indicating the theoretical HS upper bound is unreachable for three-dimensional lattices. Deshpande et al.[30] investigated effective properties of an octet-truss lattice, which is a three-dimensional stretch-dominated structure. Its unit cell is shown in the Figure2.2 (c), which is a face-centered cubic cell comprised of an octahedron with 8 tetrahedrons sub cells distributed on its faces. In their work, the compliance tensor of the lattice was explored. A small discrepancy was noticed for the modulus measured from different loading directions. Dejean and Mohr[31] explored conditions for achieving isotropic modulus for a three-dimensional lattice. They suggested that an isotropic modulus could be theoretically achieved by a compound topology combined with a simple cubic, a body-center cubic and a face-centered cubic (octet-truss lattice) cells.

Wang[32] analytically derived in-plane yield strength for two-dimensional periodic lattices under uniaxial loading, by relating the macroscopic applied stress to the maximum axial stress reached in the strut. The lattice strength is reached when the maximum axial stress attained at the material failure stress, σ_f. The general expression for lattice strength, σ^*, is formulated as:

$$\frac{\sigma^*}{\sigma_y} = C\overline{\rho}^c \tag{2.9}$$

where c and C are constants shown in Table 2.1. Note that the strength scales linearly with relative density, $\overline{\rho}$, for stretch-dominated structures such as triangular and kagome lattices. In contrast, the strength of hexagonal lattice scales with $\overline{\rho}^2$. It indicates a stretch-dominated structure exhibit significantly higher strength compared to that of bending-dominated structure particularly at a very low density. The failure mechanism of two-dimensional lattices are analytically explored through a matrix method by Hutchinson and Fleck[33]. Dong et al.[34] measured compressive strength of a three-dimensional octet-truss lattice made with titanium alloy. They expressed the yield strength of the lattice as:

$$\frac{\sigma^*}{\sigma_y} = \frac{1}{3}\overline{\rho} \tag{2.10}$$

This result was found to be comparable to the HS upper bound for an isotropic material[1]. Deshpande et al.[30] performed a numerical analysis to characterise the plastic yielding collapse surfaces of the octet-truss lattice, where the yield strength was evaluated for the lattice under different loading conditions. An anisotropic yield criterion was proposed in this study to describe the yielding of the lattice subjected to a compressive loading.

The use of three-dimensional lattices as core material for sandwich structure has been studied extensively. Wicks and Hutchinson[16] reveals that an optimised truss core panels are superior for taking bending and compressive load, and are more weight efficient compared to honeycomb core sandwich panels. Lee et al.[35] experimentally characterised both static and dynamic compressive behaviours of a pyramid truss core where an excellent compressive strength was measured at a low density. A fabrication technique for titianium matrix composite lattices was developed by Moongkhamklang et al.[36]. They showed that the lattice created in their study exhibited the highest specific strength and stiffness compared to other existing three-dimensional lattices used in practice.

Meza et al.[37] introduced a method to extend the property space of lattices by making lattices with hollow struts. The work illustrated the difference in mechanical behaviours of hollow-beam lattices compared to that of solid beam lattices and revealed their complex parameter space. A recent study optimised mechanical properties of lattices by replicating micro-scale structure of crystalline materials [38]. The lattice was created by a combination of different types of unit cells and arranged in multiple orientations to tailor compressive behaviours such as strength, hardening coefficient and damage paths.

From much of published works, the theoretical predictions of lattice properties were based on the assumption that all unit cells are subjected to an identical stress state. This assumption is inadequate for finite grid where boundary effects are not negligible, for example kagome lattices exhibit significant compliant mode at its boundary compared to the cells at the center[39]. Onck [40] investigated the influence of reducing model size on the mechanical properties of lattices. In his work, the two-dimensional hexagonal lattices were created with different width, W shown in Figure 2.3. A uniform compressive load was applied to each model to evaluate their modulus and strength. The study reveals that the modulus and compressive strength of the lattice reduces with model width, W, caused by the highly compliant structure of the two free edges. These conclusions are illustrated through an experimental study performed by Andrews et al. [41].

The influence of imperfection on lattice properties was considered in the literature including missing struts, fractured struts, stochastic dispersion of nodes and rigid inclusions. Symons [26] reveals that these imperfections result in a significant reduction in modulus particularly for the lattices with low nodal connectivity, Z, such as kagome and hexagonal lattices, while the influence is small for triangular lattices. Chen[42] discussed the knock-down in yield strength caused by imperfection in lattices, and reported that the fractured strut produced the largest knock-down effect compared to other imperfection types.

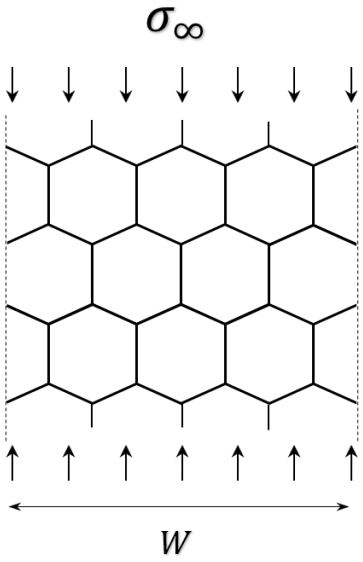

Figure 2.5: Two-dimensional hexagonal lattices model under uniform compressive load.

2.4 Fracture of lattice structures

2.4.1 Linear elastic fracture mechanics

Griffith [43] introduced concept of thermodynamics system to a cracked body, where energy balance equation was applied. The strain energy released for an incremental crack extension is balanced with work required to create new surface,W_s.

$$-\frac{d\prod}{dA} = \frac{dW_s}{dA} \tag{2.11}$$

Where the $\prod$ is the potential energy supplied by the internal strain energy and external force. Based on stress analysis of Inglis [44], Griffith expressed the strength of a centre cracked body with crack length,a, as:

$$\sigma_f = (\frac{\pi E \gamma_s}{2(1-v^2)a})^{1/2} \tag{2.12}$$

Where γ_s is the surface energy of the material. Based on works of Irwin, Westergaard and Williams [45, 46, 47], a closed-form expression of stress state at the crack tip was derived for an isotropic and elastic solid:

$$\sigma_{ij} = (\frac{K}{\sqrt{r}}) f_{ij}(\theta) + \sum_{m=0}^{\infty} A_m r^{m/2} g_{ij}^{(m)}(\theta) \tag{2.13}$$

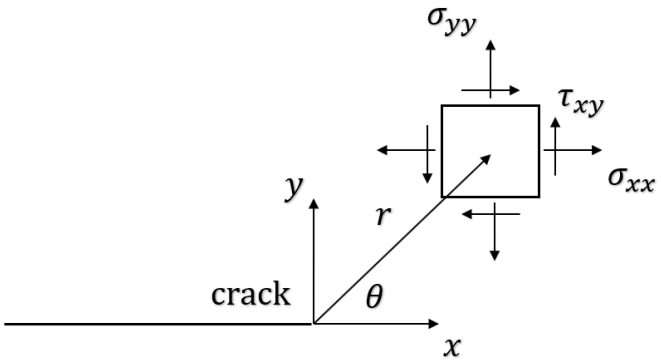

Figure 2.6: crack tip stress tensor

The K was a constant known as the stress intensity factor [48], which can be expressed in a form of:

$$K = \sigma\sqrt{\pi a} f(a/W) \tag{2.14}$$

The σ is the stress applied on the cracked body and the $f(a/W)$ is a non-dimensional geometry factor given in the previous work [49]. For the higher-order terms, the A_m is a constant and g_{ij} is a dimensionless factor depending on θ. As r approaches to 0, the leading term is infinity, and becomes dominant in comparison with the higher-order term. However, the influence of the higher-order term was found to be significant under Mode II and III fracture or mixed Mode loading conditions [50].

2.4.2 Fracture toughness

Gibson and Ashby[2] provided an analytical approach to derive the Mode I fracture toughness, K_{IC}, of brittle hexagonal lattices. In their analytical model, an infinite centre-cracked lattice plate was subjected to a remote applied stress, σ_{22}, as shown in Figure 2.4.2. The applied stress intensity factor, K_I, was related to the axial stress, σ_s, in the most heavily loaded strut (strut A) through the linear elastic fracture mechanics(LEFM) and beam theory:

$$\frac{\sigma_{22}}{\sigma_s} = C_1\sqrt{\frac{l}{a}}(\frac{t}{l})^2 \tag{2.15}$$

The fracture toughness, K_{IC},was then calculated by substituting the axial stress, σ_s, into the material failure stress, σ_f:

$$K_{IC} = C_2\sigma_f\sqrt{\pi l}(\frac{t}{l})^2 \tag{2.16}$$

where C_1 and C_2 are coefficients determined from experiment. The same approach was adopted by Fleck and Qiu[5] to derive the fracture toughness of two-dimensional triangular lattices, where a similar form of expression was deduced:

$$K_{IC} = 0.337\bar{\rho}\sigma_f\sqrt{l} \tag{2.17}$$

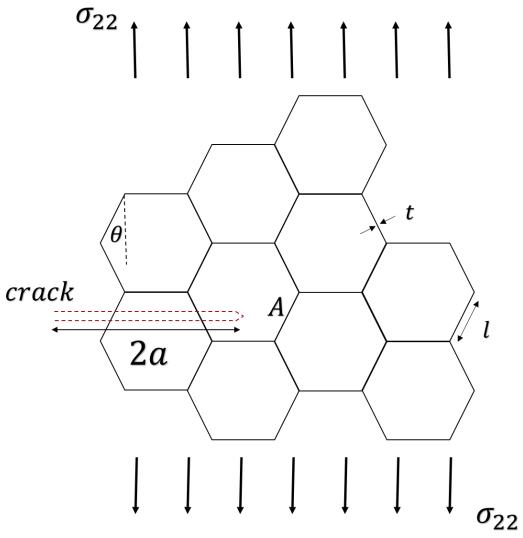

Figure 2.7: Hexagonal lattice subjected to remote tensile load

Huang and Lin[51] derived a criterion for mixed-mode fracture of brittle two-dimensional lattices subjected to a combination of uniform tensile and shear stress. The axial stress in the most heavily loaded strut was analytically related to applied K_I and K_{II} through a linear superposition principle. They expressed the fracture criterion as:

$$\frac{K_I}{K_{IC}} + \frac{K_{II}}{K_{IIC}} = 1 \tag{2.18}$$

Schmidt and Fleck[52] reported a numerical approach to evaluate the fracture toughness of two-dimensional lattices known as boundary layer analysis(BLA). The physics of the method was similar to the analytical method. In this method, a K-controlled stress field is created and the axial stress of the most heavily loaded strut is directly evaluated for a given stress intensity value,K. This is achieved through a large circular lattice model with prescribed nodal displacements and rotations on the outer boundary according

to the asymptotic field:

$$
\begin{aligned}
u_1 &= \frac{1}{2\sqrt{\pi}}\frac{K_I}{G}r^{1/2}(k-cos\theta)cos\frac{\theta}{2} + \frac{1}{2\sqrt{\pi}}\frac{K_{II}}{G}r^{1/2}(k+2+cos\theta)sin\frac{\theta}{2} \\
u_2 &= \frac{1}{2\sqrt{\pi}}\frac{K_I}{G}r^{1/2}(k-cos\theta)sin\frac{\theta}{2} - \frac{1}{2\sqrt{\pi}}\frac{K_{II}}{G}r^{1/2}(k-2+cos\theta)cos\frac{\theta}{2} \\
\omega &= \frac{1}{2}(\frac{\partial u_2}{\partial x} - \frac{\partial u_1}{\partial y})
\end{aligned}
\tag{2.19}
$$

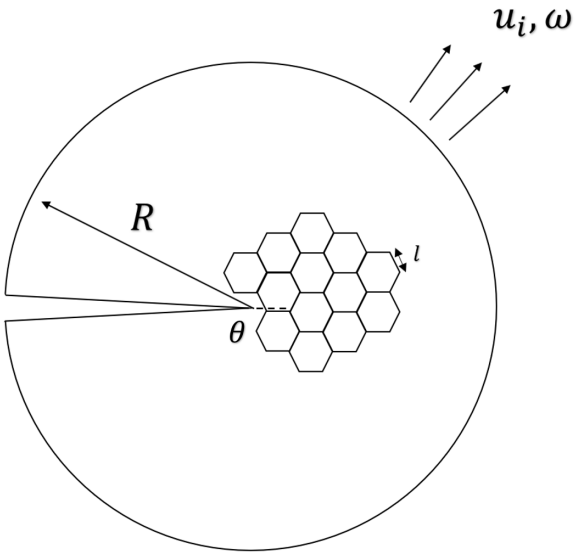

Figure 2.8: Lattice boundary layer model

where ω is the in-plane rotation and $k = (3-v)/(1+v)$. G is the shear rigidity of the lattices obtained from the Eqn.2.7. Fleck[3] introduced two types of criteria for strut failure : (i) maximum tensile strain criterion and (ii) average tensile strain criterion. The former criterion assumes that strut failure occur when the maximum tensile strain within the strut attained the material failure strain. The later criterion dictates the failure based on the mean tensile strain across the strut section. The strut is considered to be failed when the mean tensile strain across the beam section reaches to the failure strain. The study suggests that the first criterion is suitable for characterising the failure of brittle struts, while the second one is more adequate for the failure of ductile struts where the strut rupture involves a significant necking behaviour. The fracture toughness, K_{IC}, was found when the failure condition was reached at the most heavily loaded strut. The general scaling relation for fracture toughness of lattices, relative density and failure stress

was expressed as:

$$\frac{K_{IC}}{\sigma_f \sqrt{l}} = D(\overline{\rho})^d \tag{2.20}$$

D and d are constants depending on topology, as shown in Table 2.2. The exponent d shows the sensitivity of fracture toughness to the change of relative density. For kagome lattices, the d was equal to 0.5 indicating the fracture toughness is less affected by the change of relative density. In contrast to the kagome lattices, the toughness of hexagonal lattices degrade rapidly with the reduction of relative density.

Fleck and Qiu [5] adopted the BLA method to explore the mixed-mode fracture criterion for isotropic two-dimensional lattices. Figure 2.9 shows the evaluated failure locus, where the label indicates the location of the maximum axial stress under different combinations of K_I and K_{II} shown in Figure 2.10.

Topology	D (Mode I)	D (Mode II)	d for both modes
Hexagonal	0.80	0.37	2
Triangular	0.50	0.38	1
Kagome	0.212	0.133	0.5

Table 2.2: The coefficient for lattice fracture toughness [5]

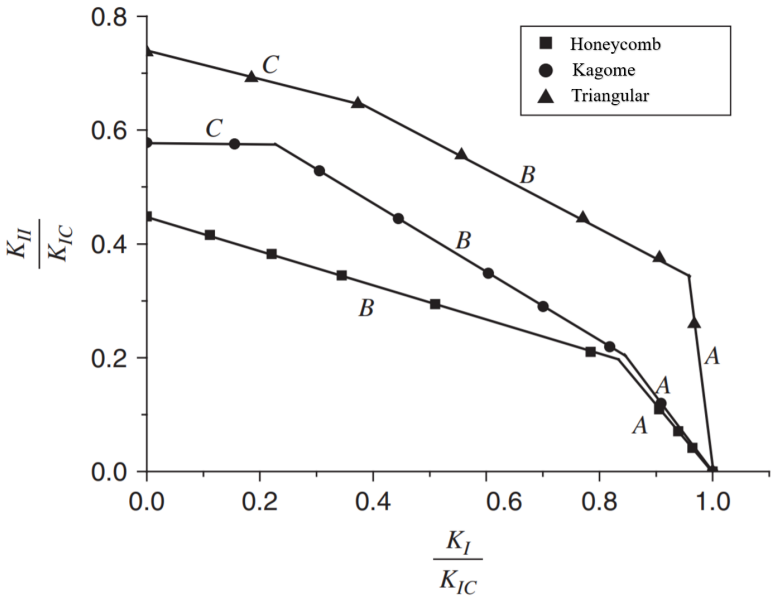

Figure 2.9: Mixed-mode fracture curve for two-dimensional lattices.[3]

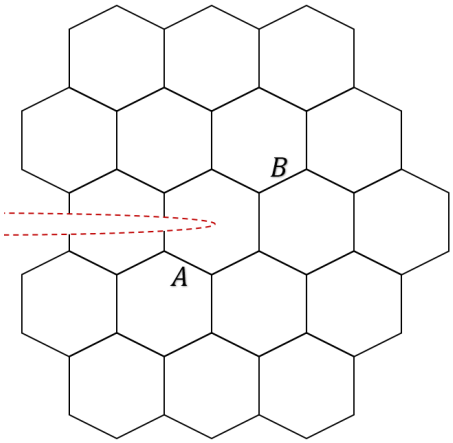

(a) Hexagonal lattice

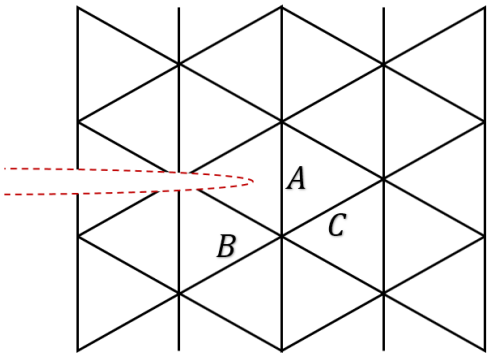

(b) Triangular lattice

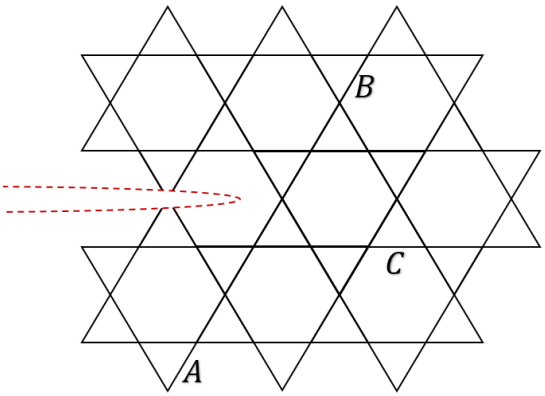

(c) Kagome lattice

Figure 2.10: Crack tip structures for two-dimensional lattices

The toughness of an elastic-plastic honeycomb was employed by Schmidt and Fleck[53] using the BLA method based on the assumption of small scale yielding. A simple estimation of the fracture toughness for the ductile lattice was given as:

$$K_C = \frac{\sigma_f}{\sigma_y} K_Y \tag{2.21}$$

where σ_y is the material yield strength, σ_f is the material failure stress, K_Y is the characteristic toughness at which cause struts start to yield. The linear scaling between K_C, and $\frac{\sigma_f}{\sigma_y}$ was illustrated in the study using a set of FE analyses. The FE results also reveal that the decrease in material hardening leads to an increase in fracture toughness. This is because the reduction of material hardening results in a larger deformation at the crack tip for achieving the failure strength. A more sophisticated expression of fracture toughness of ductile lattices was characterised by Tankasala et al.[3] using a comprehensive FE simulations. The material properties were modelled using Ramberg-Osgood relations:

$$\frac{\varepsilon}{\varepsilon_y} = \frac{\sigma}{\sigma_y} + \alpha(\frac{\sigma}{\sigma_y})^n \tag{2.22}$$

ε_y and σ_y are the yield strain and strength. α and n are coefficients describing the hardening behaviour of the material. The study related the axial strain in the first strut at the crack tip to the applied stress intensity factor based on the HRR singularity for a small strain solution:

$$\varepsilon_T \propto K^{\frac{2n}{n+1}} \tag{2.23}$$

ε_T is the maximum local tensile strain and K is the applied stress intensity. Based on the outcome of fracture toughness of brittle lattices, Eqn.2.20, a modified expression was deduced for ductile lattices:

$$K_C = D\overline{\rho}^d(\frac{\varepsilon_T}{\varepsilon_Y})^{\frac{n+1}{2n}}\sigma_Y\sqrt{l} \tag{2.24}$$

ε_Y and σ_Y are the yield stain and strength, n is the strain hardening exponent. The solution was numerically confirmed for n ranging from 1 to 500. The study also investigated the size and shape of the plastic zone for two-dimensional lattices shown in Figure 2.11. It shows that each plastic zone contained two lobes, one pointing forward and one pointing backward. For isotropic topologies such as triangular and kagome lattices, the shape of the plastic zones are similar to that of a solid material, while for diamond lattice, the shape of the plastic zone exhibited strong orientation dependency, where two elongated lobes were orientated along the strut directions.

It was also found that the shape of plastic zone was insensitive to the change of material properties. The size of plastic zone was characterised by r_P, defined as the maximum extent of plastic zone from the crack tip, which was related to the applied stress intensity factor, K, by:

$$r_P = \alpha_1 (\frac{K}{\sigma_Y})^2 \tag{2.25}$$

where α is a constant depending on the lattice topology. Masta et al.[4] performed an experimental study to explore fracture properties of three-dimensional octet-truss lattices made from high strength titanium alloy. A series of three-point bending tests was conducted for single edge notched bend (SENB) specimens defined by ASTM standard E1820 [54]. The specimens were fabricated using snap-fit and vacuum brazing methods.

The toughness was measured from specimens created with different relative densities, $\overline{\rho}$, ranging from 8% to 19%, corresponding to the measured toughness ranged from 2 MPa$\sqrt{m}$ to 14 MPa$\sqrt{m}$. The study reported that the Titanium octet-truss lattices exhibit the highest combination of strength and toughness compared to other materials at a similar density such as woods. The study also revealed that the fracture toughness of scales linearly with relative density, $\overline{\rho}$, and the square root of strut length, $\sqrt{l}$:

$$K_{IC} = 0.45 \overline{\rho} \sigma_f \sqrt{l} \tag{2.26}$$

During the crack growth, visible strut failure was noticed around the node-truss joint, and micro-cracks were also formed within the braze material. The study suggests that the multiple failure locations contributed to a crack tip shielding mechanism and resulted in an increase in the fracture toughness. Furthermore, R-curve was evaluated based on the measured fracture load, where an increase in fracture resistance was observed with increasing crack length. Masta et al. suggested that the rising R-curve was mainly attributed to the energy dissipation caused by the significant plastic deformation at the joints, particularly for lattices with a high relative density, $\overline{\rho}$, where the volume of the joints were large.

Romijin [55] investigated the effect of lattice imperfections on fracture toughness using two-dimensional lattices. He concluded that the knock-down effect on fracture toughness was significant for lattices with intermediate nodal connectivity, Z, such as kagome and square lattices ($Z = 4$), due to the change of deformation mode from stretching to bending. For lattices with either low or high nodal connectivity, Z, such as hexagonal ($Z = 3$) and triangular lattices ($Z = 6$), the toughness is less affected.

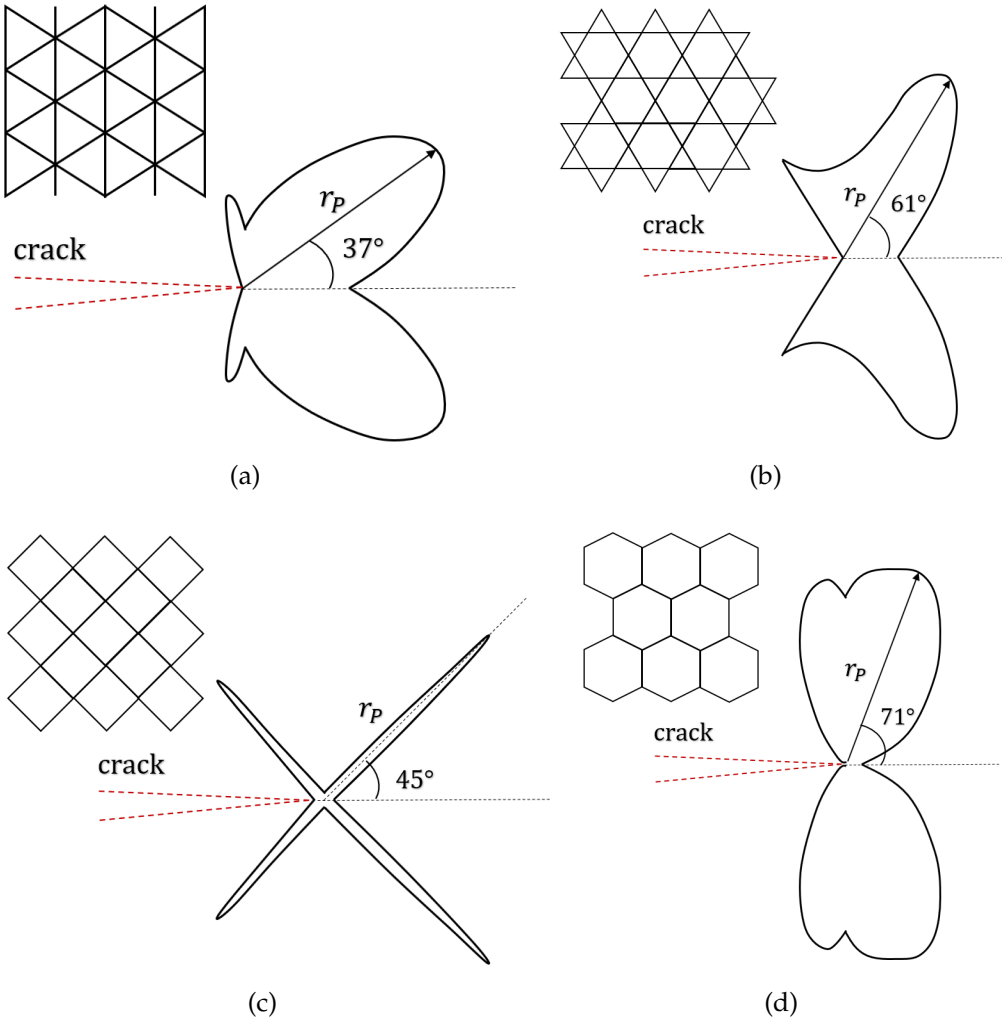

Figure 2.11: Schematic drawing of plastic zone of two-dimensional lattices under Mode I loading: (a) triangular lattice (b)kagome lattice (c) diamond lattice (d) hexagonal lattice. Reproduced from Masta[4]

2.4.3 Strength of cracked lattices

Fleck[5] demonstrated the use of LEFM for predicting fracture strength of two-dimensional isotropic lattices including triangular, hexagonal and kagome lattices. Fleck created a large centre-cracked lattice model and evaluated the fracture strength based on the stress state of the most heavily loaded strut at the crack tip. The results were compared to the prediction of LEFM technique based on the Mode I and Mode II fracture toughness obtained from the Eqn.2.20 :

$$K_{IC} = \sigma_c \sqrt{\pi a} \sqrt{sec(\frac{\pi}{2}\frac{a}{w})} \tag{2.27}$$

and:

$$K_{IIC} = \tau_c \sqrt{\pi a} \sqrt{sec(\frac{\pi}{2}\frac{a}{w})} \tag{2.28}$$

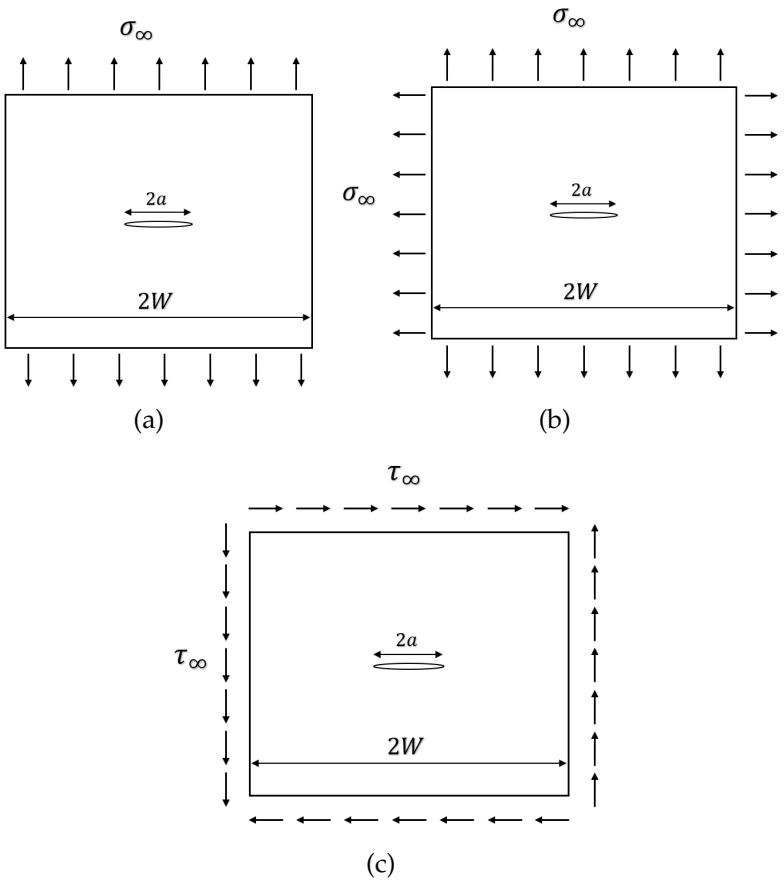

Figure 2.12: Center cracked model subjected to different loading conditions: (a)uniaxial (b) biaxial (c) shear

The study revealed that the fracture strength of lattices is adequately characterised using LEFM for large crack sizes. When the crack size is of the order of the cell size, the fracture strength is close to the unnotched strength due to the small stress concentration at the crack tip for lattices, as shown in Figure 2.13. For uniaxial loading, the FE evaluated fracture strength was found to be lower than the LEFM predictions, while this discrepancy was smaller for the condition of biaxial tension. Fleck et al. interpreted this phenomenon as a consequence of T-stress. A significant negative T-stress exhibited in the centre-cracked model resulted in an increase in axial stress at the crack tip leading to a reduction of the fracture strength. Under the condition of biaxial tension, a horizontal tensile load was imposed on the model in the same magnitude as the vertical loading, the net T-stress is close to zero leading to a better accuracy of the LEFM predictions. By conducting the analysis with different magnitude of horizontal tensile stress, the influence of T-stress on the axial stress at the crack tip was characterised as a function of the relative density:

$$\sigma_s = -A_1 \frac{T}{\bar{\rho}^{B_1}} \tag{2.29}$$

A_1 and B_1 are constants depending on lattice topologies. $B_1 = 1$ was found for stretch-dominated structures including triangular and kagome lattices. A greater value of B was found for hexagonal lattices, where the strut bending is significant.

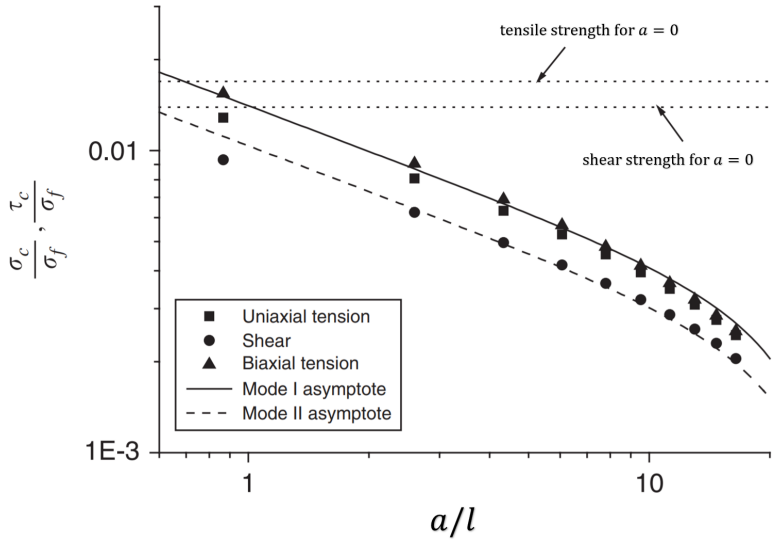

Figure 2.13: Comparison of FE evaluated fracture strength and LEFM prediction for triangular lattice. Reproduced from [5].

A transition crack size, a_T, was introduced such that for $a > a_T$, the fracture strength can be reasonably determined by LEFM, while for $a < a_T$, the fracture strength can be approximated using the tensile strength of unnotched lattices. Fleck et al. expressed the transition crack size for two-dimensional isotropic lattices as:

$$a_T = \frac{1}{\pi}\frac{K_{IC}}{\sigma_t} \tag{2.30}$$

Alonso and Fleck[56] performed a similar numerical analysis to evaluate the strength of cracked anisotropic square lattices, and assess the validity of using LEFM. A very similar conclusion was reached compared to that for the isotropic lattices that the LEFM can only be used when the crack size is much exceed to the cell size. A series of three-point bending fracture tests were carried out to experimentally determine the transition crack size, a_T of the square lattices, and hence to identify the strength-controlled and toughness-controlled regimes, as shown in Figure 2.14. From their work, the transition crack length of the square lattices is expressed as:

$$a_T = 0.14\frac{l^3}{t^2} \tag{2.31}$$

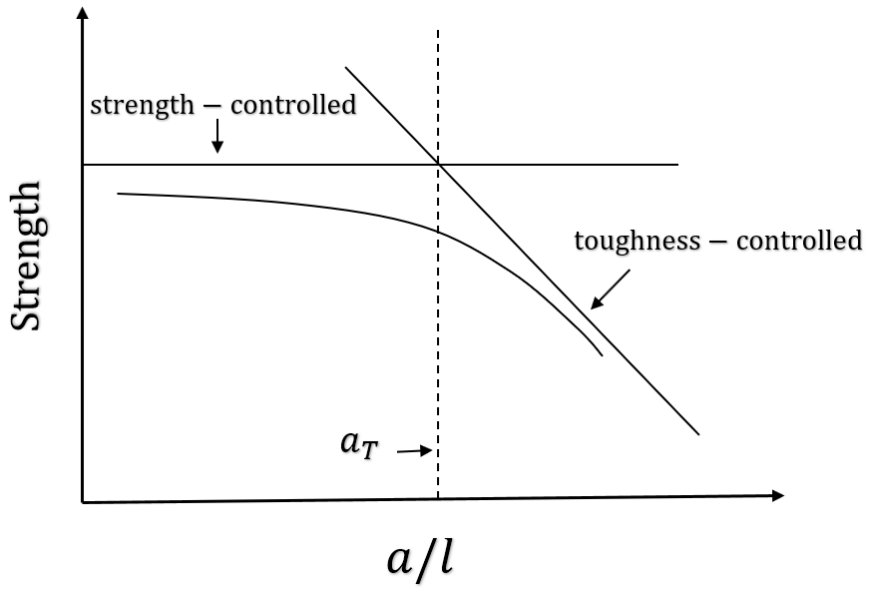

Figure 2.14: Schematic drawing for strength and toughness-controlled fracture strength of square lattices. Reproduced from[6]

2.4.4 Crack growth simulation

Cui et al.[7] simulated the crack propagation in two-dimensional ductile lattices under Mode I loading. The strut material property was characterised using Johnson-Cook model, where the yield criterion was expressed as:

$$\sigma_Y = (A + B\varepsilon_p^n)[1 + C\ln(\frac{\dot{\varepsilon_p}}{\dot{\varepsilon_0}})](1 - T_H^m) \tag{2.32}$$

where A is the material yield strength, B is the strain hardening constant, C is strengthening coefficient for the strain rate, n is the hardening coefficient and m is the thermal coefficient. The strut behaviour was modelled using Timoshenko beam element with linear interpolation functions. Element deletion algorithm was triggered when failure condition was met. From the work of Cui et al. the models were subjected to different strain rate ranging from 10 s^{-1} to 1000 s^{-1}. It was found that the material softening behaviour was only observed at strain rate of 10 s^{-1}. No softenning behaviour was found under a high strain rate, and the applied stress rapidly dropped down to zero when the failure condition was reached at the crack tip.

Various crack patterns were observed from different lattice topologies including hexagonal, triangular and kagome lattices. For a centre-crack model, triangular lattices exhibited an X-type crack pattern after crack initiation, while the Butterfly-type, Petal-type crack patterns were observed from hexagonal lattices with different initial flaw types, as shown in Figure 2.15.

Schmidt and Fleck[53] modelled crack growth in a ductile hexagonal lattice under a static loading. Compared the work of Cui et al. a different element deletion technique was adopted. The element attained failure condition were firstly replaced with axial and transverse forces, which were then ramped down to zero over the loading step. This work demonstrated a tortuous crack path for hexagonal lattices under Mode I loading. Furthermore, fracture resistance was computed after each increment of crack extension. An increase in fracture resistance was observed due to the growing plastic zone.

An alternative numerical approach was introduced by Lipperman and Ryvkin[57] to predict crack path of brittle two-dimensional lattices. In such approach, the stress field of an unbounded infinite lattice was calculated using a combined structural variation and representative cell method[58], by which the location of the maximum stress was determined. It shows that under a remote uniaxial tensile load, the crack paths of triangular and kagome lattice aligned perpendicularly to the load, while for hexagonal lattice, the crack inclined at 30° to the loading direction.

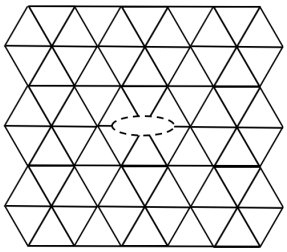

Initial crack pattern

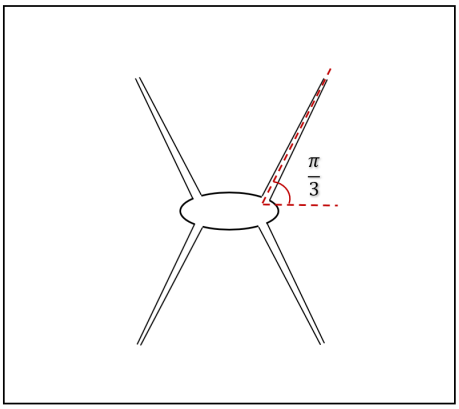

(a) X-type

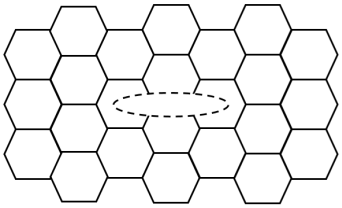

Initial crack pattern

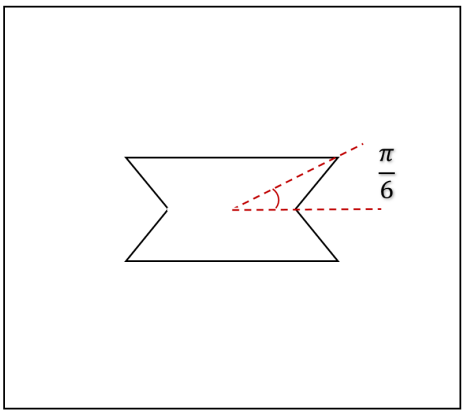

(b) Butterfly-type

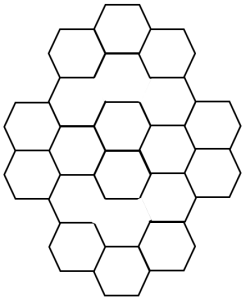

Initial crack pattern

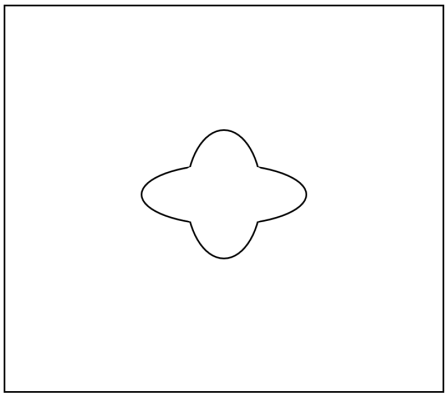

(c) Petal-type

Figure 2.15: FE predicted crack pattern for two-dimensional topologies: (a) triangular lattices (b) hexagonal lattice with vacancy defect (c) hexagonal lattice with rigid inclusion. Reproduced from Cui et al.[7]

2.5 Lattice fabrication

This section provide a review of fabrication techniques of producing lattice structures. Two-dimensional honeycombs are often fabricated using bonding techniques including expansion and corrugation methods[59]. For the expansion method, metal sheets are firstly bonded by strips of adhesive applied at specific locations. The bonded sheets are then expanded to form a honeycomb geometry, as shown in Figure 2.16(a). For the corrugation method, the metal sheets are firstly pressed by toothed rollers to form periodic patterns, which are then bonded by adhesive, as shown in Figure 2.16(b). Investment casting is a fabrication technique for three-dimensional lattices [60]. This technique consists in three operations: first a lattice pattern, made from low melting point material, is produced using a rapid prototyping methods. Then the pattern is dipped into a ceramic slurry (as investment material) to form a solid mold. In the following step, an heating process is performed to evacuate the pattern materials in order to fill in the molten metal. Once the molten metal is solidified, the pattern material is removed by using hand tools.

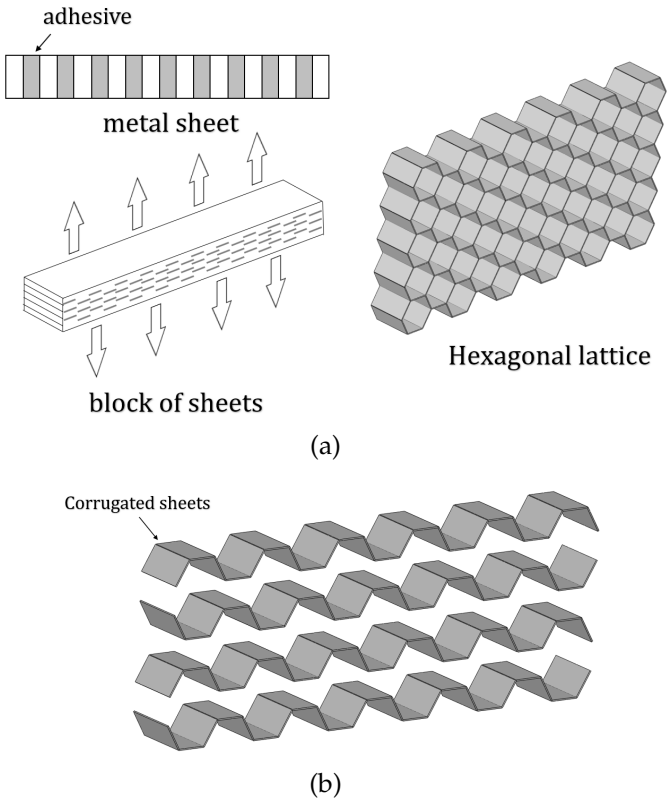

Figure 2.16: Schematic drawing of honeycomb fabrication process: (a)the expansion method, (b)the corrugation method.

However, each of these techniques has its own limitations. For example, the expansion and corrugation methods are not capable of producing complex topologies. Whereas the investment casting technique is not cost-effective and it also requires the material to have high fluidity.

Additive manufacturing(AM) provides the most effective solution for fabrication of lattices in terms of time and cost, where complex geometries can be directly produced from Computer Aided Design(CAD) models. Although there are many types of AM processes developed in the past such as Electron Beam Melting(EBM), Direct Laser Fabrication(DLF), and Selective Laser Melting(SLM) [61, 62, 63], their principles are similar, in a sense, they build three-dimensional objects by creating and stacking up consecutive layers of cross-sections. The AM processes start with spreading a layer of metal powder on the build platform. Then the layer of powder is selectively melted and solidified according to the target geometries.

For the DLF and SLM process, the fusion of metal powder is induced by a laser beam. The only difference is that the metal powder melts completely in the SLM process, whereas the DLF process heats up the powders to a temperature for them to chemically fuse. The EBM process uses a high energy electron beam instead of a laser beam, which effectively reduces residual stress induced during the fabrication process. Also a faster building speed can be achieved by using the EBM technique, but the sample qualities in terms of the dimensional accuracy and material properties are significantly limited due to its high temperature build environment. The EBM process is conducted under vacuum with building temperature higher than 870K[64]. In contrast to the EBM, the SLM process operates under an inert atmosphere with a relatively cold build environment, which enables producing small features with fine microstructures[61, 65].

The limitations of today's AM machine capability results in significant uncertainty in the mechanical properties of AM produced lattices. For instance, the strut dimensions often deviate from the target values, and the sample quality are affected by fabrication parameters[66]. Also the properties of individual strut changes with the build directions, leading to variation of the macroscopic properties of the lattices[67]. Alsalla et al.[68] performed fracture test using three-dimensional lattices manufactured using Selective Laser Melting(SLM) process. This work reported a 30% difference in the toughness measured from lattice samples built along two different directions. Hence the influence of these uncertainties need to be taken into consideration when implement the AM produced lattices in engineering applications.

2.6 Concluding remarks

This chapter reviewed the studies concerning the mechanical properties of lattices including modulus, strength and fracture toughness. The scaling relations between lattice properties, cell geometry and parent material properties have been given.

It began by considering the relationship between lattice deformation and nodal connectivity, Z, followed by a review of modulus and strength of lattices. It shows that the lattices with high nodal connectivity, Z are stretch-dominated. In such lattices, the macroscopic loading is accommodated by stretching of struts resulting in a high stiffness and strength. The lattices with low connectivity, Z, are very compliant due to the bending-dominated deformation in each unit cell.

Next section introduced the fracture toughness of lattices under different loading conditions. The expression of fracture toughness was formulated in terms of the relative density, $\overline{\rho}$, and material failure strength, σ_f. Then the use of linear elastic fracture mechanics(LEFM) was assessed using two-dimensional lattice models, where a reasonable accuracy was achieve for the model with a large crack size. Furthermore, the crack growth simulation revealed that the crack paths of lattices significantly depended on the topology and initial flaw pattern. Whereas the loading rate only affected the lattice softening behaviour.

Finally, a review of lattice fabrication methods was provided including adhesive bonding, investment casting and additive manufacturing(AM) techniques. By using the AM process, various complex topologies can be directly manufactured from Computer Aided Designed (CAD) models. However, the fabricated lattice structures suffer from significant anisotropy caused by the influence of the build direction, and are problematic for theoretical characterisation of their properties. Hence, there is a need to perform experimental studies to develop a greater understanding of mechanical properties of lattices fabricated from the modern manufacturing processes and assess the accuracy of existing prediction methods.

Chapter 3

Mechanical properties of 2D triangular lattices

3.1 Introduction

In this chapter, a comprehensive experimental study is presented to explore the mechanical behaviour of two-dimensional triangular lattices. The accuracy of analytical models and numerical predictions are assessed.

First, the lattice modulus is derived from a simple analytical model, followed by a set of numerical analysis aiming to investigate the significance of lattice orientation. Next, the influence of lattice size on the modulus is revealed, and the model size required to achieve the asymptotic modulus result is determined. Then an experimental study is presented including a description of specimen fabrication process and details of experiment procedures. The measured results are then used to validate the numerical and analytical predictions.

Next, the tensile strength is measured for the lattices fabricated in two orientations. The loading condition is identical to the modulus measurement, but the specimen geometries are modified to reduce the influence of stress concentration. The specimens are loaded to failure under a static loading condition to characterise the failure mechanism. FE simulations are presented next by adopting the defined failure criterion and element deletion technique. A comparison between the numerical predictions and experimental observations are presented.

Then, the fracture toughness of the lattice is evaluated using a set of fine-grid FE models created with various lattice orientations, aiming to assess the anisotropy of the toughness. Next, a set of fracture tests are performed using single edge notch tension(SENT) specimens made with two orientations. The fracture behaviours of different lattice orientations are compared including toughness, fracture response curves and crack paths. Finally, FE simulations of crack growth are performed to compare with the experiment results.

3.2 Lattice modulus

3.2.1 Analytical calculation

The triangular lattice is made by triangular cells which follows Maxwell's criterion. Hence struts exhibit stretch dominated deformation under mechanical load [22]: the struts are predominantly subjected to axial stresses where the contribution of bending is a second order effect[32], particularly for lattices made by slander beams. Therefore, in analytical calculations of lattice modulus each strut is taken to behave as a pin-jointed bar. For the sake of simplicity, the analytical model is chosen for a specific orientation shown in Figure 3.1 where the lattice includes struts aligned parallel to the loading direction.

In each unit cell, the load is predominantly taken by the vertical strut, see Figure 3.1. Hence, the macroscopic applied stress, σ_{app}, can be related to the local strut axial stress, σ_s, by:

$$\sigma_{app}\beta b = \sigma_s b t \tag{3.1}$$

where b is the lattice thickness and t the strut thickness. The lattice modulus E_A^* is obtained as:

$$\frac{E_A^*}{E_s} = \frac{2\sqrt{3}}{3}\frac{t}{l} \tag{3.2}$$

where E_s is the Young's modulus of the parent material. The subscript A in E^* denotes that this is an analytical prediction.

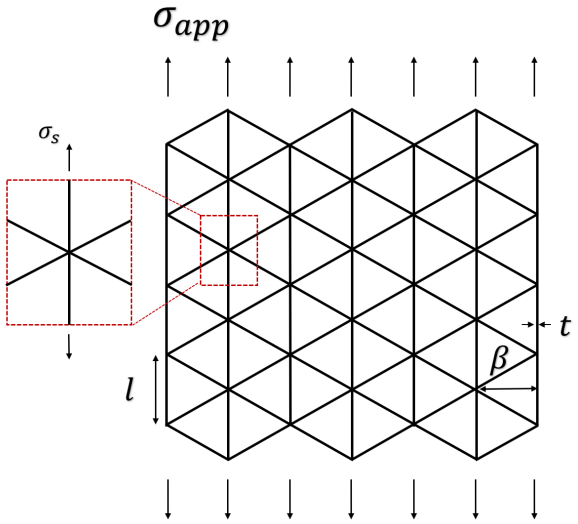

Figure 3.1: triangular lattice subjected to a remote uniaxial applied stress

3.2.2 Lattice orientation effect

In this section, FE analysis is carried out using Abaqus 6.14 to explore the dependency of the lattice modulus on the change in orientation. The lattice orientation in this work is defined by the angle θ shown in Figure 3.2, the angle between the loading direction and the axial direction of the family of struts with the same orientation. For the $\theta = 0^\circ$ orientation the vertical struts are aligned with the loading direction. A triangular lattice has a 60° symmetry and therefore in this work θ varies from $\theta = 0^\circ$ to $\theta = 30^\circ$.

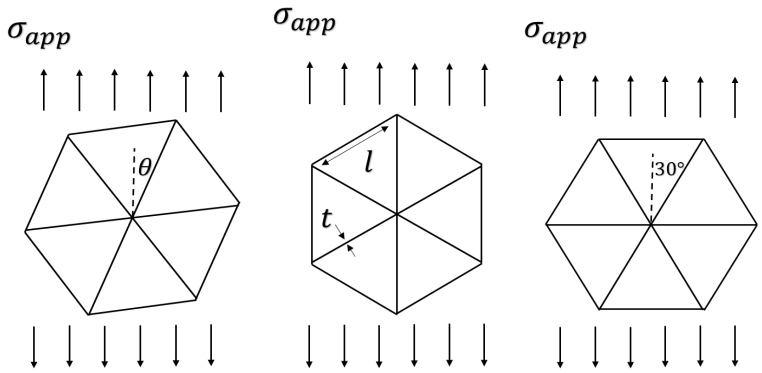

(a) θ° orientation (b) 0° orientation (c) 30° orientation

Figure 3.2: Definition of the lattice orientation angle θ. The direction of σ_{app} defines the direction of the applied load

Lattice models were created in 4 different lattice orientations with struts length $l = 10$mm and thickness $t = 1$mm shown in Figure 3.3. Each strut behaviour is modelled by one Euler-Bernoulli beam element (Abaqus element type B23), which contains 3 integration points, sufficient to simulate the elastic behaviour. The Young's modulus of the parent material was $E_s = 70$GPa. The models were $100l$ long and $60l$ wide, the width being sufficiently large to minimise the end effects caused by stress free struts on the sides for the 10° and 20° orientations.

Uniaxial tension was applied at one end while the other was fixed in the axial direction but also allowing lateral contraction. The macroscopic strain was obtained by evaluating the mean extension across the model width, and divided by the gauge length. Figure 3.10 shows the modulus evaluated from FE, which have been normalised by the relative density, $\overline{\rho}$, and the Young's modulus of the parent material. It shows that the modulus of a triangular lattice is almost isotropic, despite an approximately 2% lower results measured from the 10° and 20° orientations compared to that for the 0° and 30° orientations.

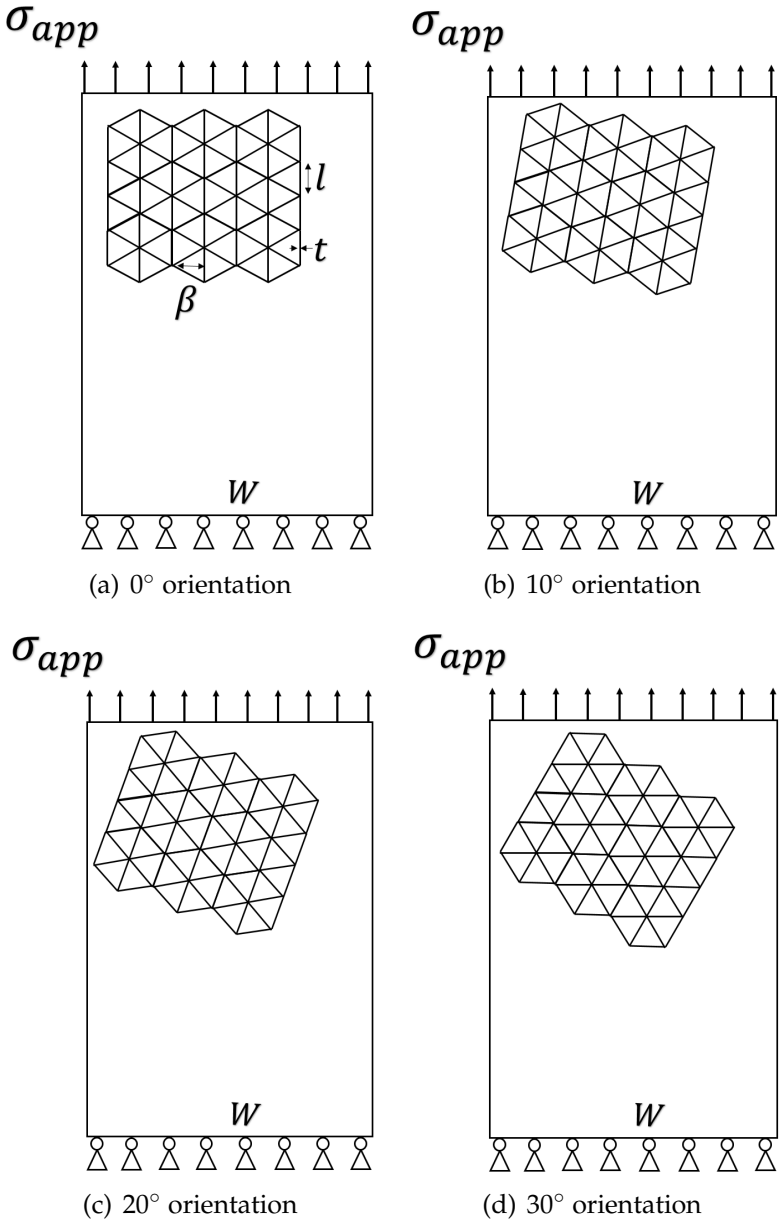

(a) 0° orientation (b) 10° orientation

(c) 20° orientation (d) 30° orientation

Figure 3.3: FE model lattice orientations

3.2.3 Size effect on lattice modulus

This section investigates the influence of model size on modulus of triangular lattices and explores the minimum model size to achieve the asymptotic material property. The size effect of the lattice modulus was investigated using FE models of the 0° orientation lattice and with a fixed unit cell width, β, as shown in Figure 3.3a). Material properties and cell dimensions were the same as those defined in the Section 3.2.2. Several different model widths, W, were analysed. Each model is subjected to tensile load imposed by uniform loading on the top surface while the bottom surface is constrained along the loading direction. The results are shown in Figure 3.4 where the FE calculated lattice modulus, E^*, normalised using the analytical prediction of Eqn. 3.2, is plotted versus the ratio of the specimen width, W, to cell width, β, denoted as α.

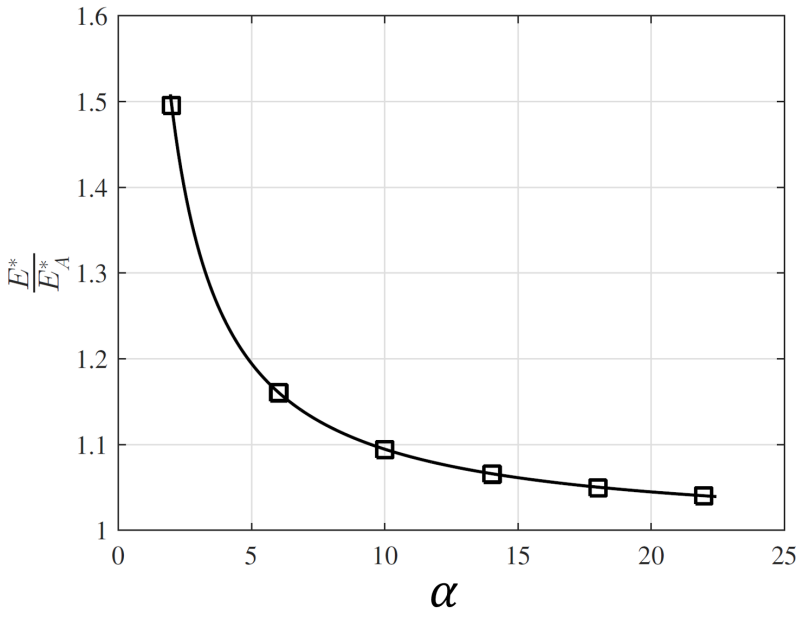

Figure 3.4: Effect of model size on lattice modulus. The symbols are from the FE simulations, the line is $(\alpha + 1)/\alpha$.

The calculated lattice modulus E^* decreases asymptotically to a saturation bulk lattice value E^*_∞ as $\alpha \to \infty$, which is almost identical to the analytical prediction. This effect can be interpreted as the applied force is proportional to $\alpha + 1$, but the cross-sectional area is proportional to α. More specifically, each vertical strut is shared by two unit cell in an infinite lattice model, while in a small model, considering an extreme case where $\alpha = 2$, there are three vertical struts wholly contained in a unit cell structure. Hence the calculated modulus for model with $\alpha = 2$ is 1.5 times of that for an infinite

lattice model. The size dependency on modulus can be expressed as:

$$E^*_\infty = E^* \frac{\alpha}{\alpha + 1} \tag{3.3}$$

3.2.4 Specimen preparation

The lattice modulus was determined by conducting a set of tensile tests. Due to the significant edge effect in 10° and 20° orientations, only the 0° and 30° orientation lattice specimens were considered. The specimen geometry was designed based on the outcome of the previous study on size effect shown in the Figure 3.4 to ensure a sufficient size to achieve the asymptotic result. Also the specimen had to be long enough to avoid the end conditions affecting the accuracy of the measurement of modulus.

Hence, the lattice specimen was designed with overall dimensions about 750mm long by 250mm wide. The specimen width was chosen so that the ratio of the specimen width to unit cell size, $\alpha = 24$, was large enough to ensure that the measured modulus is indicative of the lattice property, E^*_∞. The length of the central section was around 550mm as shown in Figure. 3.5. FE was used to verify that the length of the specimens was suitable. The ends of the sheet were left solid so that the sheet could be attached to the test machine grips using pins as shown in Figure 3.5. The nominal strut length and thickness were 10mm and 1mm.

Two specimens, one for each orientation, were machined from a 2mm thick aluminium alloy Al1050A sheet through abrasive water jet cutting (AWJC) technique. This technique involves introducing a stream of abrasive particles into high speed water jet and direct it towards metal sheet to perform cutting[69]. The advantage of the AWJC method over other manufacturing methods is that the specimen is not subjected to an increase in temperature which minimises strut distortion.

The cutting process was performed using a Flow Mach2c waterjet cutter equipped with an ultahigh pressure pump which is able to provide a maximum pressure of 400 MPa. The quality of the process significantly depends on tuning parameters including water pressure, abrasive grade, abrasive mass flow rate and standoff distance. The influence of the machine parameters on dimensional accuracy of specimen has been described in Ozcelik [70]. The specimens were machined using a high pressure water jet with mass flow rate of 15g/s, aiming to achieve good surface condition. A 120 grade ruby dust was used as the abrasive material with particle sizes of 106 to 250 micrometer. The small particle sizes was used to effectively reduce the kerf taper angle caused by high rate of material removal at the jet entrance [71]. The waterjet nozzle width was chosen to be 0.5mm to achieve a good dimensional accuracy.

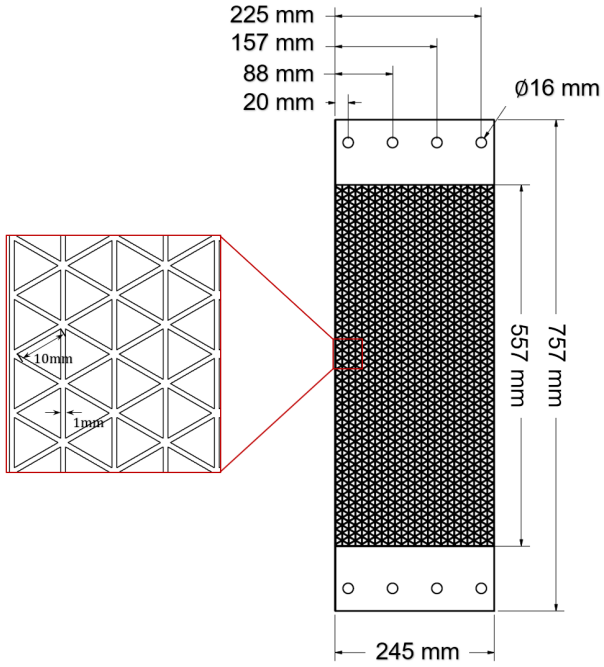

(a)

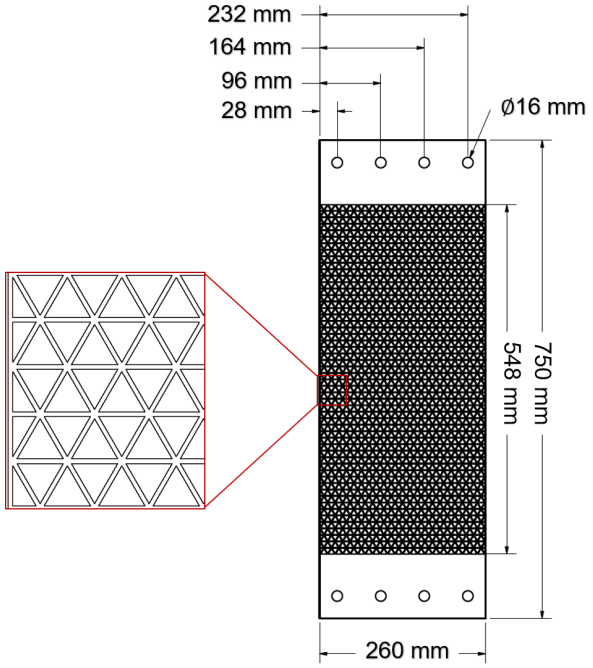

(b)

Figure 3.5: Uniaxial tensile tests of lattice specimens:(a) 0° orientation specimen and (b) 30° orientation specimen

The strut dimensions that were achieved by the AWJC technique are shown in Figure 3.6(a), which are the mean values of measurements from 100 randomly chosen struts. The strut mean thickness is $\bar{t} = 1.1$mm with a standard deviation of 0.02mm. The circular water jet results in smooth lattice corners with a fillet radius of about $\bar{r} = 0.5$mm. The mean strut effective length is $\bar{l} = 9.7$mm, slightly shorter than the nominal value of 10mm due to corner fillets. Figure 3.6(b) shows a detail of one of the specimens cut using the waterjet method.

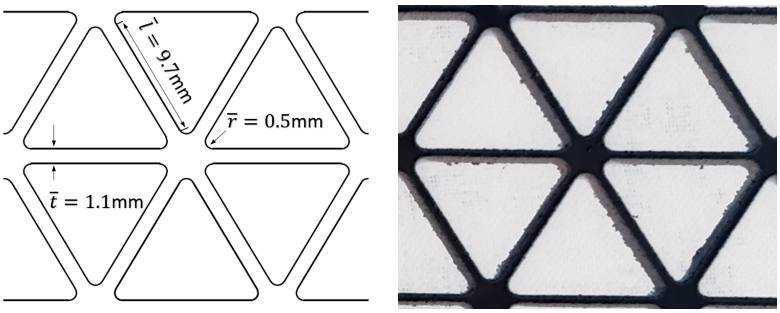

(a) (b)

Figure 3.6: Lattice manufacture by the waterjet method: (a) lattice dimensions, (b) detailed photograph of one of the lattice specimens

3.2.5 Modulus measurement

To support subsequent FE analysis, a tensile test was performed to characterise the material properties of the Al1050A aluminium alloy. A standard dog-bone specimen with gauge length of 50mm was use to determine the stress-strain curve of the materal, as shown in Figure 3.7, The Young's modulus and the ultimate tensile strength (UTS) was measured to be as 70 GPa and 139MPa. The initial yield stress was measured using a 0.2% strain offset, which was $\sigma_y = 134$MPa.

Then a tensile test was carried out on the lattice specimens. The experiment configurations are shown in Figure 3.8, where both ends of the specimens are pinned to a rigid fixture. A displacement-controlled tensile loading was applied at rate of 1mm/min corresponding to the strain rate of 0.002 /min, followed by an unloading process before reaching to the elastic limit. The specimen deformation were measured by an iMETRUM video gauge system which tracks the positions of pre-defined points on the surface shown in Figure 3.9 [72]. This technique is referred to as Digital Image Correlation (DIC) which evaluate deformation of the interested area by comparing digital greyscale images taken before and after a deformation has occurred[73]. The gauge area was chosen at the central area of the specimen with gauge length of $20l$ shown in Figure 3.9 .

Ten targeted points were marked on the specimen, 5 points at each end. The area of interest is manually defined around each targeted point and ensure sufficient surface pattern is included. Video was recorded during the test by a camera with resolution of 1.4 megapixels, and the system offers frame rate of 17.8 fps, sufficient to capture specimen deformation under quasi-static loading. The captured images are analysed using the iMETRUM software tool, which applies recognition algorithms to detect the change in position of the targeted areas. Hence macroscopic strain is measured, and the linear stress-strain response was obtained. The lattice modulus was calculated from the slope of the unloading curve, to avoid the influence of plasticity effects.

Figure 3.10 shows a plot of the experimentally measured normalised lattice modulus for lattice orientations of between 0° and 30°. The experimental measured modulus are compared with those predicted by the analytical and FE models, and a good agreement has been achieved. The FE results for 0° and 30° are slightly higher than for 10° and 20° resulting from the small bending contribution from the intermediate orientations.

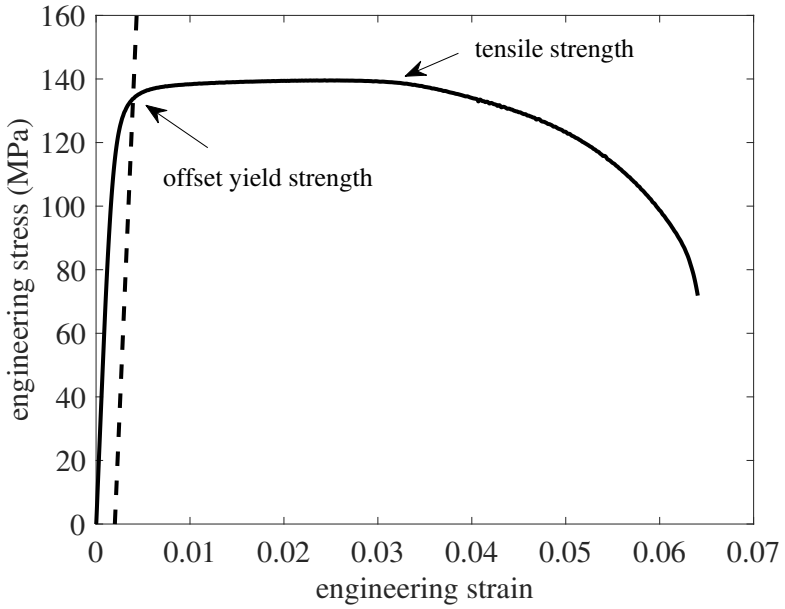

Figure 3.7: Measured stress versus strain behaviour for Al1050A aluminium alloy

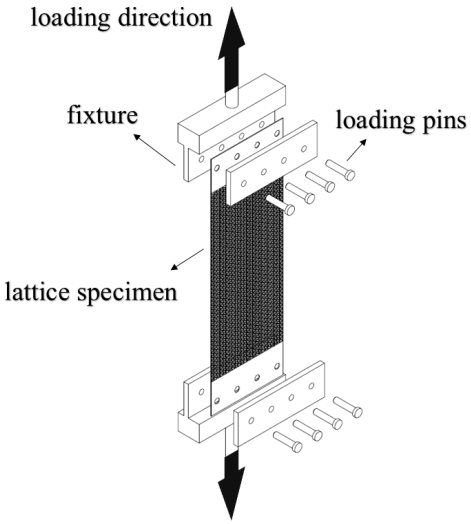

Figure 3.8: Experiment set-up for the lattice tensile test

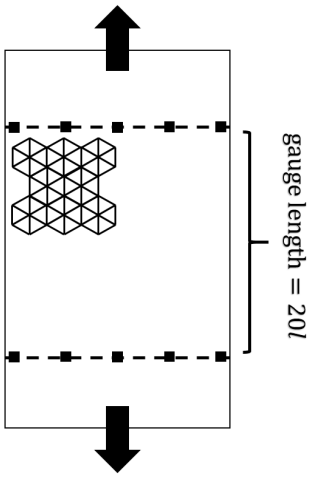

Figure 3.9: Diagram showing the ten locations used for the video gauge measurement of lattice extension

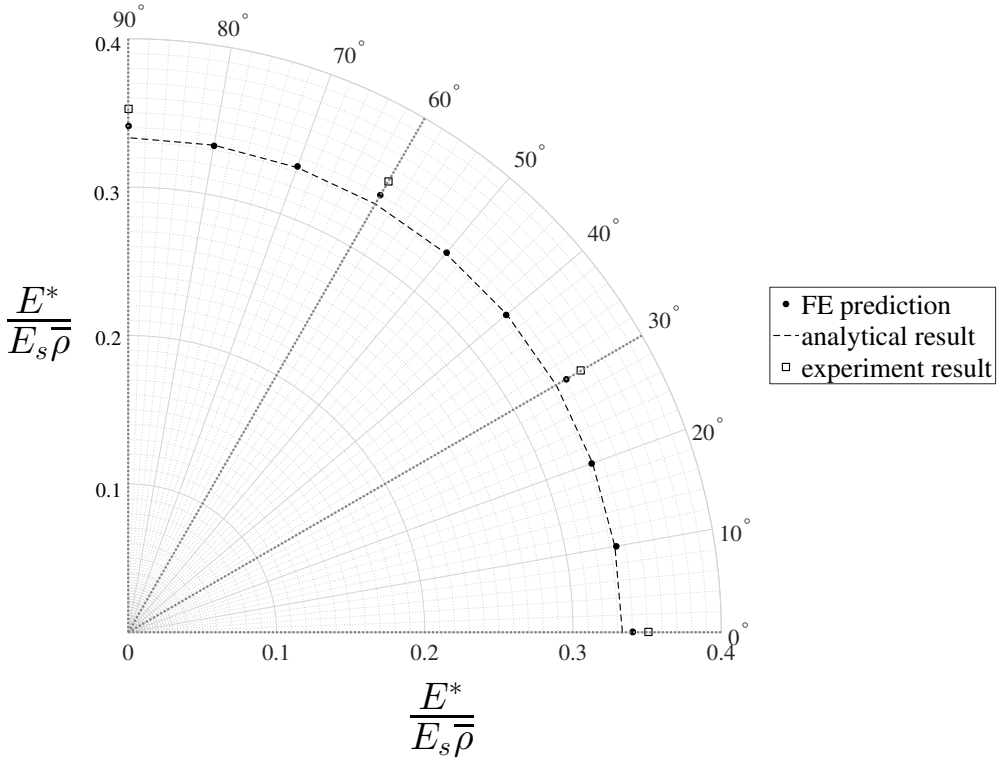

Figure 3.10: Experimentally measured normalised lattice modulus compared with the results of the analytical and FE models

3.3 Lattice strength

3.3.1 Evaluation of lattice initial yield strength

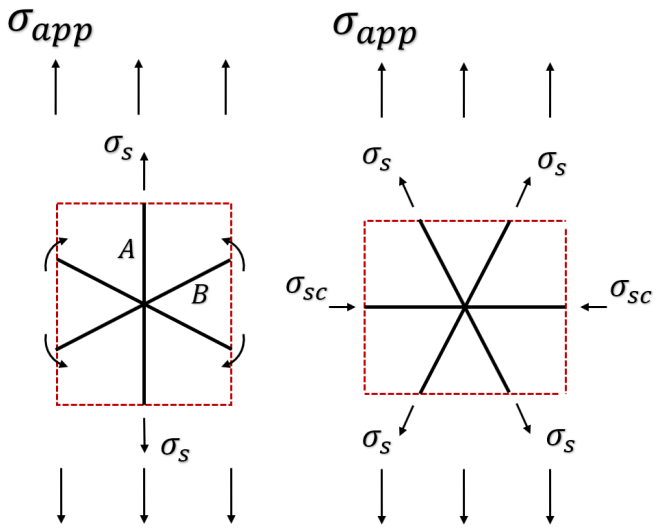

(a) 0° orientation (b) 30° orientation

Figure 3.11: Unit cell of triangular lattice in different orientations

The analytical calculation for the initial yield strength of triangular lattice has been performed on two different orientations shown in Figure 3.11. As mentioned in Section 3.2.1, for 0° orientation, the applied stress is predominantly distributed through vertical struts. Hence, the initial yield strength of a 0° triangular lattice, σ^0_{ys}, can be obtained by replacing σ_s in Eqn. 3.1 with the material yield stress σ_y to give:

$$\sigma^0_{ys} = \frac{2\sqrt{3}\sigma_y t}{3l} = \frac{\sigma_y \bar{\rho}}{3} \tag{3.4}$$

For a 30° orientation lattice, all struts are subjected to tensile and compressive stresses. The applied stress is related to the axial stress in struts at 30° to the loading axis by:

$$\sigma_{app} bl = 2\sigma_s bt \cos(\frac{\pi}{6}) \tag{3.5}$$

The yield strength of the lattice can then be obtained by replacing the axial strut stress with the material yield strength:

$$\sigma^{30}_{ys} = \frac{\sqrt{3}\sigma_y t}{l} = \frac{\sigma_y \bar{\rho}}{2} \tag{3.6}$$

From Eqns. 3.4 and 3.5 the yield strength of the 30° orientation is about 1.5 times higher than that of 0° orientation.

A set of FE analyses is performed to explore the dependency of lattice orientation on its yield strength, σ^*_{ys}. The analysis conducted in Section 3.2.2 as shown in the Figure 3.3 was repeated using the measured material properties from the tensile test shown in the Figure 3.7 with an assumption of isotropic hardening. In this numerical model, we evaluate the properties of ideal lattices where the influences of surface imperfection and the volume of vertices are neglected. The initial yield strength of lattices in 4 different orientations were shown in the Figure 3.15. The results shown that the 0° orientation, where the macroscopic stress is only distributed through vertical struts (strut A shown in Figure 3.11), provide the lowest yield strength. The yield strength increases with an increase in the degree of orientation, due to the fact that the strut B rises its contribution to the macroscopic strength. In 30° orientation, the yield strength of the lattice reaches to its maximum which is about 50% higher than the 0° orientation, and the applied stress is equally distributed through strut A and B.

3.3.2 Strength measurement

The strength of 0° and 30° orientation lattices were experimentally investigated, as they represented the lower and upper bound of strength for triangular lattices. The specimen geometry for the measurement of the strength of the lattice is shown in Figure 3.12. The lengths of the specimens were less than those for the measurement of modulus, but were again guided by FE analysis to ensure they were long enough to provide a valid measurement. The material properties and strut dimensions were the same as described in Section 3.2.2 and 3.2.4. Three specimens were tested for each orientation. The different orientations required slightly different geometries for the specimens. FE analysis showed that a waisted specimen was required for the 0° specimen seen in Figure 3.12(a) to reduce the stress concentration at the point in the specimen where the machined lattice ends. FE analysis indicated that only a small stress concentration existed at this point for the 30° specimen of Figure 3.12(b). Tensile load was applied on the specimen with loading rate of 2mm/s, and the macroscopic strain was measured using the Video gauge described in Section 3.2.5.

For tests on the 0° specimens, the vertical struts failed along a path at 30° to the horizontal axis as shown in Figure 3.13(a). For the 30° specimens, the failure path is step-like, 3.13(c). The measured stress versus strain responses of a representative 0° and 30° specimen are shown in Figure 3.14. The initial yield strength was found using the 0.2% strain offset. The ultimate tensile strength is taken as the maximum stress on the response curves. The two specimens exhibit the same modulus, however both the yield strength and ultimate tensile strength of the 30° specimen are approximately 1.5 times higher than the 0° specimen, as shown in Table 3.1.

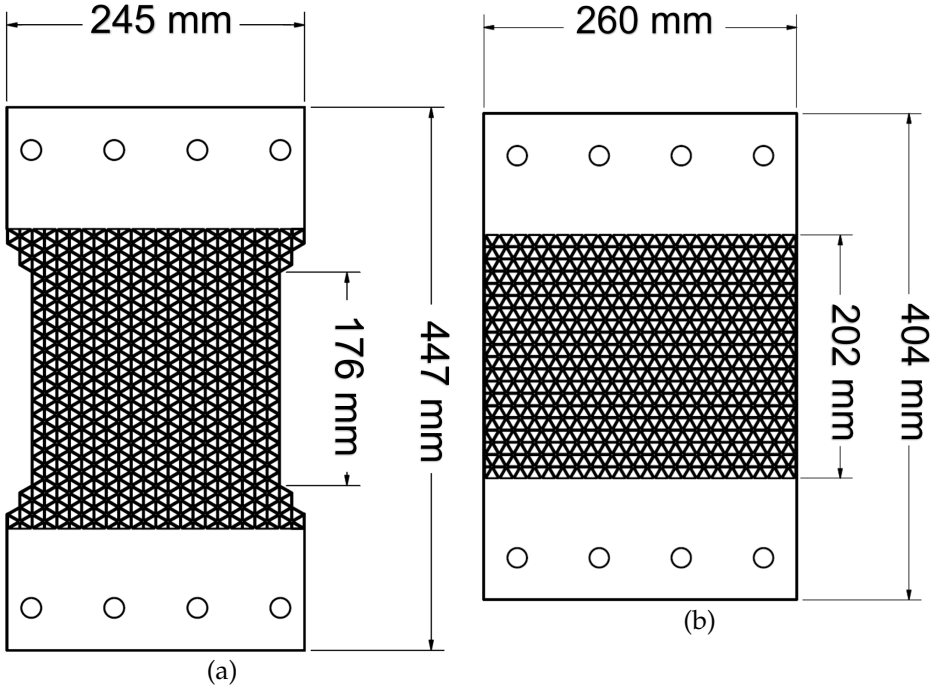

Figure 3.12: Specimens for tensile strength tests: (a) 0° orientation and (b) 30° orientation.

Orient.	Sample	Measured strength σ_{ys}^{exp} (MPa)	Measured UTS σ_{u}^{exp} (MPa)	Predicted strength σ_{ys} (MPa)
	1	15.4	16.6	
0°	2	14.8	15.8	17.5
	3	15.1	16.2	
	1	22.9	23.5	
30°	2	21.7	22.3	26.3
	3	22.3	22.9	

Table 3.1: Experimentally measured strengths for 0° and 30° specimens compared with analytical predictions

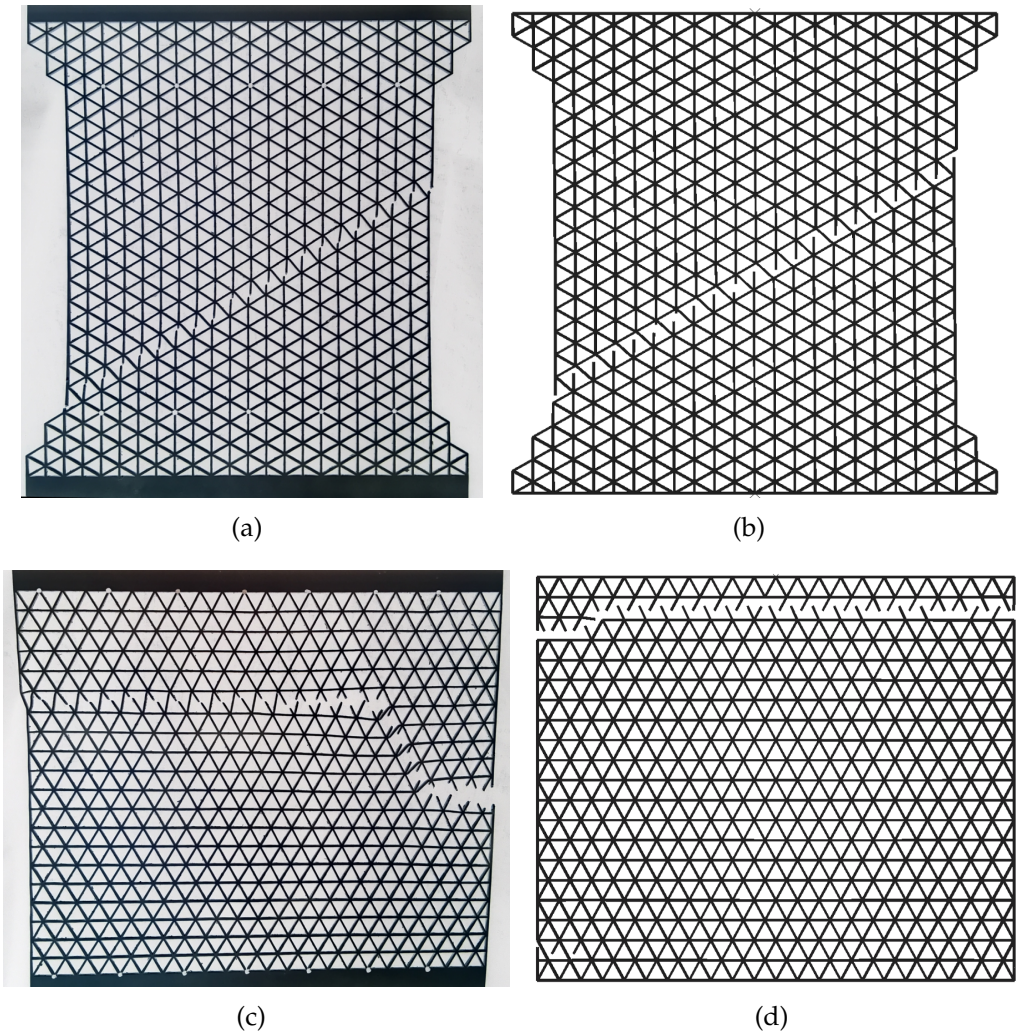

Figure 3.13: Experimental and FE predicted failure loci: (a) experimental locus for 0° orientation, (b) FE locus for 0° orientation, (c) experimental locus for 30° orientation and (d) FE locus for 30° orientation

3.3.3 Finite element simulation

Timoshenko beam elements (Abaqus element type B21) were used to predict the tensile response of the lattice. This type of element contains a single integration point to control the damage behaviour, which was found to be more suitable for the simulation of progressive damage in lattices than the Bernoulli beam element (B23). 10 elements were used for each strut, enough to provide convergence of the results. The strut length and thickness in the model were 10mm and 1.1mm respectively, based on the strut measurement data from Section 3.2.4.

The element removal technique was used to simulate damage progression in both 0° and 30° lattices. Failure initiates when the maximum axial strain in the element reaches 0.03 which is based on the result of the tensile test shown in Figure 3.7. The strut necking behaviour is replicated by the reduction of the yield stress after failure initiates, which is characterised by the damage variable B:

$$\sigma = (1 - B)\sigma_y \tag{3.7}$$

where B ranges from 0 to 1 and is a function of the plastic strain, fitted to match the data of Figure 3.7. When $B = 1$, the material point has failed and the corresponding element is deleted from the mesh.

To replicate the loading condition of the experiment, Each model was subjected to a rigid displacement at top end while the bottom end was fixed. The FE predicted failure paths are compared with the experimentally measured ones in Figure 3.13(b) and (d). Figure 3.14 compares the FE predicted engineering stress versus strain behaviours for the two orientations with the experimental results. In general, there is good agreement between the FE and the experiments.

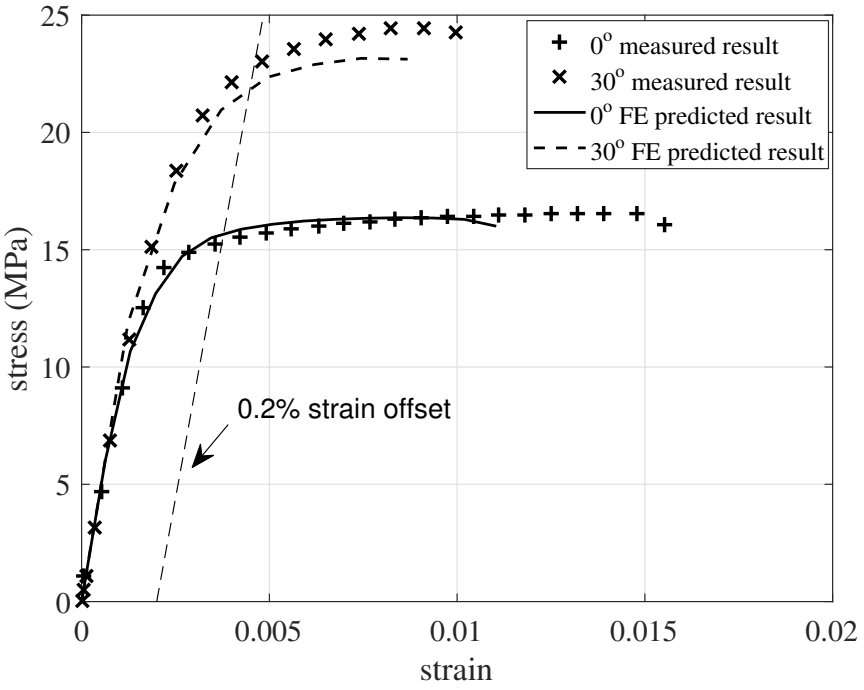

Figure 3.14: Nominal stress versus nominal strain responses for representative 0° and 30° specimens.

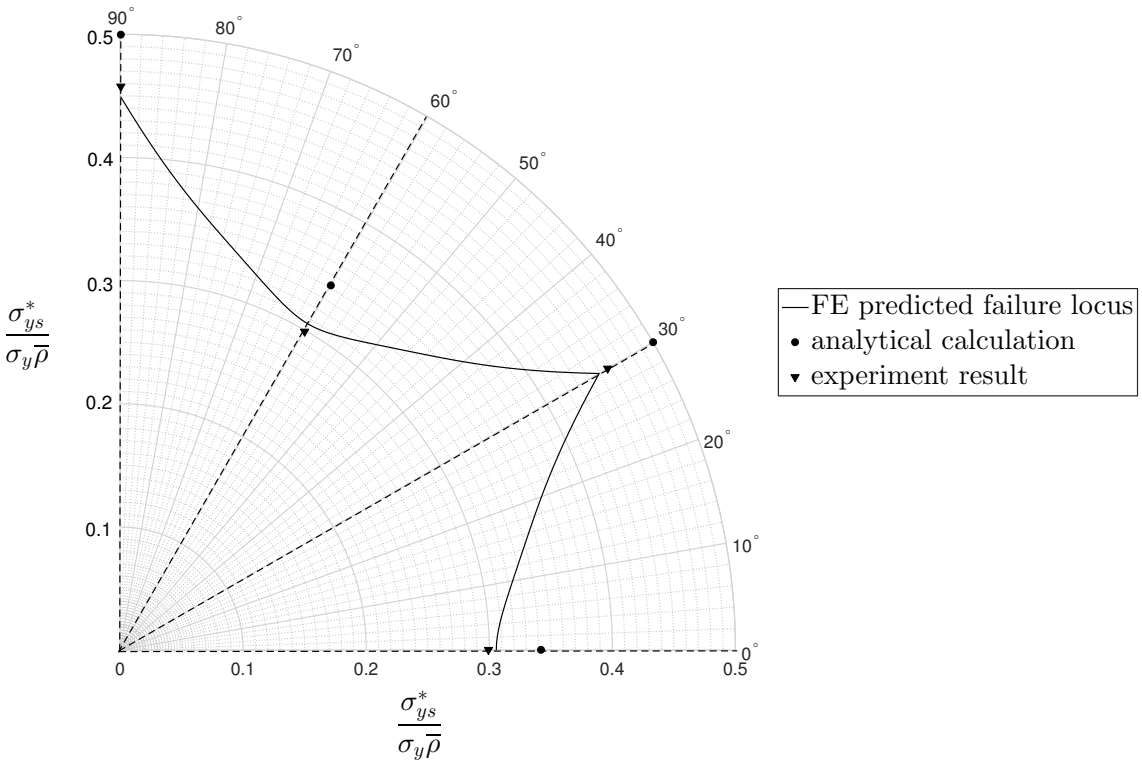

Figure 3.15: Orientation dependent normalised lattice yield strength

3.4 Fracture performance

3.4.1 Fracture toughness

The fracture toughness of triangular lattice was evaluated using a boundary layer analysis. A set of large circular models with prescribed boundary displacement was created to explore the orientation dependency of the fracture toughness in triangular lattices. Euler-Bernoulli beam elements were used (Abaqus element type B23) in order to obtain accurate results with a reduced number of elements. Models of radius $100l$ for four different lattice orientations were created as shown in Figure 3.16. Displacements were applied on the outer boundary in each model based on the K_I asymptotic displacement field[52].

Two sets of analyses were carried out for each model. The first analysis was performed with brittle material properties: the struts behave in a linear elastic manner until the material strength is reached at which point they fail instantaneously. The second analysis was performed with ductile material properties. For this analysis the failure was strain controlled: failure was assumed to initiate when the mean value of strut axial strain across the section reaches to the failure strain. In the linear elastic model, the material modulus and failure strength were defined as 70 GPa and 140 MPa, while for the ductile lattice model, the material was assumed to be elastic perfectly plastic with modulus of 70 GPa, yield strength of 134 MPa and failure strain of 0.03.

The FE evaluated fracture toughness for these two set of analysis are shown in Figure 3.23. The results show that the fracture toughness is significantly affected by the orientation, particularly for ductile lattices where the 30° orientation has a fracture toughness 16% higher than the 0° orientation and 40% higher than the 10° and 20° orientations. The normalised toughness for brittle lattices ranged from 0.46 to 0.52 which is less sensitive to the changes of orientation compared to the ductile lattices. The highest toughness for brittle lattice was obtained from a 0° orientation which agrees well with the result given in the literature[3, 5]. The toughness of 10° and 20° orientations were approximately 10% lower than the 0° orientation.

3.4.2 Lattice toughness size effect

This section demonstrates the size effect on the apparent toughness and aims to explore the minimum specimen size to achieve the asymptotic toughness value of a triangular lattice. The effect of specimen size on apparent fracture toughness was investigated using FE analysis. A set of single edge crack lattice models was created in various sizes, as shown in Table 3.2. In all models the crack length,a, was a quarter of the model width, $0.25W$.

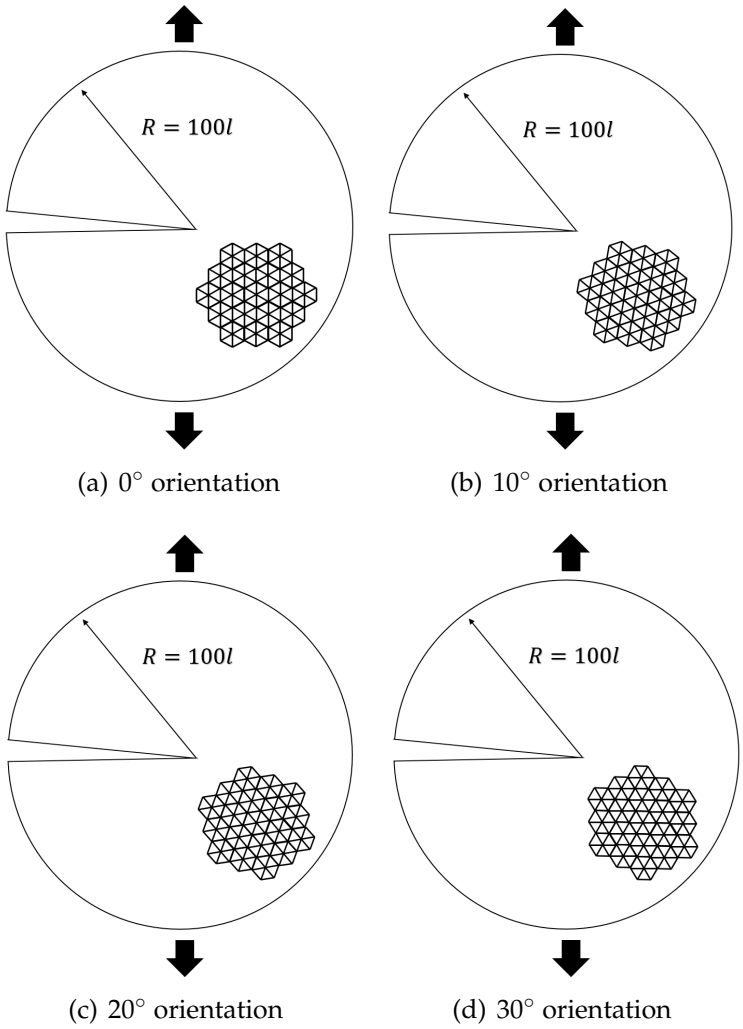

(a) 0° orientation (b) 10° orientation

(c) 20° orientation (d) 30° orientation

Figure 3.16: Boundary layer FE models for predictions of fracture toughness: (a) 0° orientation, (b) 10° orientation, (c) 20° orientation and (d) 30° orientation

Two sets of analysis were conducted with the same material properties as in Section 3.4.1. Uniaxial tensile load was applied to each model to evaluate the lattice stress, σ_t^* at which the crack starts to grow. Each model was subjected to a uniform tensile load on the top edge while the bottom edge was constrained along the loading direction and free to contract laterally.

The lattice stress for crack growth σ_t^* normalised by the material failure stress, σ_f, is shown in Figure 3.17. The toughness based predictions are calculated based on toughness evaluated from the boundary layer analysis. Clearly the strength of larger specimens tends to be toughness controlled. It was found that the toughness based prediction significantly overestimated the strength of the small scale ductile lattices compared to that of brittle lattices. This is due to relatively large plastic zones in smaller specimens,

compared to the specimen sizes, and that the boundary layer analysis was based on the small scale yield assumption. The results suggest that a very large specimen (compared to the cell size) must be used in experimental measurement of toughness, for the results to agree with the boundary layer prediction.

a/l	W/l
2.5	10
4.5	18
6.5	26
8.5	34
10.5	42
12.5	50
14.5	58
16.5	66

Table 3.2: Size of 0° orientation triangular lattice models with $t = 1$mm and $l = 10$mm. a/l is the normalised crack length and W/l is the normalised specimen width.

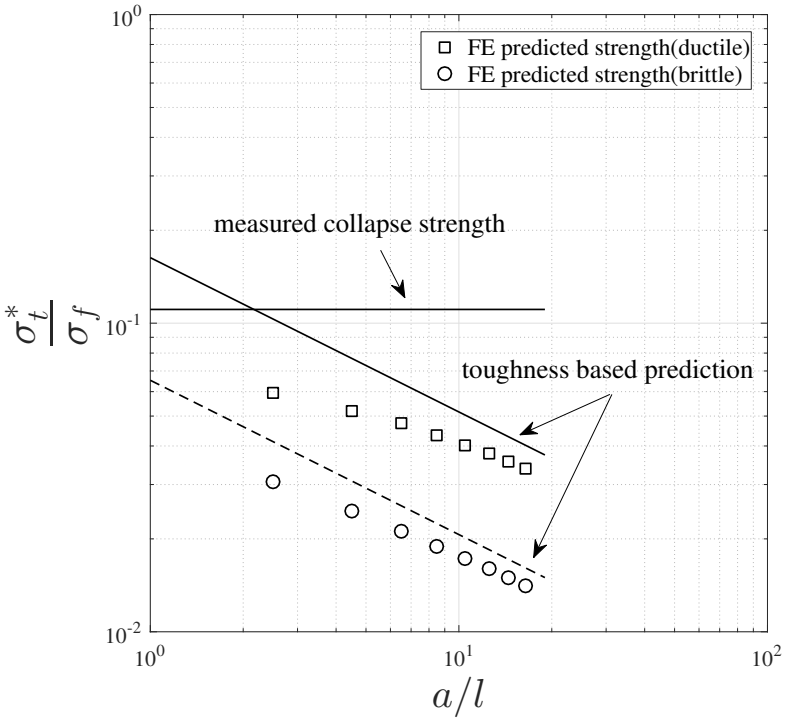

Figure 3.17: Normalised lattice stress for crack growth versus lattice size

3.4.3 Edge crack fracture experiments

Edge crack fracture tests were carried out under displacement control to measure apparent toughness, load-displacement behaviour and crack paths for 0° and 30° lattices. The edge crack geometry was used to reduce the influence of T-stress [74]. The specimen dimensions were the same as shown in Figure 3.5 in Section 3.2.4. Two specimens were tested for each orientation, one with an edge crack of length given by $a = 3.5l$ and one given by $a = 5.5l$. The edge cracks were cut into each specimen at the mid-section using electrical discharge machining (EDM) with a wire thickness of 0.5 mm to minimise the strut damage caused during the cutting process. The length of the crack,a,was measured from the edge of the specimen to the centre of the cell, as shown in Figure 3.18. Each specimen was subjected to a rigid displacement(no ends rotation) with loading rate of 0.2 mm/min to ensure a quasi-static deformation.

#	Orient.	a	$\frac{a}{W}$	K_{IC}, MPa$\sqrt{m}$
1	0°	$3.5l$	0.14	3.8
2	30°	$3.5l$	0.13	4.4
3	0°	$5.6l$	0.22	4.6
4	30°	$5.6l$	0.21	5.2

Table 3.3: Experimental measurement of fracture toughness for edge cracked lattices

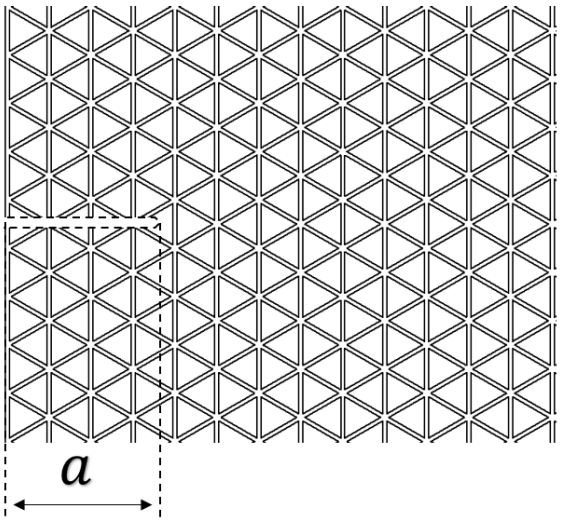

Figure 3.18: Edge crack of lattice specimen

Two types of crack paths were observed in the tests as shown in Figure 3.21(a) and (c). In Figure 3.21(a), for 0° specimens, the crack grew at a 60° angle to the loading direction. All struts aligned in the loading direction ruptured, while the angled struts bent plastically. This resulted in a significantly non-linear load versus displacement response seen in Figure 3.22. In Figure 3.21(c), for 30° specimens, the crack propagated in the direction normal to the loading direction horizontally.

Out-of-plane deformation of the specimen was observed as the crack approached the edge of the specimen, as shown in Figure 3.19. This effect can be seen in the load versus displacement curve in Figure 3.22, where load reduction in a 30° specimen significantly slows down after the first rapid load drop. Finally, note that 30° specimens show higher fracture loads than 0° specimens. The fracture toughness,K_{IC}, was calculated as:

$$K_{IC} = f(\frac{a}{W})\sigma_{app}\sqrt{\pi a} \tag{3.8}$$

where σ_{app} is the peak stress applied to the specimen when the crack starts to grow, a is the measured crack length and $f(a/W)$ is a geometry factor evaluated from previous work[49].

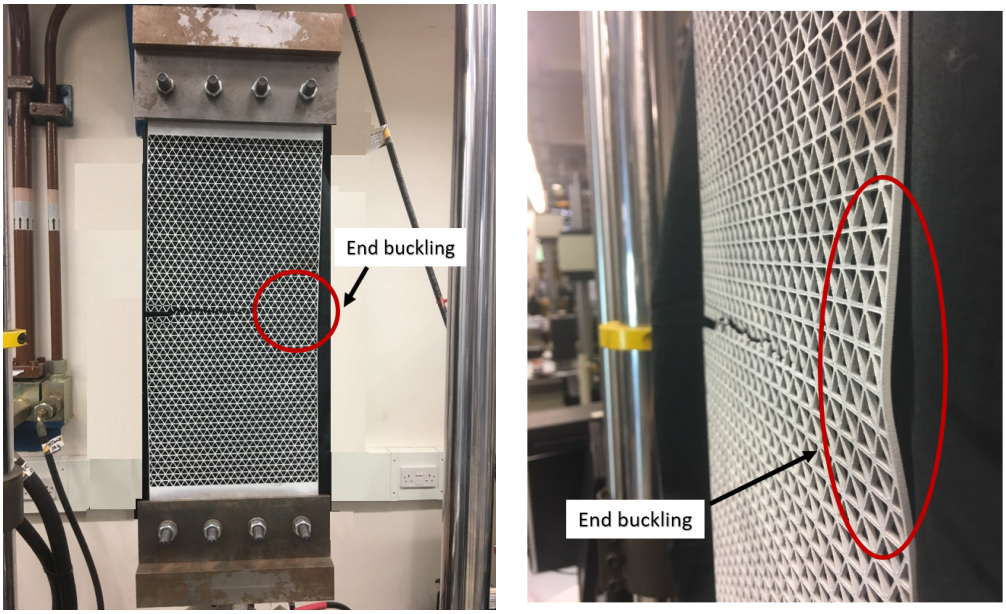

(a) (b)

Figure 3.19: Out-of-plane deformation for a 30° fracture specimen

It was found that the measured toughness of 30° specimens is significantly higher than 0° specimens for both crack lengths, as shown in Table 3.3. The normalised toughness is compared against the boundary layer predictions in Figure 3.23. The measured results are significantly different to the boundary layer predictions due to the effect of finite specimen size. Higher toughness results, obtained in specimens with longer cracks, are closer to the boundary layer predictions.

3.4.4 Crack growth simulation

Fracture propagation in the edge crack specimens was also simulated with FE. The models used two-dimensional Timoshenko beam elements with the element length of 1mm. In each model, the top end was subjected to a vertical displacement, while the motion of the bottom end was fixed in all directions to replicate the condition of experiment, as shown in Figure 3.20. Crack propagation was carried out using the element deletion technique described in the Section 3.3.3. The predicted crack paths, shown in Figure 3.21, are consistent with the experiment results shown in the same figure. It was noticed that the failure occurred near to the joint, due to the significant strut bending at the crack tip. A good agreement was also obtained between the FE predicted load versus displacement curves and experimental results, as demonstrated in Figure 3.22.

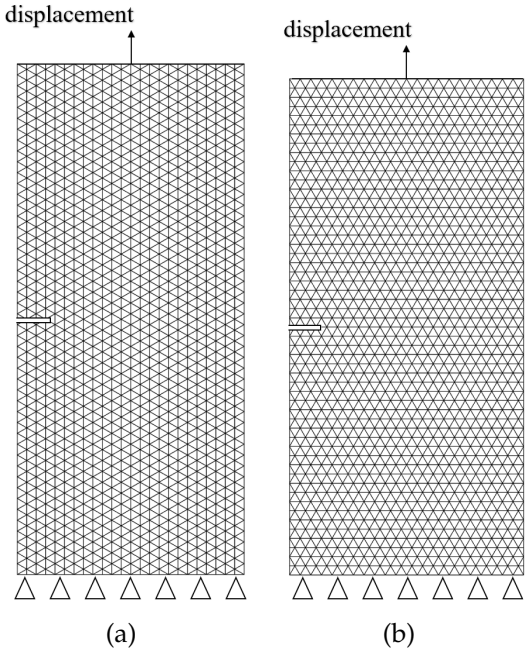

Figure 3.20: FE models for the simulation of crack paths: (a) 0° orientation (b) 30° orientation.

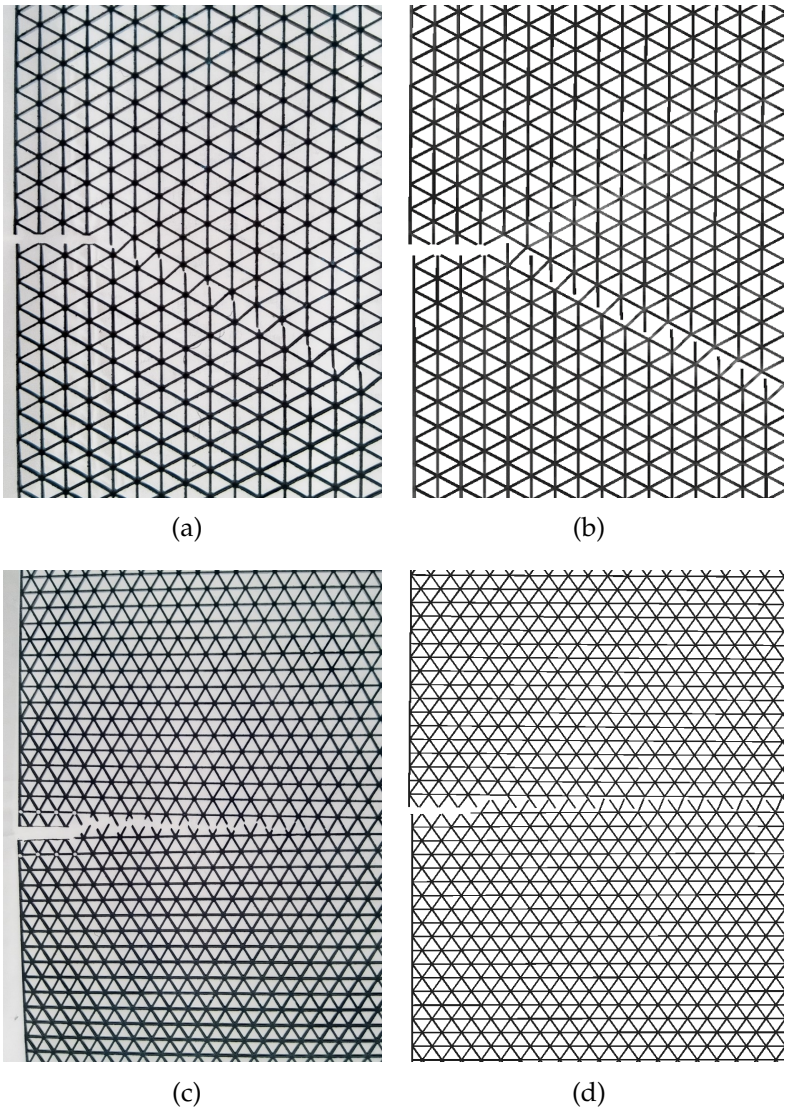

Figure 3.21: Measured and predicted crack paths in edge cracked specimens: (a) 0° measured crack path, (b) 0° FE predicted crack path, (c) 30° measured crack path and (d) 30° FE predicted crack path

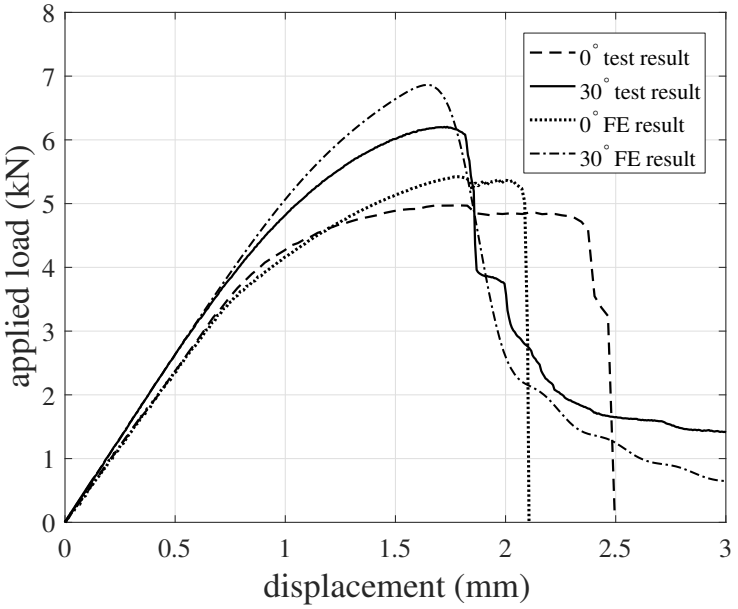

(a)

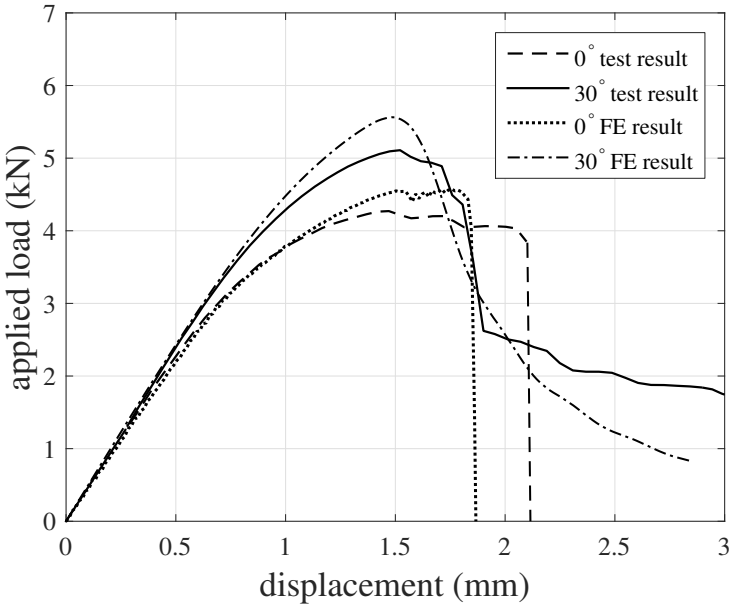

(b)

Figure 3.22: Experimentally measured and FE predicted load versus displacement behaviour for fracture specimens: (a) response for $a = 3.5l$ and (b) response for $a = 5.5l$

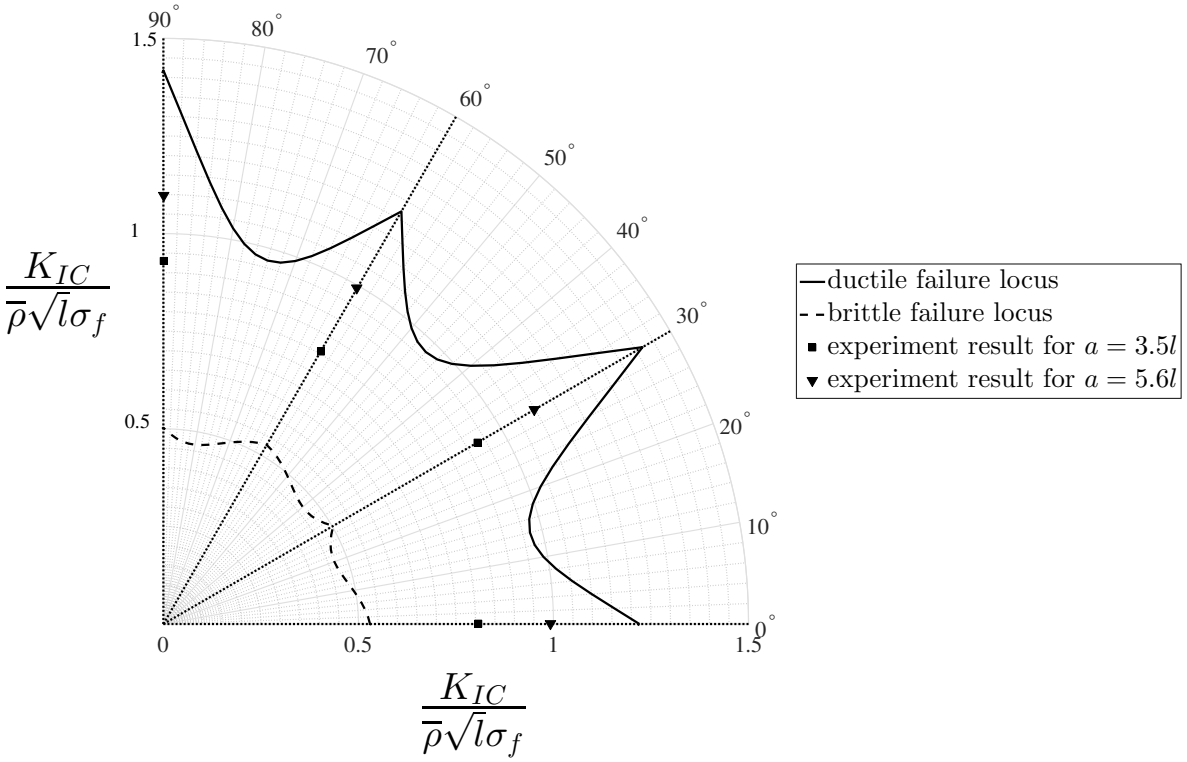

Figure 3.23: Orientation dependent normalised fracture toughness for brittle and ductile failure

3.5 Concluding remarks

The macroscopic mechanical properties of the two-dimensional triangular lattice including elastic modulus, strength and fracture toughness have been experimentally measured. It was found the experiment results for the modulus and strength agreed well with the numerical predictions, while the measured fracture toughness was significantly lower than the predicted value due to the size effect.

It has revealed that the strength and toughness of the lattice exhibited strong orientation dependency, while the modulus was almost isotropic. The measured strength of a 30° orientation lattice was 1.5 times that of a 0° lattices, and the normalised toughness can increase from under 1 to 1.4 with lattice orientation. The fracture behaviours such as crack paths and load-displacement curves are also orientation dependent. The crack path of a 0° lattice is at 60° to the loading direction, while for a 30° lattice the crack path is horizontal.

The measured properties are plotted in the material property chats, as shown in Figure 3.24 3.25 and 3.26. The 30° orientations exhibit better mechanical properties compared to that of 0°. In general, the properties reached by the Aluminum triangular lattices are comparable to those of polymers and natural materials.

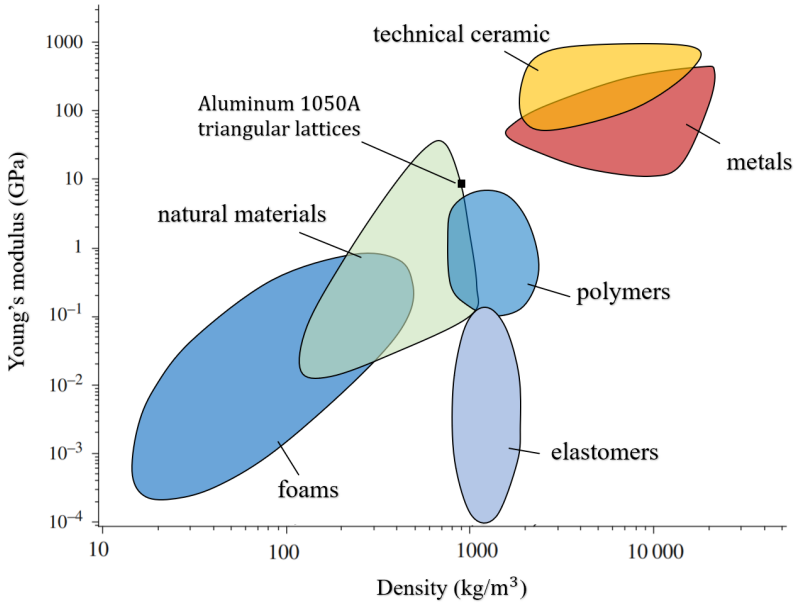

Figure 3.24: Material property chart for Young's modulus

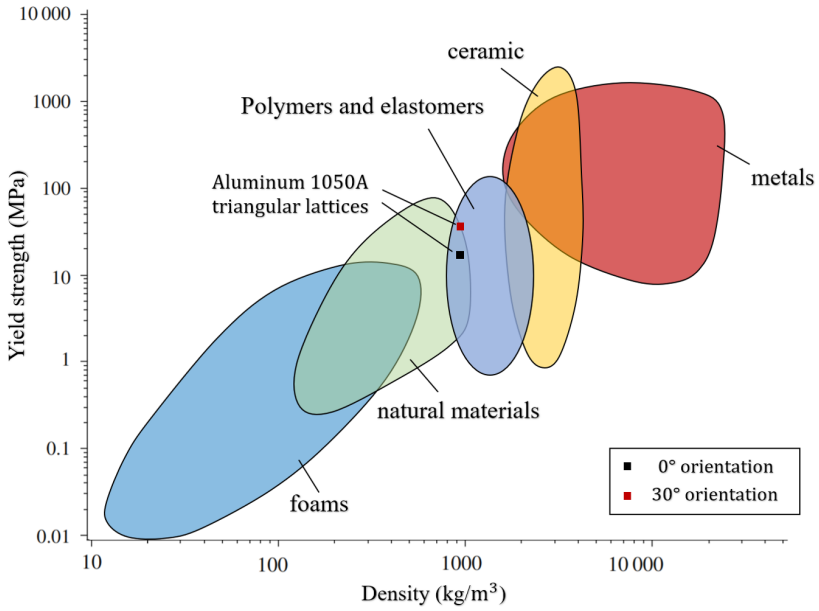

Figure 3.25: Material property chart for strength

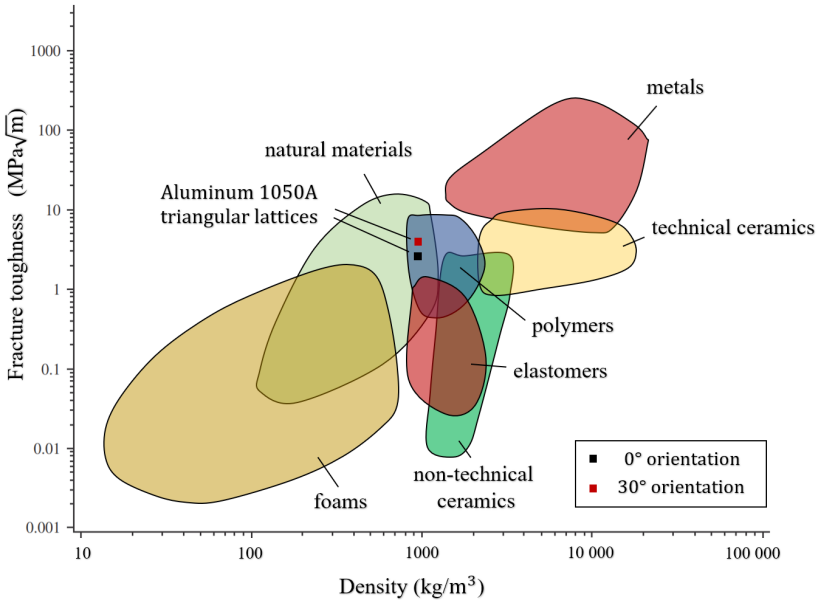

Figure 3.26: Material property chart for fracture toughness

Chapter 4

Modulus and strength of 3D lattices

4.1 Introduction

This chapter explores mechanical properties of three-dimensional lattices. The octet-truss lattice is used in this study due to its high strength to density ratio and great potential in the advanced lightweight structure applications.

First the lattice configuration and its unit cell are described. The lattice orientations are defined according to the loading directions. The next section provides analytical derivations of the lattice strength in three different orientations, where the lattice is assumed to be a pin-jointed frame.

Then a set of numerical analysis is performed using different sized lattice models to illustrate the significance of model size on its macroscopic properties. The same analysis is repeated for different lattice orientations to investigate anisotropy.

Next, an experiment is conducted aiming to validate numerical predictions. The specimens are made by a brittle photo-polymer resin, and fabricated using an additive manufacturing technique. A brief description of the fabrication process and background of the technique are provided.

Finally, the mechanical behaviours of the photo-polymer resin is experimentally determined through a uniaxial tensile test. The details of the experiment including the loading condition and measurement technique are described. The measured results are presented and used to assess the accuracy of numerical predictions.

4.2 Lattice configuration

The octet-truss lattice is a face-centred cubic structure with a nodal connectivity of 12 which obeys the Maxwell's criterion, and is a stretch-dominated structure. It was first designed by Fuller in 1961[75] as a three-dimensional space filling material due to its high weight efficiency. The unit cell of the lattice includes a octahedron at the cell centre and 8 tetrahedron sub cells distributed on each face, as shown in Figure 4.1. The coordinate system was described using the Miller indices and the relative density was evaluated based on the unit cell configuration:

$$\overline{\rho} = 6\sqrt{2}\pi(r/l)^2 \tag{4.1}$$

where r and l are the strut radius and length. Dong et al.[34] performed an experimental study to explore mechanical properties of an octet-truss lattice made from Titanium alloy. A series of compression tests was conducted using specimens fabricated by snap-fit method. The work reveals that the compressive modulus and strength achieved by the lattices are significantly higher than that of other cellular materials, suggesting the lattice could be a promising candidate for weight efficient space filling materials.

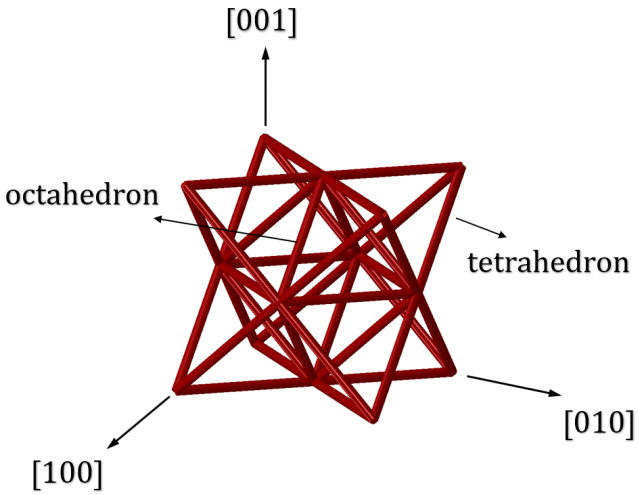

Figure 4.1: The octet-truss lattice for FCC configuration

This work explores the properties of the lattice in different lattice orientations in comparison to Dong et al.'s work. In such orientation, the lattice can be treated as stacking up of two-dimensional triangular lattices and rigid tetrahedral truss layers along Z direction, as shown in Figure 4.2. Hence the properties within the $X - Y$ plane are associated to the properties of two-dimensional triangular lattices explored in the Chapter 3. The property in the Z direction is determined by the behaviour of the tetrahedral structures. The unit cell configuration for this lattice orientation is shown in the Figure 4.2, where the cell width, n, and cell hight, k, are related to the cell size, l.

Three types of lattice orientation have been considered which are referred to as orientation-x, orientation-y and orientation-z. In Figure 4.3, the X, Y , Z axes represent the global coordinates of the model, while the x, y, z-axes represent the local coordinates of the lattice unit cell. For orientation-x, the x-axis in the local coordinate system is in parallel to the loading direction, corresponding to the Y-axis in the global coordinate. The same principle applies to orientation-y and orientation-z, where the unit cell was rotated 90° about z-axis and y-axis respectively.

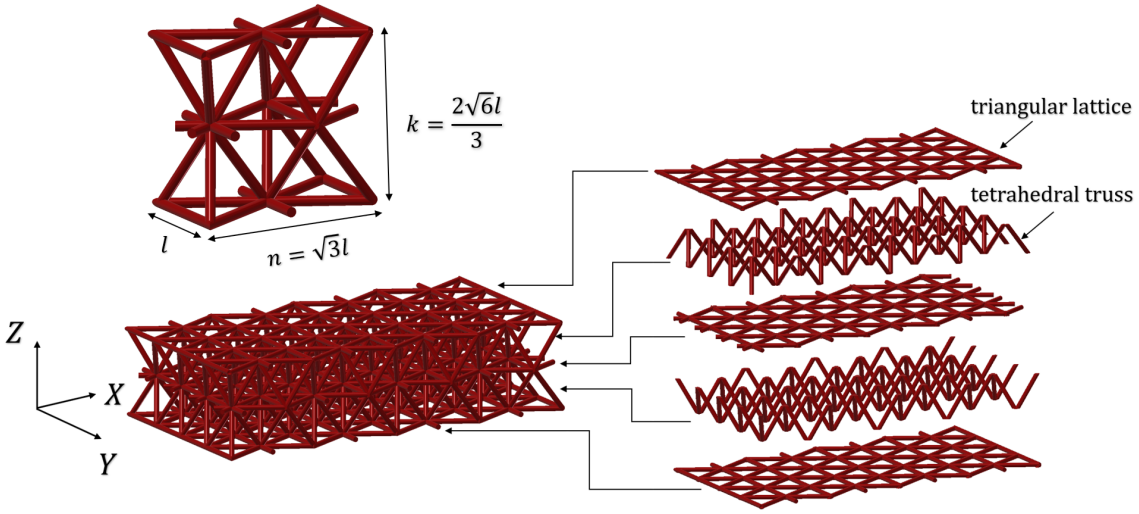

Figure 4.2: The octet-truss lattice for tetrahedral configuration

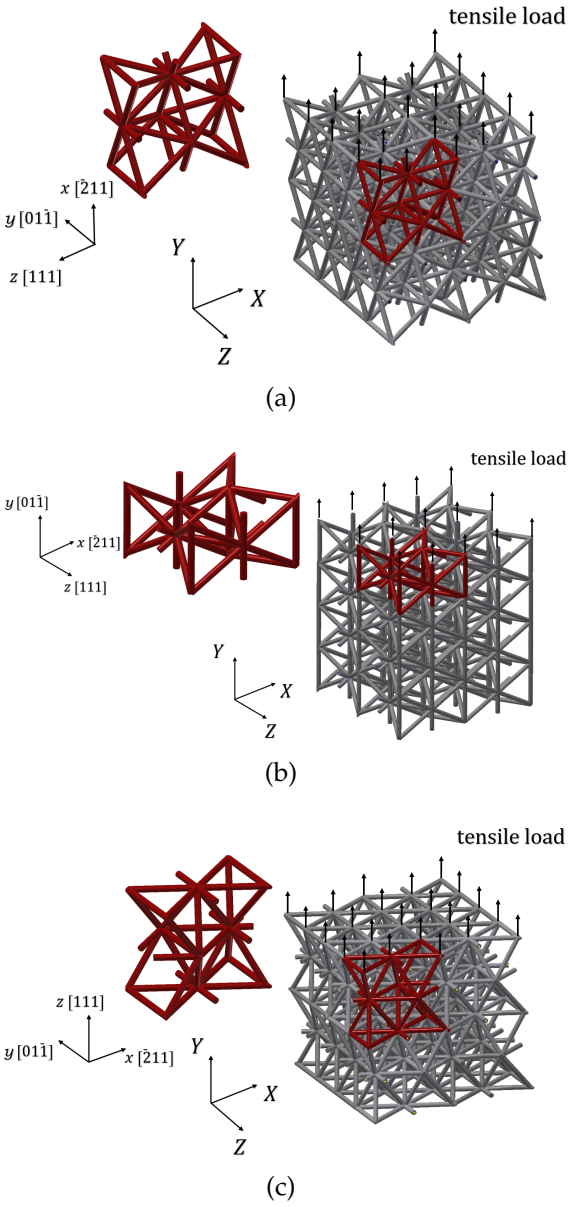

Figure 4.3: Definition of lattice orientations (a) orientation-x (b) orientation-y (c) orientation-z

4.3 Lattice strength

4.3.1 Analytical calculations

In the analytical model, each joint is treated as a frictionless hinge. The macroscopic load is predominantly balanced by tensile and compressive axial stresses within the struts. Previous work [76, 77, 78] has investigated the influence of the end conditions of the struts on the elastic modulus of the lattice. For some geometries, rigid end conditions lead to a higher lattice modulus, but for other geometries, including the octet-truss geometry studied in our work, the end conditions have little effect. Figure 4.4 shows that a change in structural orientation results in a different stress distribution within the structure, which leads to a dependence of lattice strength on orientation.

In the orientation-x structure the strength is mainly due to the triangular structures within the $x-y$ plane, as shown in Figure 4.4(a). The angled struts are under tension and the horizontal struts are in compression, while the struts between the triangular structures only have small contribution to strength. When the structure is sufficiently large compared to the cell size, then the structure contained in every unit space becomes identical to that shown in Figure 4.4(a). For this orientation the remote applied stress σ_∞ can be related to the axial stress in the struts σ_s by:

$$\sigma_\infty \frac{k}{2} l = 2\sigma_s \pi r^2 cos(\pi/6) \tag{4.2}$$

The strength of the orientation-x lattice, σ_t^X, can be obtained by substituting Eqn. (4.1) into Eqn. (4.2) and replacing the axial stress, σ_s, with the material failure stress, σ_f:

$$\sigma_t^x \approx 0.25\overline{\rho}\sigma_f \tag{4.3}$$

In the orientation-y structure the stress is distributed though struts which are parallel to the loading direction, as shown in Figure 4.4(b). Compared to the orientation-x and the orientation-z structures, it had the least number of struts contributing to the strength, and the relationship between σ_∞ and σ_s can be expressed by:

$$\sigma_\infty \frac{nk}{4} = \sigma_s \pi r^2 \tag{4.4}$$

Thus the strength of the orientation-y structure, σ_t^y, can be related to the relative density and the failure stress as:

$$\sigma_t^y \approx 0.17\overline{\rho}\sigma_f \tag{4.5}$$

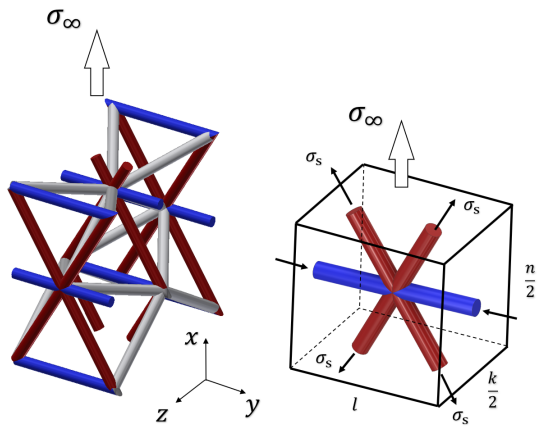

(a) orientation-x

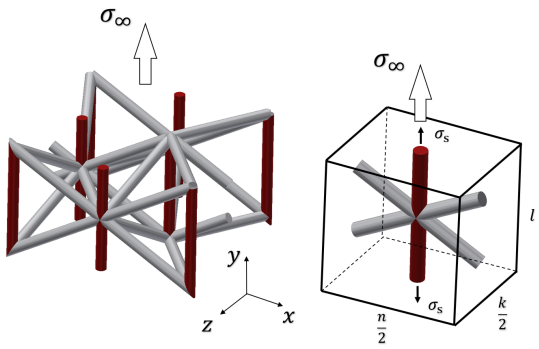

(b) orientation-y

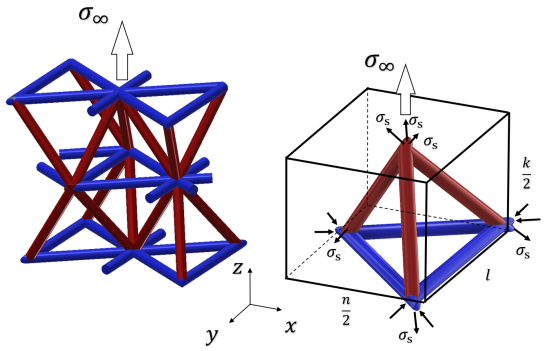

(c) orientation-z

Figure 4.4: Schematic of the unit cell stress states under tension along coordinate axes. Red, blue and grey colours indicate the struts which are in tension, compression and bending respectively

The orientation-z was found to be the only orientation where all components within the structure contributed to the strength. The triangular structures within the $x-y$ plane are under compression whereas the struts between the $X-Y$ planes are under tension. Thus, the remote applied stress, σ_∞, can be expressed as:

$$\sigma_\infty \frac{nl}{2} = 3\sigma_s \pi r^2 cos(0.6\pi) \tag{4.6}$$

Therefore, the strength of the orientation-z lattice, σ_t^z, can be obtained as follows:

$$\sigma_t^z \approx 0.34\overline{\rho}\sigma_f \tag{4.7}$$

4.3.2 FE analysis

FE analysis has been performed using the Abaqus FE system [79] to evaluate the modulus and strength of the lattice. Three sets of cuboid structures were created in orientation-x, orientation-y and orientation-z. For each orientation the models were made with various cross sectional areas. The model width, W, ranged between approximately $3l$ to $17l$, while the height, H, was kept at $20l$ for all models, as shown in Figure 4.5.

A point load was applied to each node at the top surface in the vertical direction, while vertical motion of the nodes at the bottom surface were constrained vertically, but allowing displacement in the lateral direction. The strut behaviour was modelled using 10 Timoshenko beam elements for each strut (Abaqus element type B31) with linear interpolation functions. This mesh refinement was sufficient to ensure mesh independence. The strut dimensions and material properties are listed in Table 4.1.

strut length, l	strut radius, r	modulus, E	Poisson's ratio, ν	failure stress, σ_f
10 mm	0.5 mm	70 GPa	0.33	140 MPa

Table 4.1: Strut dimensions and material properties.

The evaluated elastic modulus of the lattice was normalised by the relative density, $\overline{\rho}$, and the material modulus, E_s, as shown in Figure 4.6. A significant size effect was observed for the modulus of the orientation-x and orientation-y models, where the modulus reduces asymptotically with increasing model width, W/l. This is because in orientation-x and orientation-y models, the load was predominantly carried by the layers of triangular structures, as shown in Figure 4.2. The applied load was proportional to the number of layers of the triangular lattice,N, while the surface area was was proportional to, $N-1$. Hence, the tensile stress applied to a structure

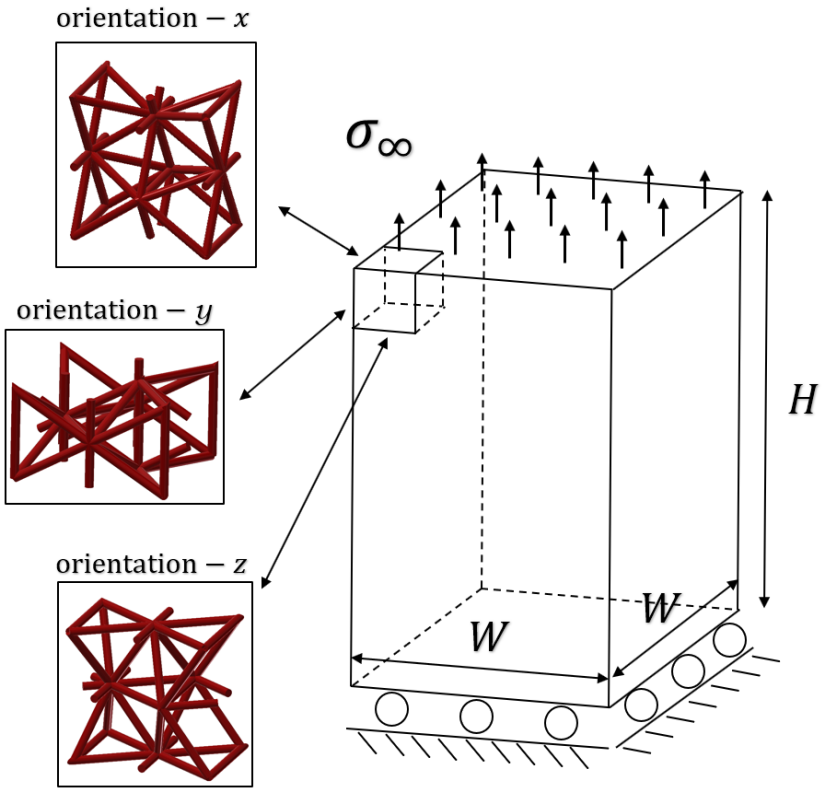

Figure 4.5: Rectangular FE lattice models for each of the three orientations.

with a small value of N, is higher than that to a large structure in order to achieve a same amount of extension. The modulus of the orientation-x and orientation-y models can be characterised as a function of model width:

$$\frac{E^*}{\overline{\rho}E_s} = 0.17(1 + \frac{3.5W/l + 2}{2.7(W/l)^2}) \tag{4.8}$$

The above expression was derived based on calculating the effective modulus of layers of equally spaced triangular lattices, which agreed well with the FE results. Hence, the asymptotic values shown in Figure 4.6 for the orientation-x and orientation-y models can be predicted from the Eqn. 4.8 by taking W/l to be large. The modulus of the orientation-z model was found to be independent of model size and was about 15% higher than that of the orientation-x and orientation-y models, as shown in Table 4.2. Furthermore, the Poisson's ratios of the lattice have also evaluated. These are found to be independent of the model size and are given by $v_{xy} = 0.33$, $v_{xz} = 0.25$ and $v_{yz} = 0.15$.

Figure 4.7 shows the normalised strength for the three lattice orientations. The strength of the orientation-x and orientation-y reduce with model width, W/l, due to the size effect described previously. The strength of the orientation-z was almost size-independent. A reduced strength was evaluated from model with a small W/l due to the edge effect; the cells at the free edge exhibited bending deformation, leading to a higher axial stress in the strut. However, this effect was only observed for model with $W/l < 10$.

It was also found the analytical predictions, derived for infinite lattices, agree well with the numerical predictions for model with, $W/l > 14$. The asymptotic value of strength for each orientation are shown in Table 4.2, where the strength of orientation-z is about 35% higher than that of orientation-x and double that of orientation-y structure.

mech. prop	orientation-x	orientation-y	orientation-z
$E^*/(\overline{\rho}E_s)$	0.17	0.17	0.20
$\sigma_t/(\overline{\rho}\sigma_f)$	0.25	0.17	0.34

Table 4.2: Mechanical properties of the lattice in three orientations.

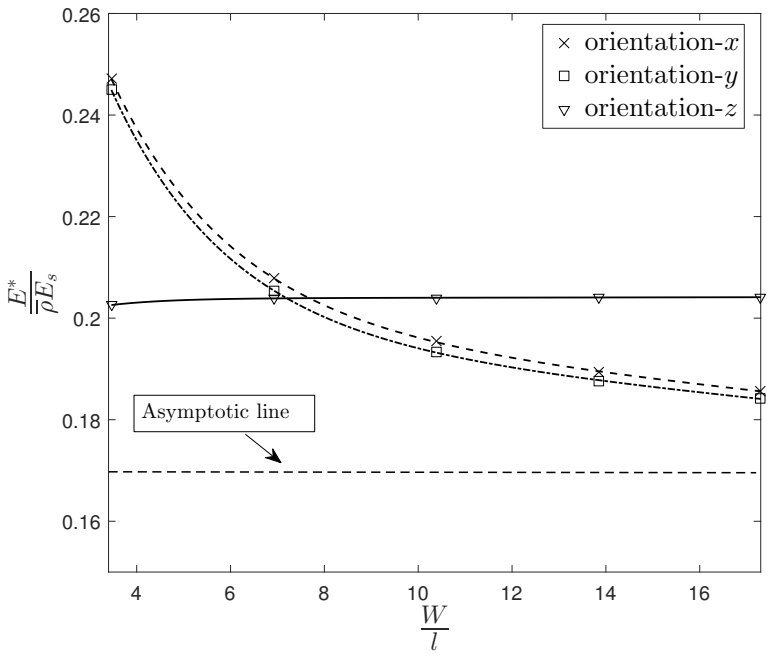

Figure 4.6: The normalised modulus versus normalised model size for the three orientations. The horizontal line indicates the asymptotic value of the orientation-x and -y curves.

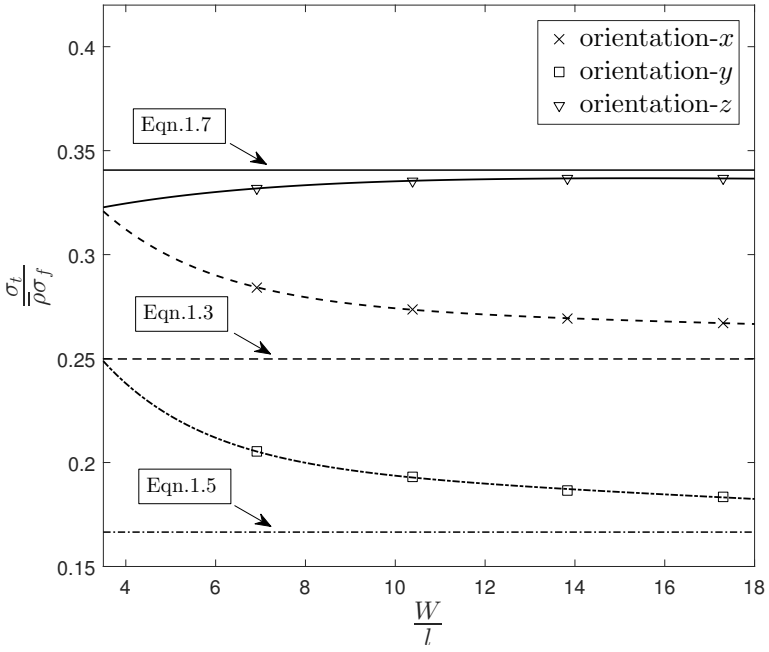

Figure 4.7: The normalised FE predicted strength of lattice versus normalised model size. The horizontal lines are the analytical results.

4.4 Experiment

4.4.1 Specimen preparation

The aim of the experiment is to characterise the strength and modulus of the lattices in different orientations and validate the numerical predictions. According to the previous analysis, a very large specimen is required to achieve the size-independent material properties given in Table 4.2 , which is difficult to achieve in practice. Hence, an experiment was conducted using finite-sized specimens which was designed as a cube with width $W/l \approx 5$, as shown in Figure 4.8. The strut radius and length were equal to 1mm and 10mm, sufficiently large to be accurately fabricated. The specimens were made from photo-polymer resin, and manufactured using stereolithography(SL), which is an additive manufacturing technique first introduced in 1984 for rapid prototyping[80]. This technique is worked by focusing an ultraviolet (UV) laser onto a layer of liquid mono-polymer resin, which is then selectively solidified through photo-polymerization[81] to build a layer of geometry. Scan speed, hatching spacing, layer thickness, and diameter of laser beam are key processing parameters to determine the sample quality. A detailed explanation of the influence of these parameters has been presented by Lee et al.[82]. Among these parameters, the layer thickness has a particular significance in the surface roughness. A small layer thickness results in a better surface quality, but will significantly extend the build time.

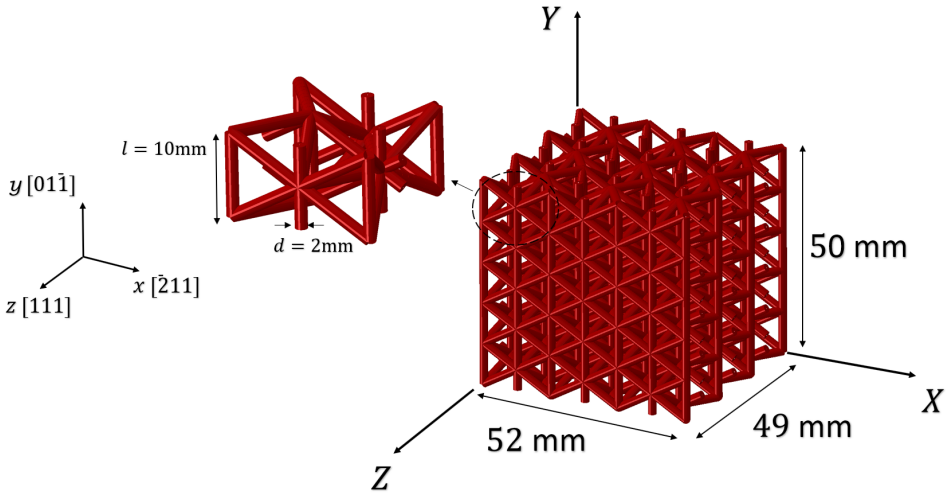

Figure 4.8: Lattice sample designed for compression test.

An SLA660 rapid prototyping machine was used in this study equipped with a chamber size of 600mm x 600mm x 300mm. The laser scanning speed and power were chosen to be 6000 mm/s and 0.8 Watt. The diameter of spot size and layer thickness were chosen to be 0.1mm and 0.075mm to achieve a good surface condition. The strut length, l, and diameter, d, of the manufactured specimens were measured using a vernier caliper. 10 measurements were taken from randomly selected struts for each specimen. A good surface quality and dimensional accuracy was found such that the measured l and t were almost identical to the targeted parameters, as shown in Table 4.3.

Figure 4.9 shows the stress-strain curve of the photo-polymer resin used in this study, which was measured from a 3D printed standard dog-bone specimen with a gauge length of 12.5mm. The modulus, yield strength and ultimate tensile strength(UTS) of the resin were therefore determined, as shown in Table 4.3. It was found the resin ruptures in a relatively brittle manner with the failure strain of 5%.

strut length, l	strut diameter, d	relative density, $\overline{\rho}$	Modulus E, MPa	Tensile strength, MPa	Failure strain
10 mm	2.1 mm	0.29	3000	58	0.05

Table 4.3: Strut dimensions and material properties.

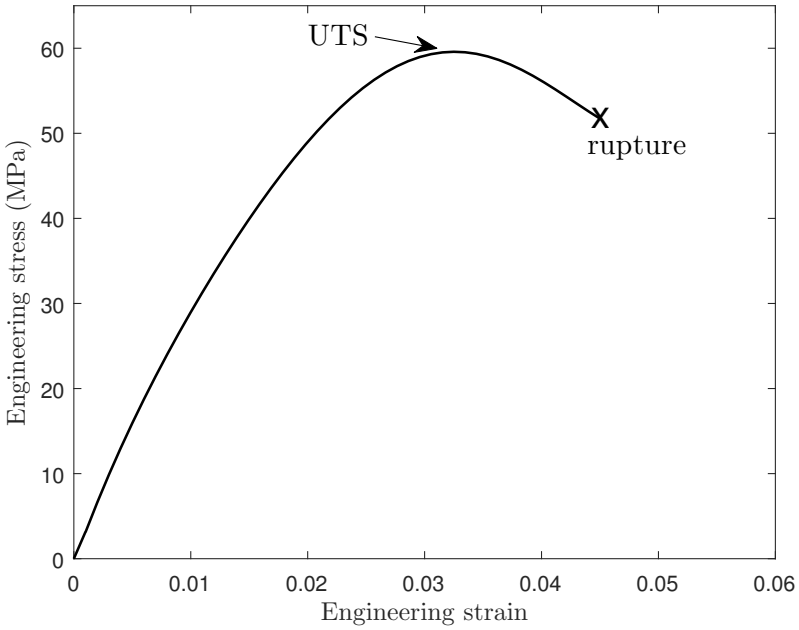

Figure 4.9: Stress-strain behaviour of the photo-polymer resin.

4.4.2 Compression test

A compression test was carried out in this study, as it is straightforward to apply a compressive load on the specimen. Despite the analytical predictions given in the section 4.3.1 were derived under a tensile load, the obtained results are also applicable for predicting the compressive strength considering the stress states illustrated in Figure 4.4.

The specimens were loaded in three different orientations: orientation-x,orientation-y and orientation-z structures, as shown in Figure 4.10. Three specimens were tested for each orientation. All tests were performed using an Instron 50kN tensile/compression test machine, with a loading rate of 2mm/min to ensure a static deformation. A smooth plate was installed at the grip to minimise friction force at the contact surfaces which allowed the specimens to be free to expand in the laterally direction.

The grip was connected to a self-aligning loading block with a spherical bearing and the specimens were carefully located at the center of the plate to ensure the displacement was uniformly applied to the specimen without any possible influences from eccentricity. The lattice deformation was characterised using a video gauge system, which was used to track the displacements of pre-defined points on the specimens, as shown in Figure 4.10. The background of this technique has been described in Chapter 3. The measured displacements were then used to calculate the axial and lateral strain of the lattices.

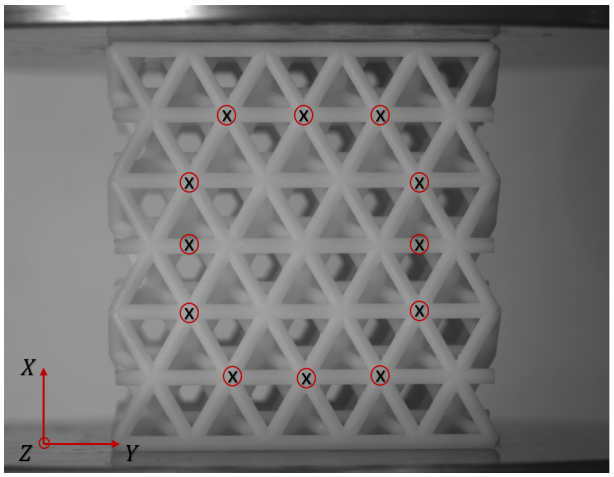

(a)

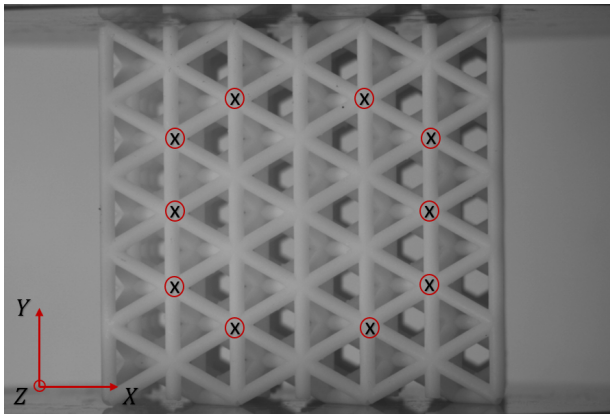

(b)

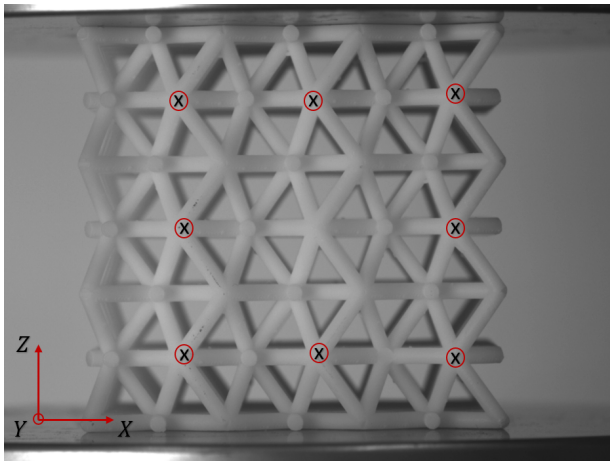

(c)

Figure 4.10: Compressive test for different lattice orientations (a) orientation-x (b) orientation-y (c) orientation-z

4.5 Results and discussion

4.5.1 Compressive response

Figure 4.11, 4.12 and 4.13 show the measured stress-strain curves for each lattice orientation. A high repeatability is observed between these measurements. The nominal stress was calculated as dividing the applied load by the original cross sectional area, while the nominal strain was obtained by the ratio of the measured compressive displacement and the undeformed gauge length. Figure 4.14 compares the measured results between three lattice orientations. After the peak load was reached, the failure of orientation-x and orientation-z specimens were catastrophic due to the brittleness of the material. Hence, there was no failure mechanism and failure path observed from the tests.

Figure 4.14 compares the stress-strain curves measured from the three orientations. For the orientation-x specimens, the stress-strain increases linearly followed by a non-linear region corresponding to the strut yielding at the contact surface between the specimen and the metal plate shown in Figure 4.14. The stress continues to increase until fracture occur at the tensile loaded struts. In contrast to the orientation-x, there is no fracture observed in the orientation-y specimens. The peak stress was reached when the vertical struts started to yield. Continued loading eventually caused strut buckling, leading to a structure densification and strain hardening. For the orientation-z specimens, the stress-strain responses are almost linear before reaching to its peak stress.

4.5.2 Comparison of predictions with measurements

The Table 4.4 compared between the numerical predictions and the mean values of measured modulus and strength obtained from Figure 4.11, 4.12 and 4.13. A reasonable agreement was achieved. The highest strength is measured from the orientation-z specimen, which is double that of the orientation-y and 40% higher than the orientation-x specimens. The measured Poisson's ratios are given by $v_{xy} = 0.37$ and $v_{xz} = 0.25$ which are almost consistent with the numerical predictions given in the section 4.3.2.

mech. prop	orientation-x	orientation-y	orientation-z
$E_{exp}/(\overline{\rho}E_s)$	0.24	0.25	0.22
$E_{FE}/(\overline{\rho}E_s)$	0.22	0.22	0.20
$\sigma_{exp}/(\overline{\rho}\sigma_f)$	0.28	0.23	0.35
$\sigma_{FE}/(\overline{\rho}\sigma_f)$	0.30	0.22	0.33

Table 4.4: Comparison of measured properties with numerical prediction for lattice with $W/l = 5$.

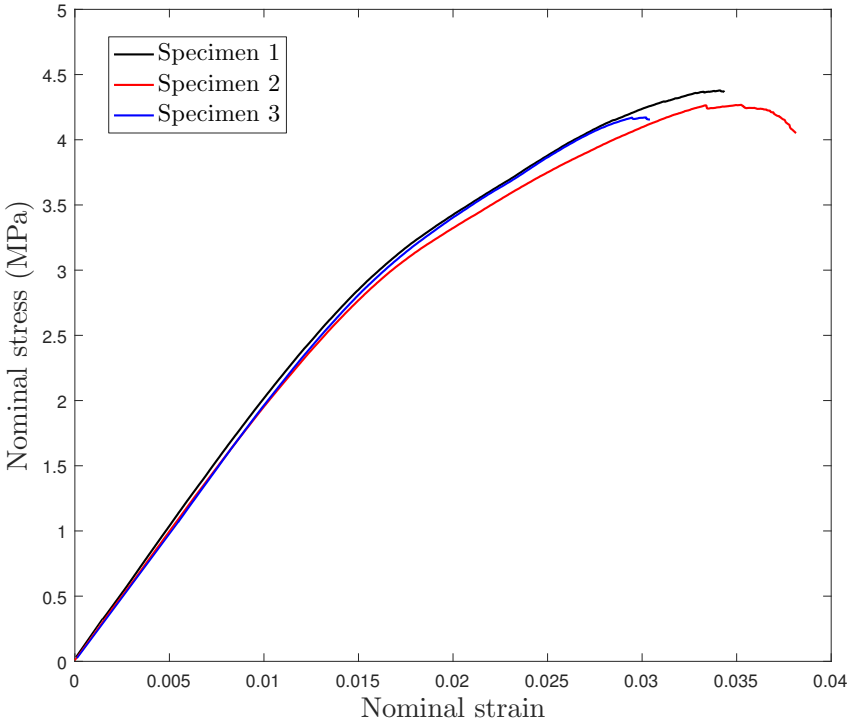

Figure 4.11: Measured stress-strain curves for orientation-x specimens.

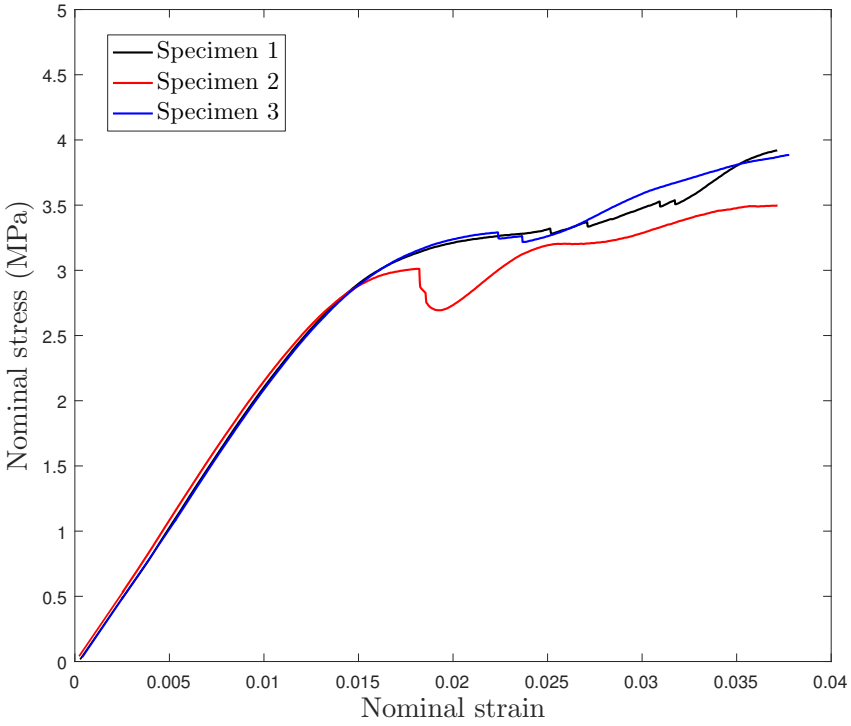

Figure 4.12: Measured stress-strain curves for orientation-y specimens.

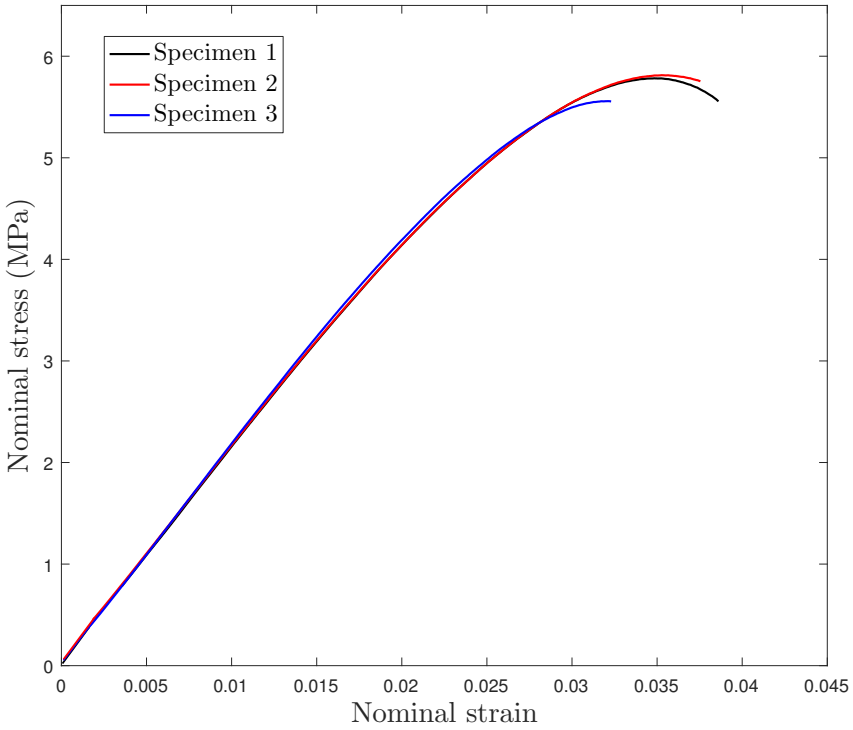

Figure 4.13: Measured stress-strain curves for orientation-z specimens.

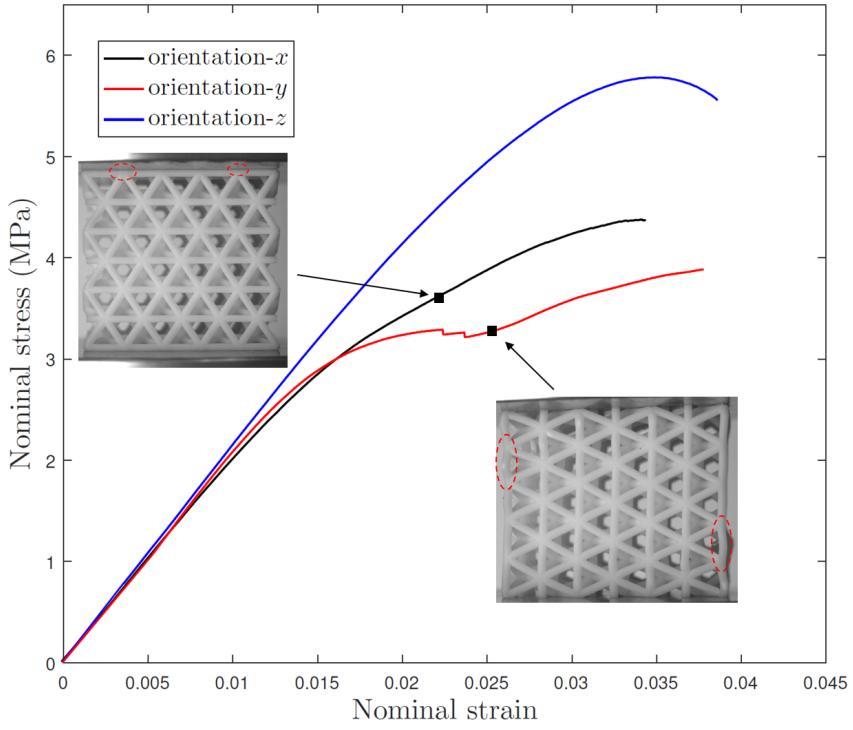

Figure 4.14: Comparison of stress-strain curves for three orientations.

Two factors are likely to contribute to the discrepancy between the measured results and the numerical predictions. First the specimen properties could be varied for different struts due to the different build directions in the fabrication process. The local struts are aligned in multiple directions in the specimens leading to the different yield strength possessed by each strut. However, it is beyond the scope of this dissertation to assess the significance of the build direction on mechanical properties of the lattices. Detailed interpretation of the build direction effect can be found in the work presented by Taufik and Jain[83] where the physics of the phenomenon has been described. Then the non-linear stress-strain response exhibited by the resin is also detrimental to accuracy of the numerical predictions. The yielding process before rupture is not taken into account in the numerical models which is likely to be the cause of the higher strength measured from the experiment compared to the FE results.

4.5.3 Compressive strength

When a compressive load applied to the lattice, a low density specimen could collapse by the buckling of the out-of-plane struts, while the failure of a high density specimen was caused by the inelastic buckling or plastic yielding of the struts [34]. In this study, the specimens are made with relatively thick struts(high relative density) and buckling was only observed in the orientation-y specimens during the experiment. To examine if the buckling occurred prior to strut yielding, an analytical prediction of the buckling stress is carried out for the orientation-y specimen using the expression:

$$\sigma_b \frac{nk}{4} = \frac{\pi^2 EI}{(K_e l)^2} \tag{4.9}$$

The left term in the above expression is the load carried by each unit cell. The right term is the Euler's critical load[84] where the second moment of area $I = \pi r^4/4$. Since the lattice was assumed to be pin-jointed in the analytical model, the effective length factor K_e was chosen to be 1. The buckling stress, σ_b, was therefore expressed as:

$$\sigma_b = \frac{\pi^3 E}{2\sqrt{2}} (\frac{r}{l})^4 \tag{4.10}$$

The compressive strength, σ_c, can be calculated by substituting material parameters given in the Table 4.3 into the Eqn.4.5. The calculated buckling stress and compressive strength were found to be 3.2 MPa and 2.8 MPa respectively. Therefore the predicted buckling stress, σ_b, was about 15% higher than the compressive strength, σ_c, indicating the lattice yielding was occurred prior to strut buckling.

4.6 Concluding remarks

This chapter describes the mechanical properties of the octet-truss lattices. It started with an analytical and numerical approach to investigate the strength, modulus and Poisson's ratio, followed by a demonstration of the influence of lattice orientation and size on its mechanical properties.

It was found that the lattice strength was orientation dependent, while the modulus was relatively isotropic. The orientation-z model exhibits the highest strength which is about 40% higher than that of orientation-x and double that of the orientation-y model. The model size had a particular significance for the properties of orientation-x and orientation-y models. Their strength and modulus reduced by 15% and 20%, when model size, W/l, increased from 4 to 16. The properties of the orientation-z model were almost size-independent.

An experimental study was carried out using a set of additive manufactured lattice specimens. A good agreement was found between the measured results and numerical predictions. Hence the validity of the numerical predictions were assured. The failure of orientation-x and orientation-z specimens were catastrophic, while the orientation-y specimen exhibited significant buckling after plastic yielding. Figure 4.15 shows the material property charts for modulus and yield strength, where the measured results are compared with other categories of materials. It shows that the modulus and strength of the polymer octet-truss lattices are significantly lower than the results measured from the Aluminium triangular lattices described in the Chapter 3, but are comparable to the properties of foams and natural materials at the density of 300 kg/m^3.

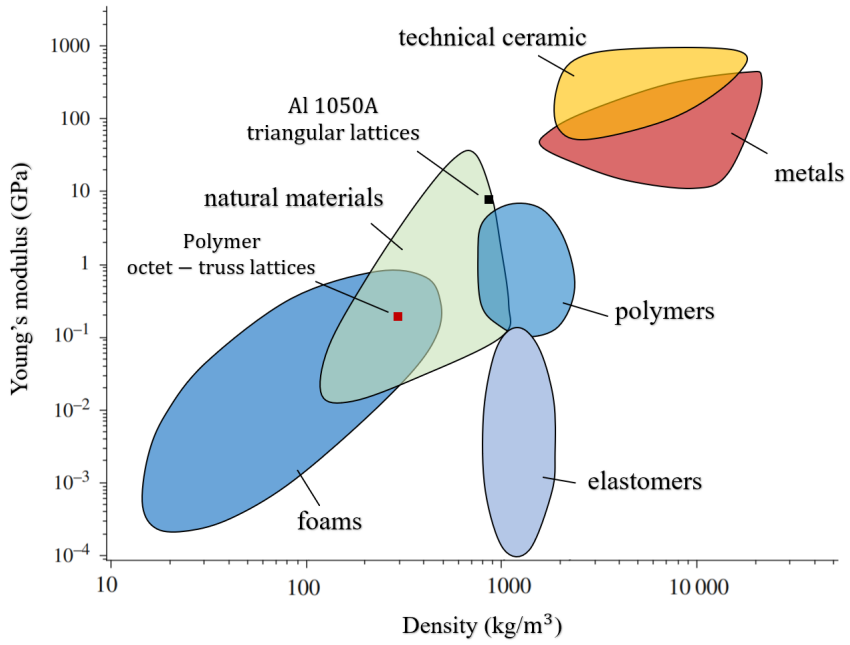

(a)

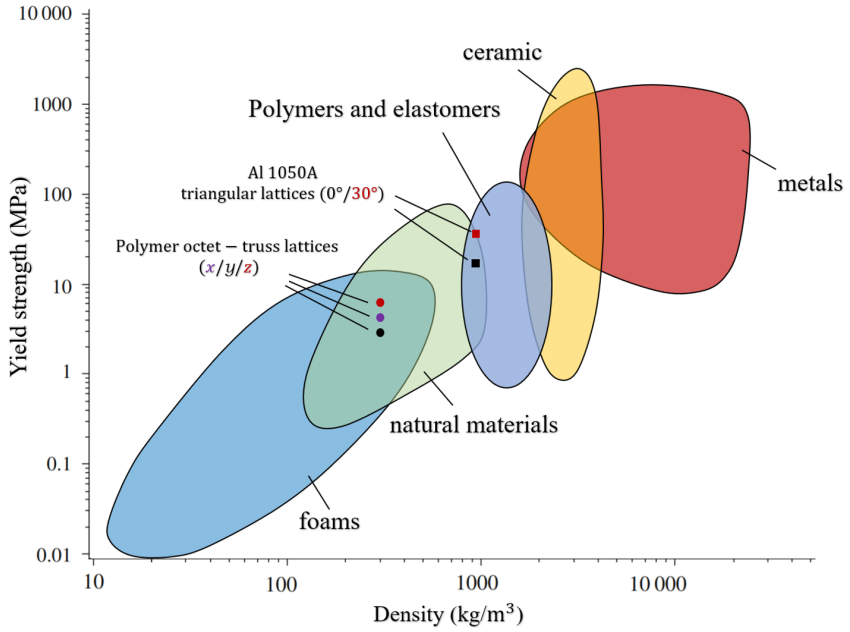

(b)

Figure 4.15: Material property chart for Young's modulus and yield strength

Chapter 5

Fracture behaviours of 3D lattices

5.1 Introduction

This chapter presents a comprehensive study of fracture behaviours of the octet-truss lattice. First a series of experiments is performed to measure the fracture toughness and load-displacement responses of the lattices. The specimen geometry is defined based on ASTM E399 and fabricated using an additive manufacturing technique. Detailed manufacturing processes are provided including a description of heat treatment and artificial aging.

Next X-ray computed tomography(XCT) is conducted to assess the quality of the specimens in terms of the dimensional accuracy and porosity contained in the struts. The stress-stain curve of the material is then determined from a tensile test.

The experiment method such as the loading pattern, test configurations and measurement techniques are described. The experiment results are presented next and compared with numerical predictions. The fracture resistance is calculated during crack extension using a standard method described in the ASTM E399. Then a set of numerical analyses is performed to investigate the effect of specimen size on the toughness and assess the validity of the measured toughness.

Then, the influence of specimen geometry on toughness is investigated. The toughness is evaluated from various model geometries including compact tension(CT), single edge notch tension(SENT), single edge notch bending(SENB) and thumbnail crack models. The significance of the crack tip constraint has been explored using a boundary layer analysis(BLA). Finally, a series of simulations of crack growth has been performed to predict crack paths and post-fracture responses for different lattice orientations and model geometries.

5.2 Experiment

5.2.1 Specimen design

The aim of the experiment is to characterise fracture behaviours of the lattice. Compact tension (CT) fracture specimens were chosen for this study, as the geometry allows a relatively stable crack growth which enables fracture behaviours to be monitored during crack extension [85].

Specimens were created for orientation-y and orientation-z lattices shown in Figure 5.1 where the Miller indices are given based on the coordinate system defined in Chapter 4. Two types of specimens were designed with almost identical dimensions to eliminate the influence from the specimen size. The CT specimen geometry followed the ASTM E399 which requires knife edges on the crack mouth rather than the load line compared to the geometry given by ASTM E1820 [54]. The nominal strut length, l, and diameter, d, were equal to 5 mm, and 0.5 mm. The strut radius was designed to be large enough to ensure the manufacturability for the lattice fabrication technique, while the strut length was chosen to achieve a reasonable aspect ratio such that each strut behaviour can be adequately simulated as a beam.

The specimen dimensions shown in Figure 5.2 were chosen to achieve a reasonably high ratio of W to l in order to reach an asymptotic value of toughness [86]. Two solid rings were built around the pin holes to strengthen the local structure. Two thin plates with knife edges were bonded to the front face of each specimen to allow measurement of crack mouth opening displacement(CMOD).

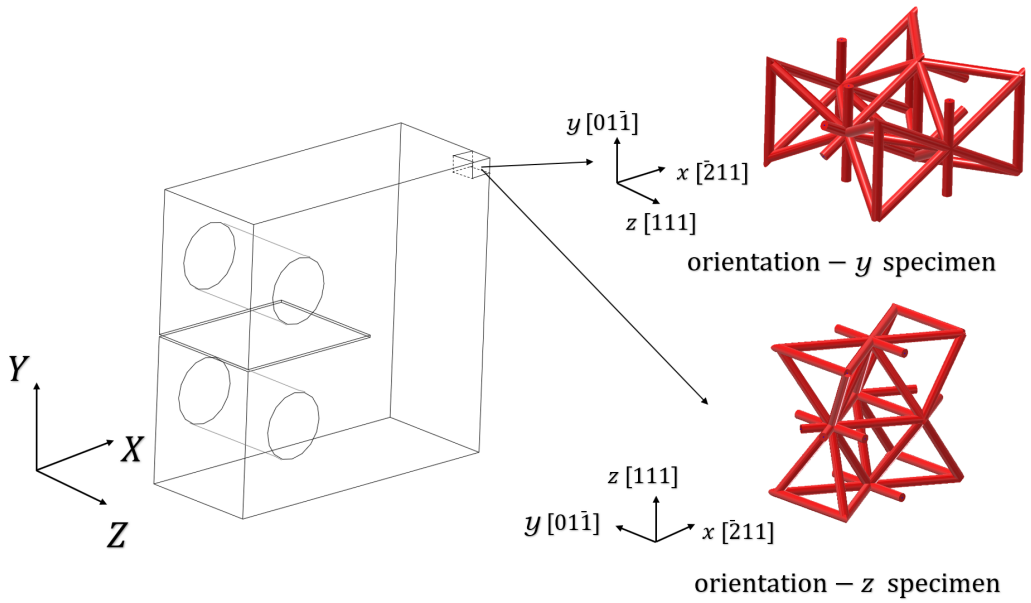

Figure 5.1: Definition of specimen orientations

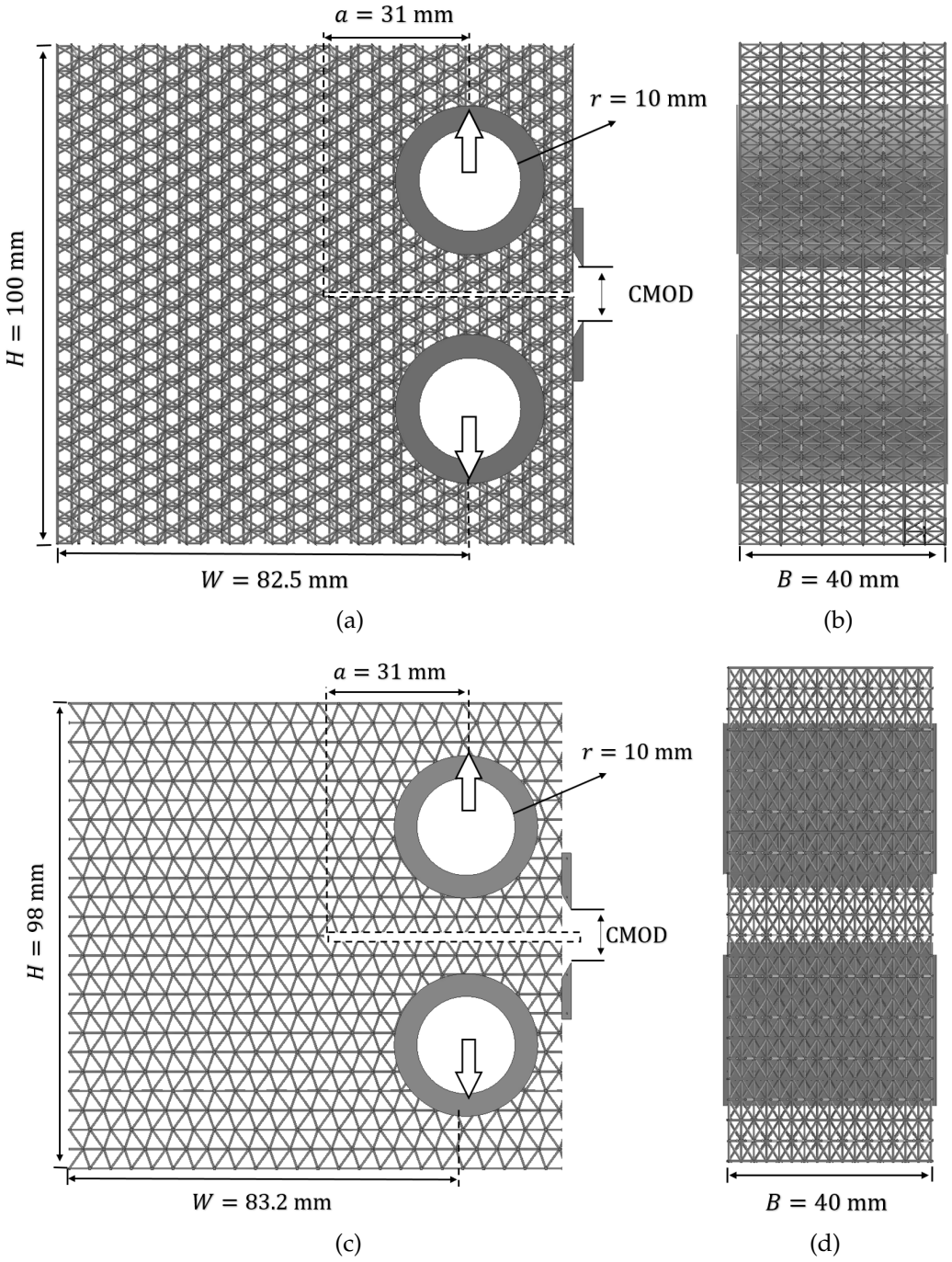

Figure 5.2: Designed specimens geometry with $\frac{a}{W} = 0.38$: (a)(b) are side and front view of an orientation-y specimen;(c)(d) are that for an orientation-z specimen.

5.2.2 Selective laser melting technique

Selective laser melting (SLM) technique is a layer manufacturing process which developed in late 1980s for rapid prototyping[87], so that complex geometries can be directly manufactured from computer designed models. The pre-work involves creating of a CAD model and storing the geometry data into a STereoLithography (STL) file, which is then processed to provide slice data for the manufacturing process.

The SLM process worked by selectively melting metal powder using a high energy laser beam. The melted metal is then solidified after it cools down to form a layer of solid geometry. When a layer of scan is completed, the working platform moves down to start creating another layer of solid. This process is repeated until the whole part is completely built. After the scanning process is finished, the residual powder is discarded.

The key parameters of the SLM process include scan power, scan speed, hatch space and layer thickness. The fabrication process involves heating and melting, hence the heat input during the scanning is critical as it determines the degree of consolidation of the powders. Insufficient heat input, caused by low laser power, high scan speed, and high layer thickness results in incomplete wetting of particles and leads to the balling phenomenon[88, 89]. The balling phenomenon involves formation of spheroidal beads during solidification, which causes detrimental effect on sample qualities such as poor surface roughness and high porosity. The complex physics of the balling phenomenon is provided in [90]. However when powders are overheated resulting from the high laser power and slow scanning speed, the keyhole effect occurs due to the extensive material evaporation[91]. Moreover, a poor hatch space often causes porosity due to incomplete fusion of powders between two melt lines. Hence a good combination of the key parameters is the essential to determine the quality of built part.

Recently there has been much interest in applying the SLM technique for the fabrication of three-dimensional lattices. The influence of processing parameters on dimensional accuracy of strut was investigated by by Qiu et.al.[66] using AlSi10Mg metal powder. The study carried out by comparing struts dimension and porosity within struts fabricated at different scanning speed and power levels. It was found that the strut thickness linearly increased with laser power, provided the scanning speed remained constant at 7000mm/s. Also the strut fabricated at laser power higher than 150W results in a greater strut thickness compared to the target thickness of 0.3 mm.

The porosity within struts was found to be low at both low(150W) and high(400W) laser power, while a high porosity was observed in sample when a intermediate power level(200W-300W) was used. When the laser power was constant, the strut thickness was found to reduce with increasing scanning speed. The study also suggested that an intermediate scanning speed (3000mm/s - 5000mm/s) causes a high porosity level and should be avoided.

In this study, specimens as shown in Figure.5.3 is fabricated at the University of Birmingham using a SLM solution Gmbh SLM500HL L-PBF machine equipped with 2 sets of 1000W laser, 2 sets of 400W laser and 2 sets of scanning lens systems. The 400W laser was chosen for the lattice manufacturing to ensure a better geometry accuracy due to its small spot size of about 90µm in diameter. The hatch space and layer thickness are chosen to be 100µm and 30µm. A205 aluminium alloy metal powder was used for specimen production[92]. The metal powder was produced by EIGA (Electrode induction melting gas atomiser) by the TLS Company with particle sizes ranging from 15µm to 53µm.

Specimens were produced at a constant laser scanning speed of 1650 mm/s with laser power of 350W. 150°C preheating was used to reduce residual stress during manufacturing and achieve good density[93]. The substrate and build chamber were preheated to 150°C for 3 hours and maintained at the same temperature during the building process to reduce residual stress developed in the specimens. The oxygen level was controlled up to lower than 0.17% by flooding Argon gas into the chamber so as to avoid formation of oxides.

After manufacture, specimens were manually removed from the substrate plate and subjected to T6 heat treatment. Specimens were solution treated at 521°C for 17 hours followed by water quenching. This process aimed to homogenise the micro-structure and chemical composition, especially for copper and magnesium elements. Aging treatment was then conducted for 22 hours at 170°C to allow precipitation of incoherent θ- phase and coherent Ω-phase which are the most effective strengthening phases in Al-Cu-Mg-Ag alloy [94, 95].

Finally, a pre-crack was introduced into each specimen using wire Electrical Discharge Machining (EDM). The EDM technique was found to be able to produce a smooth and clean cut into the specimens without damage or deformation of struts in the vicinity of the cutting path. A wire of a diameter of 0.1mm was chosen to enable accurate crack location.

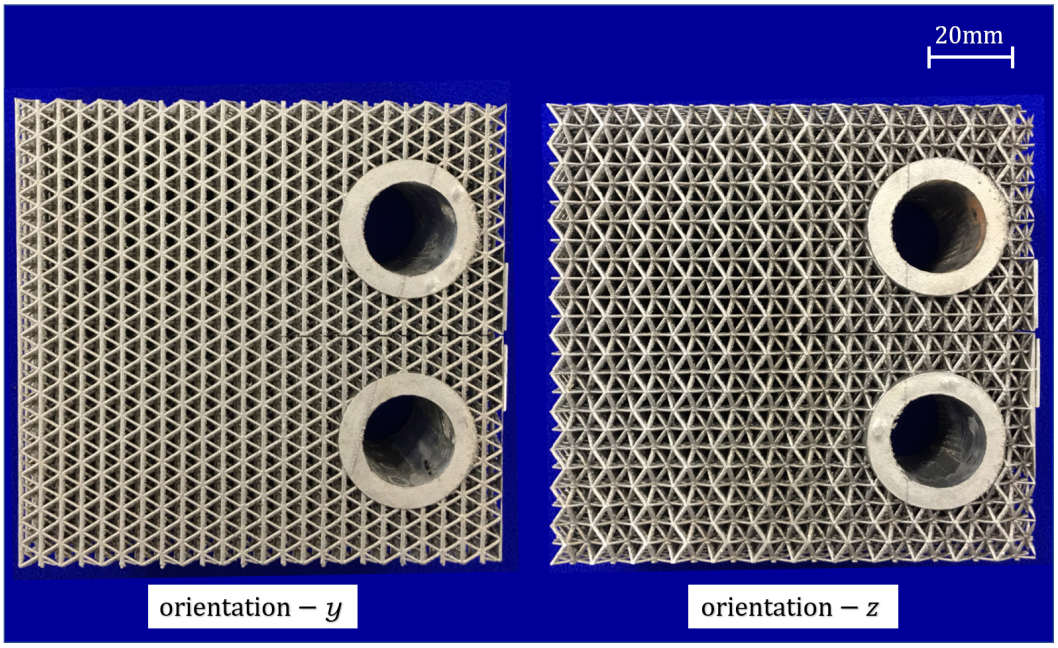

Figure 5.3: Specimen manufactured by SLM technique

5.2.3 X-ray computed tomography

The X-ray computed tomography technique enables characterisation of material internal features by evaluating intensity attenuation of X-ray which are directing on to the specimen from multiple angles. The attenuation is characterised by the Beer's Law[96]

$$I = I_0 e^{-\mu x} \tag{5.1}$$

where I and I_0 are the initial and final intensity of X-ray. μ is the linear attenuation coefficient of the material. x is the length of X-ray path. The measured linear attenuation coefficients of the sample from different directions are then used to reconstruct three-dimensional volume through a set of reconstruction algorithms described by Hsieh[97]. The elements of the technique consists of an X-ray source and a series of detectors to characterise the X-ray intensity.

The aim of X-ray computed tomography conducted in this study is to assess specimen qualities including dimensional accuracy and porosity. The size of the specimen was found to be too large to allow images to be constructed with a reasonable resolution. Therefore, a scan was performed on a small lattice cube with an edge of length 26.5 mm, as shown in Figure 5.4(a), designed with identical strut dimensions and manufactured in the same chamber as the CT specimens.

The X-ray computed tomography was performed using a Zeiss X-Radia 520 Versa scanner. Both low and high magnification scans were performed to measure the strut length, l, and diameter, d, shown in Figure 5.4 and evaluate the porosity shown in Figure 5.5. The resolution of the low magnification scan was 25.22 µm/pixel, while the corresponding one for the high magnification scan was 3.57 µm/pixel.

The strut dimensions were selectively measured on a proportion of the two-dimensional images (Orthoslices) used to stack the three-dimensional volume of the probed material (the low magnification scan). Image processing software Avizo[98] was used for processing. A significant surface roughness was noticed on the upper surface of the strut shown in Figure 5.5, caused by the non-melted particles loosely attached to the strut. Hence the orthoslices image of $X - Z$ plane was used for characterising strut dimensions to minimise the influence of surface condition. Twenty different locations were investigated per 2D image to extract the mean values for the strut length and diameter.

It was found that good accuracy was achieved by the lattice manufacturing process for the strut length, l, however the measured strut diameter d ranged from 0.79 mm to 0.82 mm, significantly higher than the original design, as shown in Table 5.1. This is the most likely caused by the slow scanning speed chosen for the manufacturing process. Pores were observed from the result of high magnification scan, which were almost evenly distributed though-out the strut. The porosity was evaluated by isolating the pore areas within the matrix, shown in Figure 5.5(b). The volume of the pore area and the scanned matrix were both evaluated to calculate a sample porosity which was equal to 2.2%.

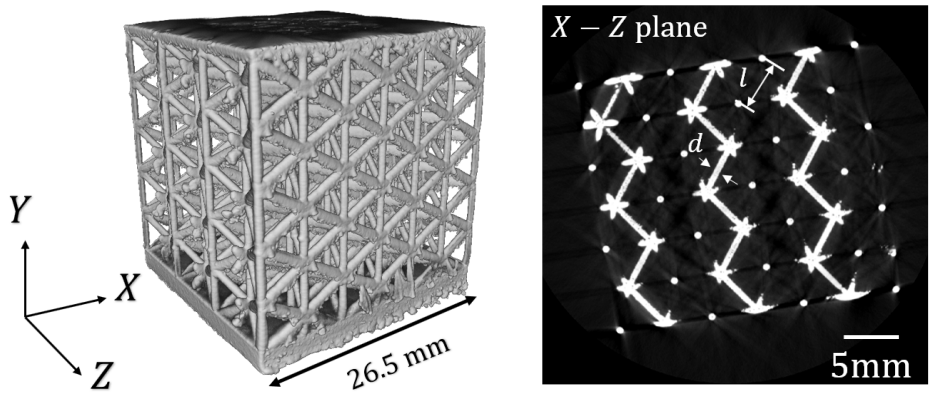

(a) (b)

Figure 5.4: Result of X-ray computed tomography with low magnification:(a) volume of the entire sample probed; (b) typical 2D orthoslice image (X-Z plane) of the sample across its height (Y-axis).

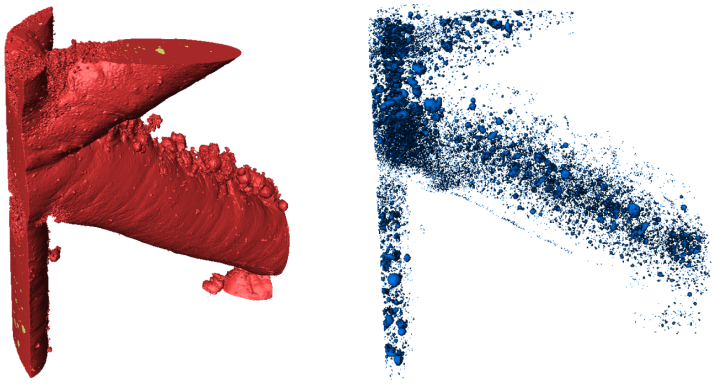

(a) (b)

Figure 5.5: 3D volume of the sample being probed using high magnification:(a) entire probed volume illustrating the exterior surface (pores and matrix shown in yellow and red colour respectively; (b) pore network within the scanned area.

	diameter,d	Strut length,l	Relative density, $\overline{\rho}$	Porosity
Nominal	0.5mm	5mm	0.067	2.2%
Measured	0.79-0.82mm	5mm	0.17	

Table 5.1: Measured strut dimensions and porosity

5.2.4 Tensile test

A solid round bar specimen was chosen for the tensile test to determine the material stress-strain response. Measuring the response of a single strut cut from the specimen was discounted because the surface roughness of the strut would result in significant uncertainty of the cross-sectional area. The round bar was fabricated using the same process parameters as the lattice specimens and was built vertically along the longitudinal direction. The sample was then machined into a standard dog-bone geometry with gauge length of 25 mm and diameter of 6 mm. The strain was measured by 25 mm Instron extensometer[99] and the applied load was acquired from a 50 kN load cell.

The measured stress-strain curve is shown in Figure 5.6, where the modulus and ultimate tensile strength were measured to be 63 GPa and 320 MPa. It was found that the modulus was lower than that would be expected for an aluminium alloy, likely to be caused by porosity within the specimen. Various models were developed to characterise the influence of pore shape and distribution on modulus [100, 101]. Wang[100] expressed the relation

between the porosity and modulus of aluminium alloy as:

$$E = E_0 e^{-(bp+cp^2)} \tag{5.2}$$

where b and c are the material constants. The E_0 is the modulus for material with zero porosity, and the p is the porosity. The study suggests that an approximately 10% reduction in modulus is possibly to be achieved by 2% of isolated closed pores.

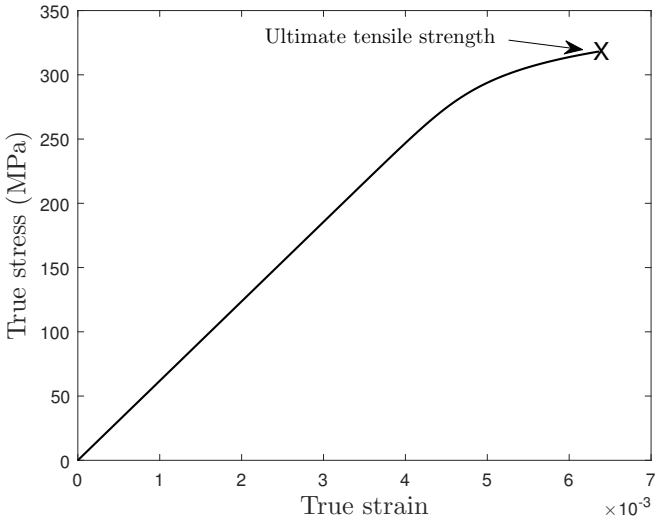

Figure 5.6: stress-strain curve of parent material measured from round bar tensile test

5.2.5 Fracture test

Fracture tests were carried out using the apparatus illustrated in Figure 5.7. The clevises was assembled with 6 mm Aluminium (Al6082) plates, strong enough to carry the fracture load required for lattice specimens and provided flexibility to accommodate specimens made with various thickness. A periodic loading pattern was used so that the specimen compliance could be measured as the crack extended. In each cycle, loading was applied so that the crack mouth opening displacement (CMOD) increased by 0.5 mm followed by unloading to reduce the CMOD by 0.25 mm. This pattern of loading allowed small increments of displacement applied to the specimen, aiming to capture as many as possible analysis points on the Load-CMOD curve. The rate of loading and unloading were set to 0.2 mm/min, to maintain a static deformation rate[102]. An Instron 2670-132 extensometer[103] with gauge length 10 mm was used to measure crack mouth opening displacement (CMOD) which was installed at the specimen knife edges with care to centre the gauge preventing eccentricity. The crack extension was tracked by an iMETRUM video gauge system [72], described in Chapter 3.

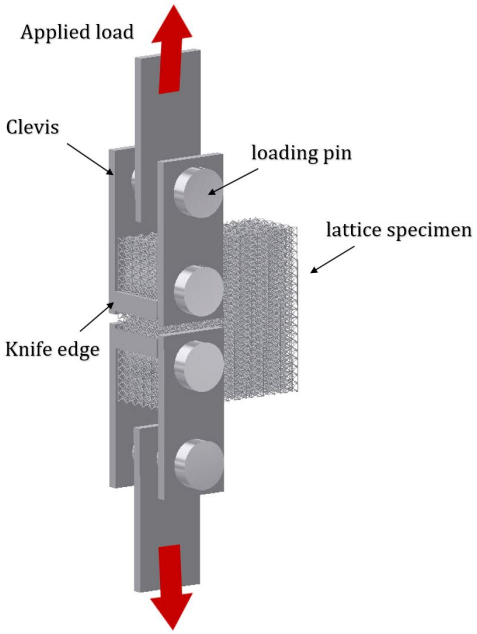

Figure 5.7: Experiment set up

5.3 Results and discussion

Fracture tests were conducted for two orientation-y specimens and three orientation-z specimens. The load-displacement responses are shown in Figure 5.8 and 5.9. There is reasonably good repeatability, particularly for the peak load. Figure 5.10 compares load-displacement curves for different orientations: orientation-y (specimen 2) and orientation-z (specimen 3). An increase in critical load can be observed for both orientations with crack extension. The point a in Figure 5.10 indicates the initial critical load where failure was observed at struts ahead of the initial crack tip, while point b indicates the peak load. Struts A and B in Figure 5.11 shows the location of failed struts corresponding to points a and point b in Figure 5.10. For the orientation-y specimen, the angled strut at location A failed first without a noticeable drop in load. A significant drop in load was observed when vertical struts at location B failed. A similar behaviour occurred for orientation-z specimens. Despite the significant surface roughness observed from the images of X-ray computed tomography which could result in variation of strength along the strut, the failure location of each strut was found to be almost consistent. Most failures occurred at the location near to the joint caused by the influence of strut bending and local stress concentration, as shown in Figure 5.15 and 5.16.

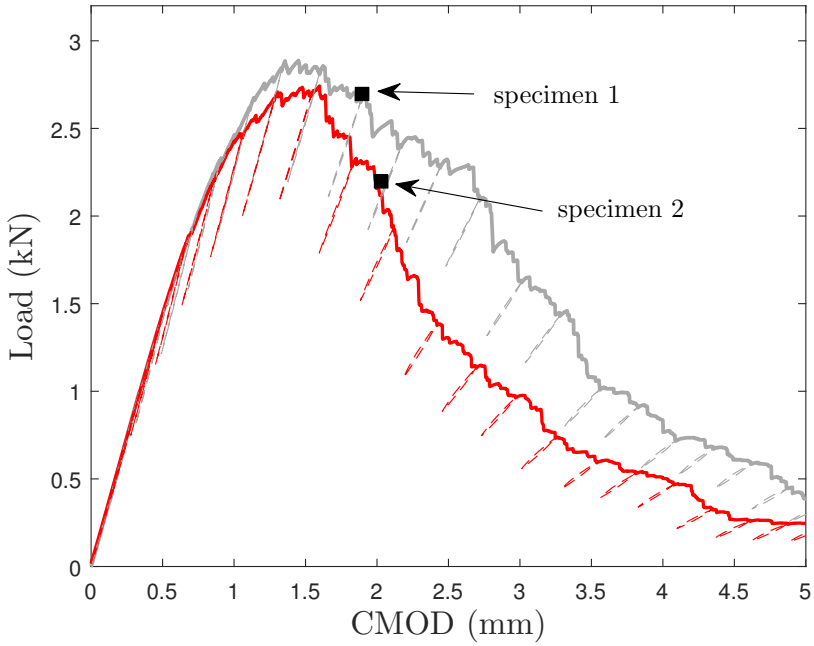

Figure 5.8: Load-displacement response of orientation-y specimen

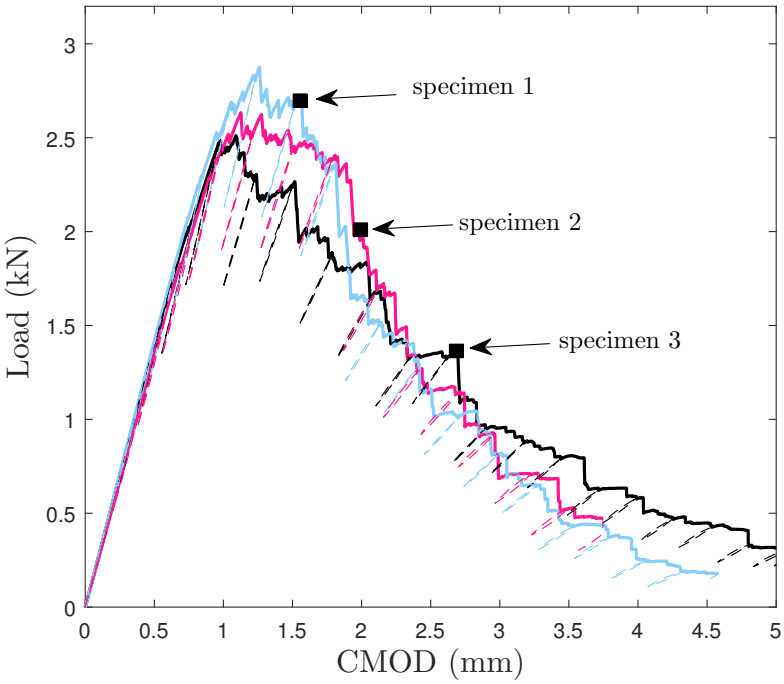

Figure 5.9: Load-displacement response of orientation-z specimen

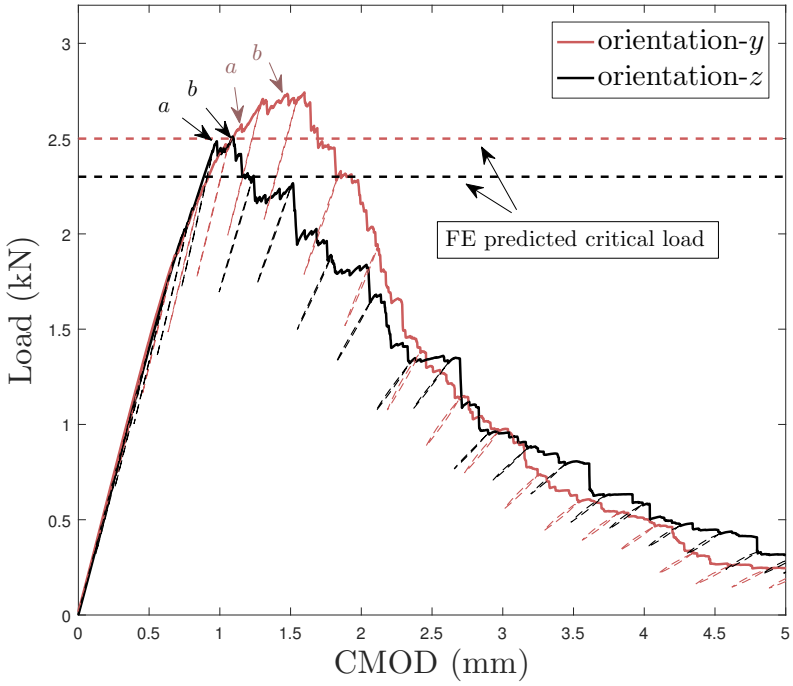

Figure 5.10: Load-displacement response of lattice specimens for two orientations: the results are compared between specimen 2 from orientation-y and specimen 3 from orientation-z

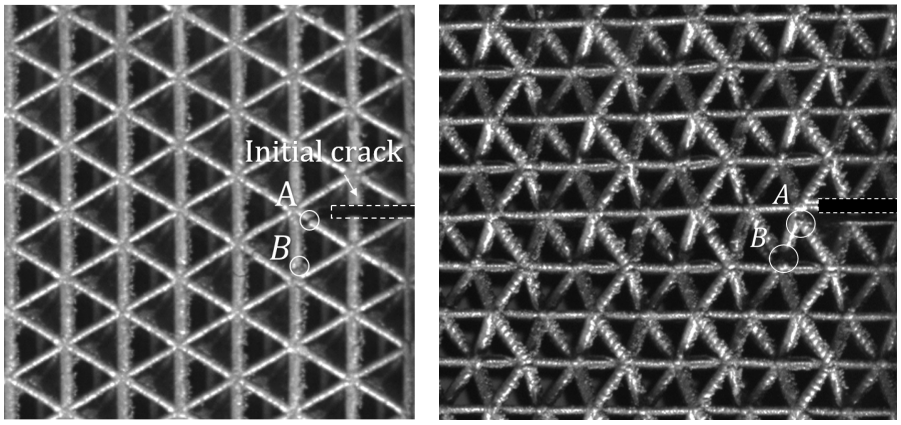

(a) (b)

Figure 5.11: Details of crack growth (a)orientation-y and (b)orientation-z

Repeatable crack paths were observed for each specimen, as shown in Figure 5.12. The crack of orientation-y specimens deviated after initiation and the entire crack plane was rotated by 30° about the Z-axis. The crack path for orientation-z specimens was almost horizontal.

The compliance of each specimen was calculated using the slope of each unloading during crack extension (the dashed lines shown in Figure 5.8 and 5.9). The effective crack length, a/W, can be calculated from the compliance using the ASTM E399:

$$\frac{a}{W} = 1.000 - 4.500U + 13.157U^2 - 172.551U^3 + 879.944U^4 - 1514.6711U^5 \tag{5.3}$$

and:

$$U = \frac{1}{1 + \sqrt{(\frac{EBV_m}{P})}} \tag{5.4}$$

where V_m is the crack mouth opening displacement, P the applied force, B is the specimen thickness and E is the equivalent Young's modulus of the lattice which was calculated based on the measured relative density, $\overline{\rho}$, using the expression given in [30]. The effective crack length matched adequately with visual observations for orientation-z specimens. For the orientation-y specimens, the observed crack length was found to be significantly longer than the effective crack length. When the crack significantly deviated from the horizontal plane, the compliance method was inappropriate for the prediction of the crack length due to the assumption made in the ASTM standard. Figure 5.13 shows fracture resistance, K_R, with increasing normalised effective crack length. The fracture resistance is calculated as:

$$K_R = \frac{P_m}{B\sqrt{W}} f(\frac{a}{W}) \tag{5.5}$$

with:

$$f(\frac{a}{W}) = \frac{(2 + \frac{a}{W})[0.886 + 4.64(\frac{a}{W})^2 - 13.32(\frac{a}{W})^3 - 5.6(\frac{a}{W})^4]}{(1 - \frac{a}{W})^{3/2}} \tag{5.6}$$

where P_m is the maximum applied load in each load cycle. The fracture resistance for crack onset was found to be similar for the two orientations of specimen. An increase in K_R with crack growth was also observed for both orientations, as shown in Figure 5.13.

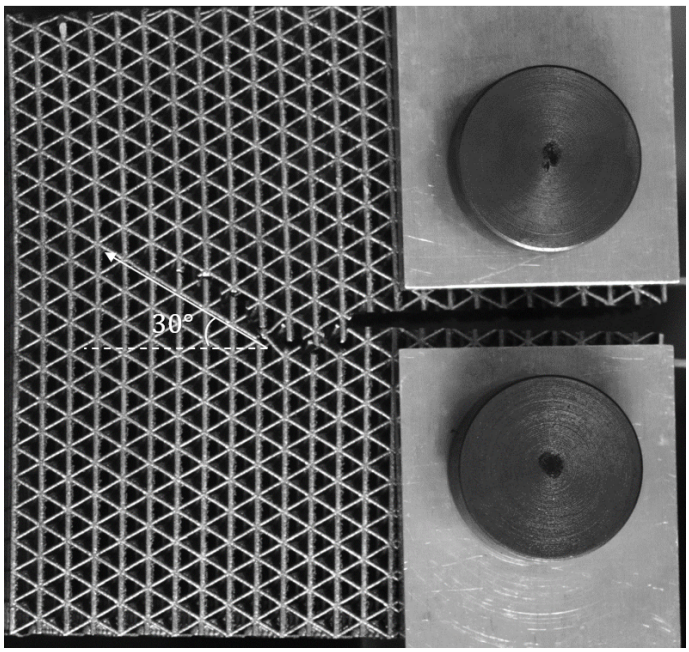

(a)

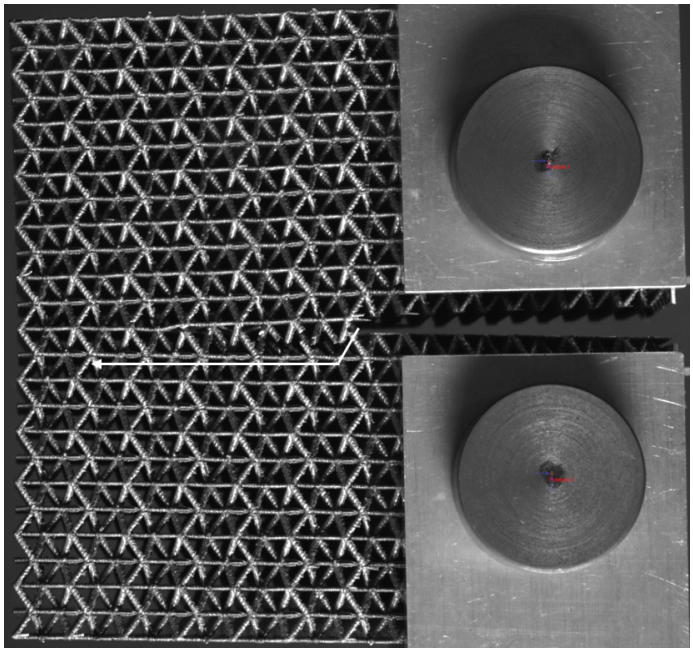

(b)

Figure 5.12: Crack path observed for (a) orientation-y and (b) orientation-z

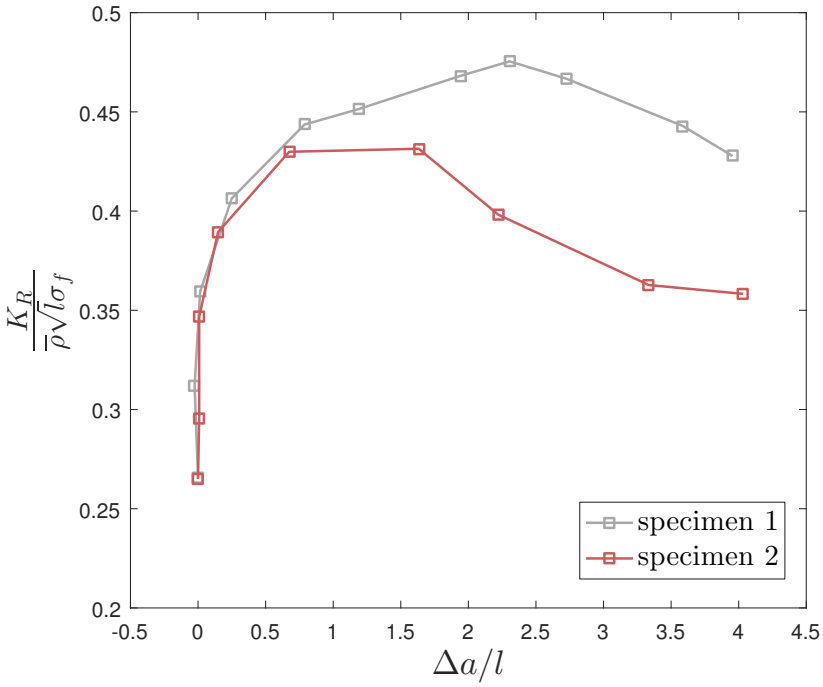

(a)

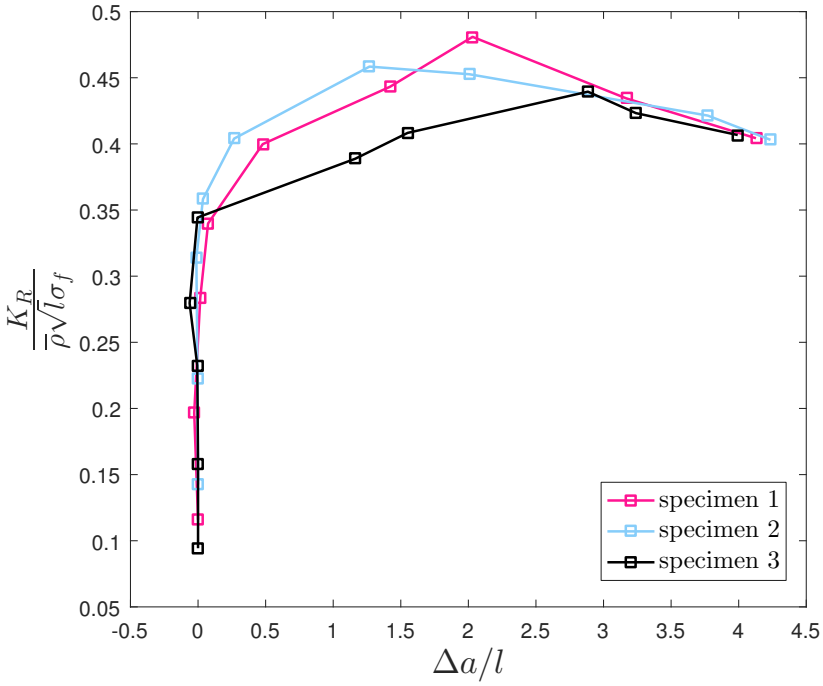

(b)

Figure 5.13: Fracture resistance,K_R, of lattices with (a)orientation-y and (b)orientation-z

5.3.1 FE evaluation

FE analysis was performed using Abaqus 6.14 to predict fracture properties of the lattice. Each strut was modelled using 5 Euler-Bernoulli beam elements (Abaqus element type B33), which was found to be sufficient to achieve a converged solution. Models created for both orientation-y and orientation-z specimens contained approximately 270, 000 nodes and 150, 000 elements. The material behaviour was described by the Ramberg-Osgood relationship:

$$\varepsilon = \frac{\sigma}{E} + 0.002\frac{\sigma}{E}(\frac{\sigma}{\sigma_y})^{n-1} \tag{5.7}$$

The Young's modulus $E = 63$ GPa. The yield strength, σ_y, and hardening coefficient, n, are chosen to be 245 MPa and 20 to approximate the stress-strain curve measured from the tensile test shown in the Figure 5.6. The cell dimensions were defined based on the results of the X-ray computed tomography presented in Section 5.2.3. The significance of build orientation on the mechanical properties have been investigated previously [67]. However, strut properties assumed to be identical in this study for the ease of modelling. The motion of nodes around each pin hole was firstly coupled to a controlling point defined at the hole center. A fixed displacement was then applied at the controlling point to replicate the experiment arrangement.

The failure condition used in this study depends on the magnitude of axial stress: the element is considered to have failed when the maximum axial stress across the element section reaches the tensile strength measured in the tensile test described in Section 3.4. This failure condition was chosen due to the relatively brittle behaviour exhibited by the aluminium alloy. The critical load on the model was evaluated when the failure condition was met at the most heavily loaded strut. It was found the strut at the crack tip was subjected to both tensile and bending stresses. A significant bending stress was found in the orientation-z models due to the large angle between the strut and the loading directions, which causes the lower critical load compared to that of the orientation-y model. The FE predicted critical load is plotted in Figure 5.10 and compared to the experimental measurements with good agreement.

The failed elements were then removed from the model, and the same boundary conditions applied to predict the locations of the next failed elements and the corresponding critical loads. In this way, the crack paths for orientation-y and orientation-z specimens were predicted, as shown in Figure 5.14. There is close agreement with the experiment results shown in Figure 5.12.

Figure 5.15 and 5.16 compare the FE predicted crack path with the experimental observation. The labels in Figure 5.14(a) and (b) indicate the first and second location of element failure in the models. The critical loads were found to increase by 3% after struts failed at the first location for the orientation-y model and 7% for orientation-z model. This was similar to the experiment observations shown in Figure 5.10. In the orientation-y model, the angled struts failed first and the peak load was not reached until the vertical struts at the second location reached their maximum loading capacity. Hence, the peak load is controlled mainly by the strength of vertical struts ahead of the crack front.

For the orientation-z model, there are no struts parallel to the loading direction. However, it was found that the maximum axial stress in the model reduces as failed elements are removed in front of the initial crack front. This indicates that a stronger tip configuration is formed after crack initiation and thus a higher load is required to re-initiate the crack.

The stress intensity at initiation, K_I , was calculated by substituting the predicted initial critical load into Eqn.5.5, and the results were shown in Table 5.2. It was found that a very similar result was calculated for both lattice orientations.

	orientation-y	orientation-z
Measured results	0.35	0.34
	0.36	0.35
		0.36
FE prediction	0.34	0.32

Table 5.2: Comparison of normalised stress intensity, $\frac{K_I}{\bar{\rho}\sigma_f\sqrt{l}}$, at crack initiation between experimental measurements and FE predictions

A set of FE analyses were performed on 5 different sized models with W ranging from $8.5l$ to $42l$, as shown in Figure 5.17, to demonstrate the effect of specimen size on the stress intensity at failure. The critical load and K_I for crack initiation was evaluated for each model. Figure 5.18 plots the normalised stress intensity, K_I, at failure against normalised model size. It was found that K_I reduces with increasing model size for both lattice orientations. Also, the two sets of results were asymptotic to almost the same value with increasing model size. The orientation-y model is more sensitive to the change of specimen size than the orientation-z model.

The largest model was created with $W = 41.5l$, which contained about 2.5 million nodes and 1.4 million elements. About 29 gigabytes of memory was required for the analysis. No attempt was made to analyse a larger model. However, a previous study on two-dimensional triangular lattices suggested that a lattice model with $a = 16l$ is large enough to provide an ad-

equate prediction of the fracture toughness. The stress intensity at fracture for the lattice model with $W = 42l$ shown in Figure 5.18 was therefore taken to be equal to the fracture toughness, K_{IC}. The results also indicate that for the specimen size used in the experiment ($W = 17l$), the measured K_I at initiation is approximately 10% higher than the fracture toughness, K_{IC}.

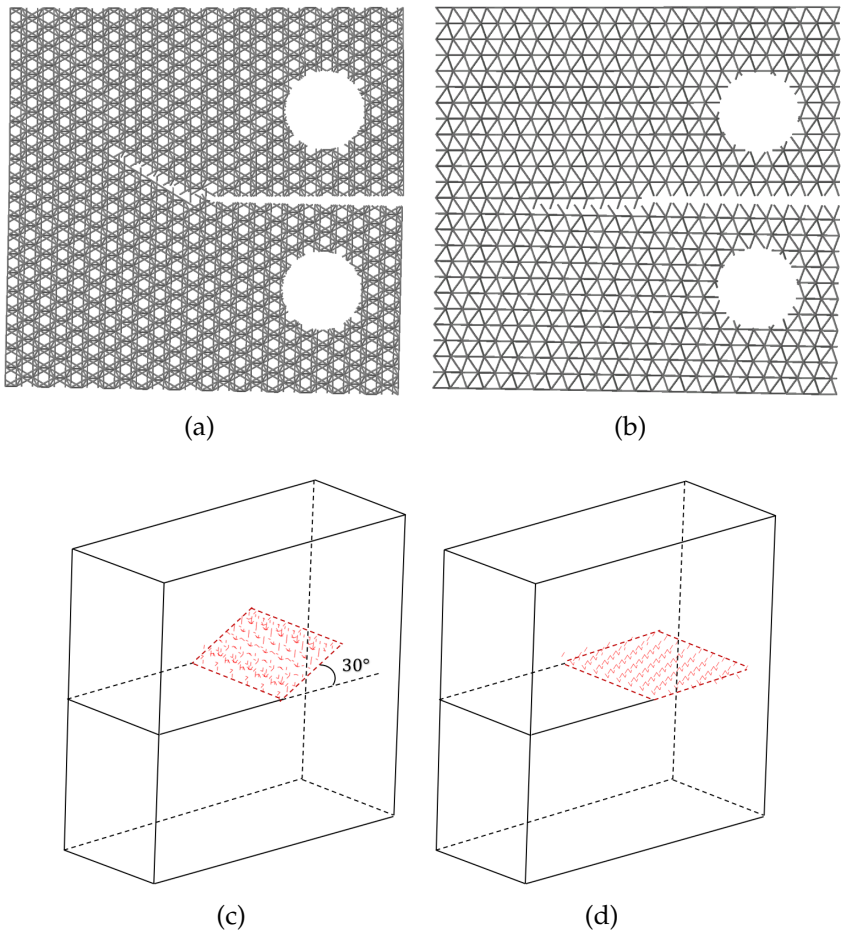

Figure 5.14: Crack path predicted from FE analysis: (a)for orientation-y and (b) for orientation-z show a side view of the models after failed elements have been removed; (c)for orientation-y and (d)for orientation-z show the elements that have failed in a perspective view.

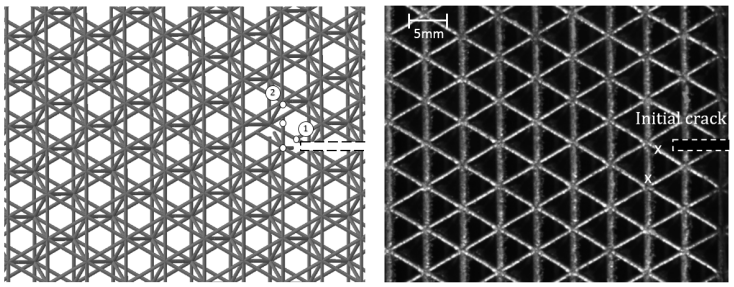

(a) CMOD=1.5mm

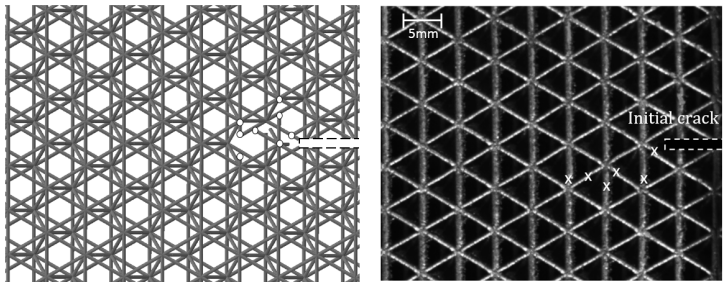

(b) CMOD=2.0mm

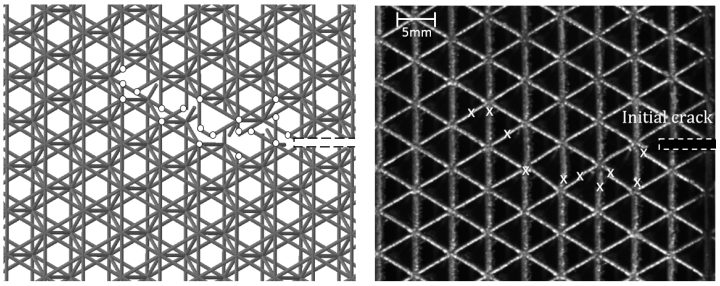

(c) CMOD=2.3mm

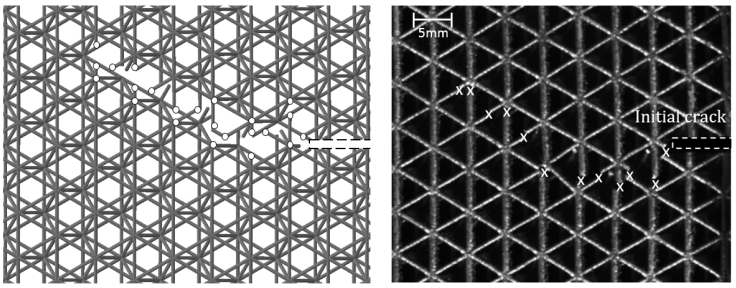

(d) CMOD=2.7mm

Figure 5.15: Details of crack growth of orientation-*y* specimen

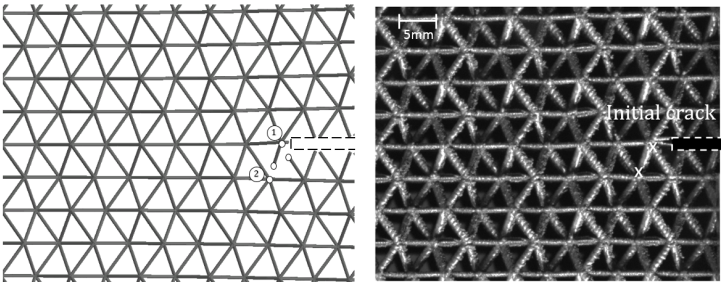

(a) CMOD=1.4mm

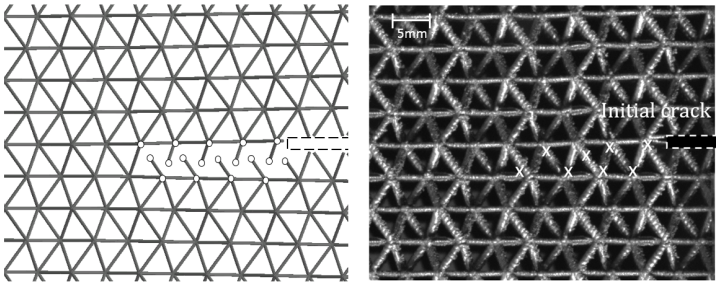

(b) CMOD=2.0mm

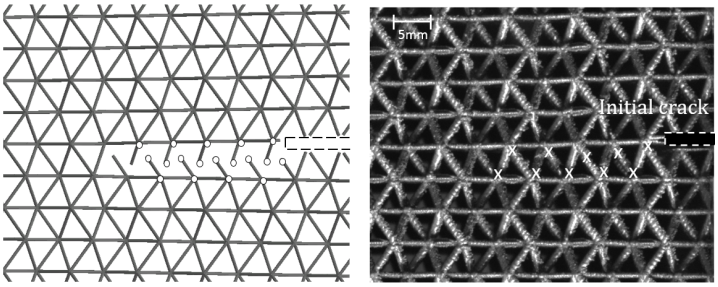

(c) CMOD=2.5mm

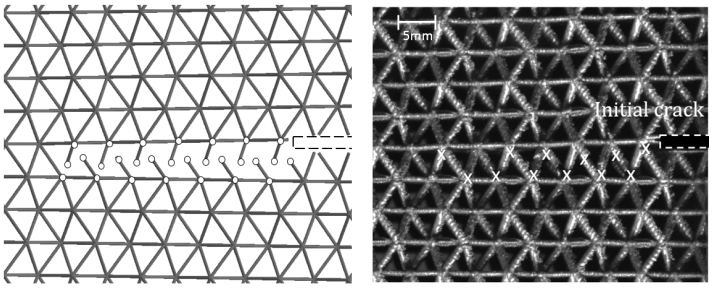

(d) CMOD=2.8mm

Figure 5.16: Details of crack growth of orientation-z specimen

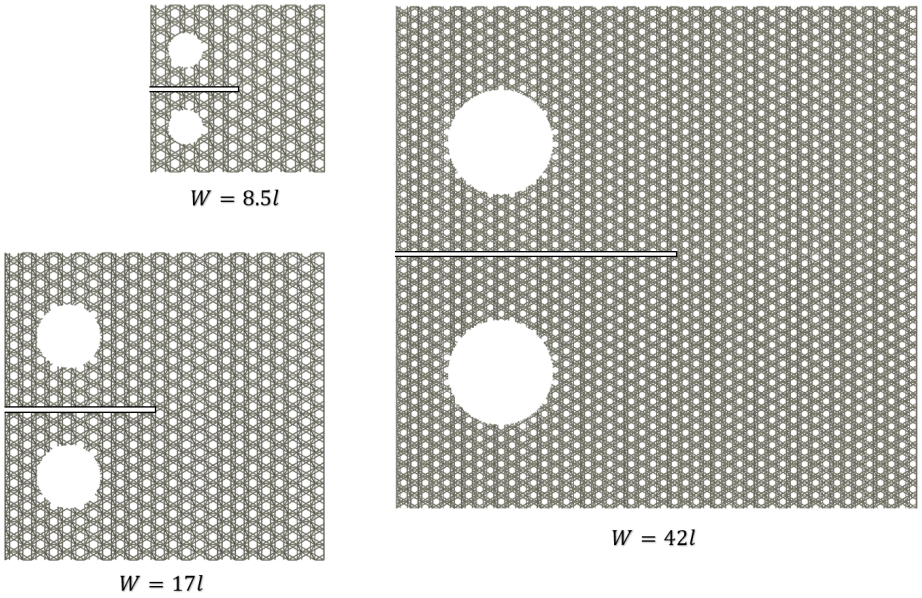

Figure 5.17: Lattice models created in different sizes

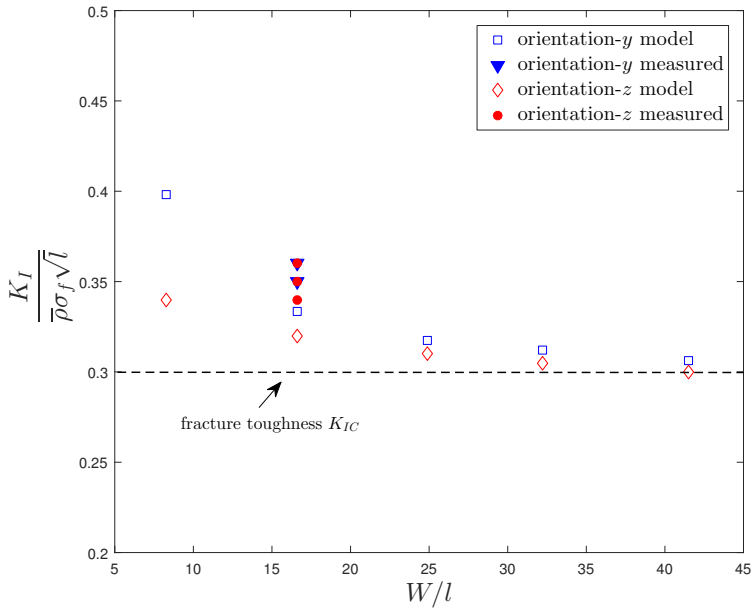

Figure 5.18: Effect of specimen size on toughness measurement

5.3.2 Fracture toughness of other orientations

The experiment results presented in this study suggests that the orientation-y and orientation-z lattices exhibit almost identical fracture toughness,K_{IC}. Here, a set of numerical analysis is performed to evaluate the K_{IC} of other lattice orientations which are referred to as orientation-x and orientation-FCC shown in Figure 5.19. The orientation-FCC is a face-centred cubic configuration, and the loading is applied along the [1 0 0] direction according to the coordinate system defined in Figure 5.1.

The material properties and element types adopted in this simulation are identical to the model described in the Section 5.3.1. Based on size sensitivity analysis given by the Figure 5.18, the models were created with $W = 42l$ in order to achieve the asymptotic toughness value. Table 5.3 compared the evaluated fracture toughness for each lattice orientation. It was found the toughness of the orientation-x and orientation-FCC were very similar compared to that of the orientation-y and orientation-z models. A small discrepancy between the evaluated toughness was associated with the different level of strut bending exhibited at the crack tip. The bending stress at crack tip was relatively large in the orientation-FCC model compared to other orientations due to the large angle between the strut and loading directions. This causes a higher axial stress and results in the reduction in its toughness.

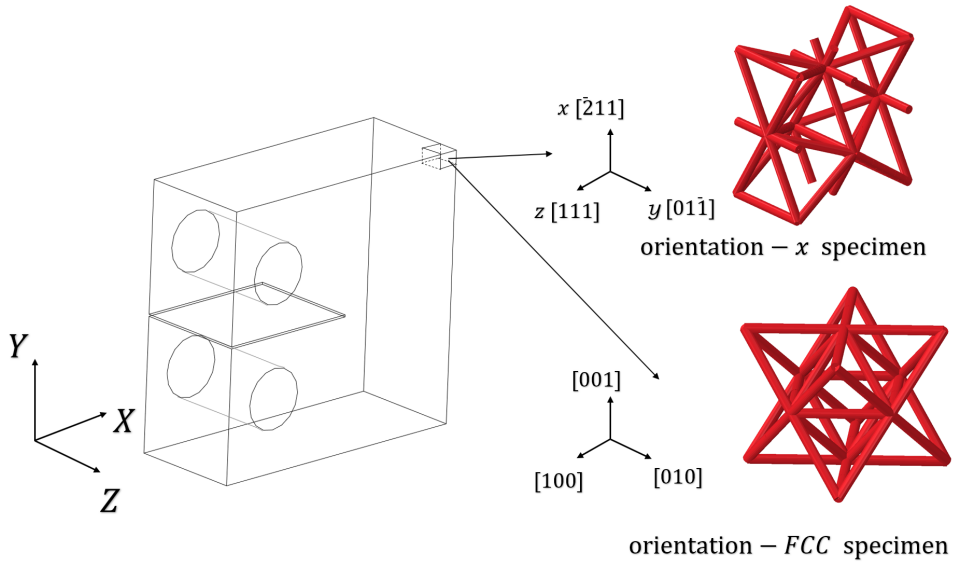

Figure 5.19: Compact tension models for orientation-x and orientation-FCC

	orientation-x	orientation-y	orientation-z	orientation-FCC
$\frac{K_{IC}}{\bar{\rho}\sigma_f\sqrt{l}}$	0.31	0.3	0.3	0.29

Table 5.3: Evaluated fracture toughness of octet-truss lattice for different orientations.

5.4 Influence of specimen geometry

The experimental work was performed using the compact tension (CT) geometry. This section aims to investigate the influence of selection of model geometry on the toughness measurement. The toughness was evaluated from 4 geometries using an orientation-y structure: single edge notch tension (SENT), compact tension(CT), single edge notch bending(SENB) and the thumbnail crack model, as shown in Figure 5.20 and 5.21. These geometries include two and three-dimensional cracks and exhibit different level of crack tip constraint, which was quantified by the T-stress. The T-stress represents a lateral axial stress at the crack tip. It is the first non-singular term in the Williams expansion of the stresses near the crack tip in a continuum and thus has an effect only if there is a fracture process zone of finite size. The significance of T-stress in fracture of two-dimensional lattices has been explored by Fleck and Qiu[5], who concluded that T-stress effects are more significant in a lattice compared to conventional materials. The study showed that the stress in the most heavily loaded strut scales linearly with the T-stress, and results in a change of toughness.

Each model geometry was created for five different sizes (relative to the cell size) to establish the asymptotic value of K_I. The strut length and radius were defined as 10mm and 0.5mm. The material properties were assumed to be linear elastic with modulus of 70GPa and failure stress of 140Ma. For the SENT model, a uniformly distributed load was applied on nodes at the top surface while the nodes at the bottom surface was constrained in the loading direction, but allowing displacement in the lateral directions. The crack length of the SENT was chosen to be half of the model width, $a/W = 0.5$. In the CT model, the motion of nodes around the pin holes are coupled to a controlling point located at the centre of each pin hole. Point loads are then applied on the controlling points to simulate conditions of a real experiment. The normalised crack length, a/W, of the CT model was chosen to be 0.38 according to the standard geometry defined by ASTM E399 [85].

The deeply notched SENB model was created with $a/W = 0.5$. The two ends at the bottom surface are constrained in the vertical direction, and a point load was applied at the center of the top surface. The loading conditions applied to the thumbnail model was identical to that in the SENT model, and the crack size was chosen to be $a/W = 0.2$.

The magnitude of T-stress for each model geometry is shown in Table 5.4, where the T-stress was positive for the CT and deeply notched SENB models[104, 105] and negative for the SENT and thumbnail crack models [105, 106].

	SENT $a/W = 0.5$	SENB $a/W = 0.5$	CT $a/W = 0.38$	thumbnail $\varphi = 0$
$T/\overline{\rho}\sigma_f$	-0.012	0.016	0.015	-0.024
$K_I/(\overline{\rho}\sigma_f\sqrt{l})$	0.25	0.26	0.26	0.22

Table 5.4: T-stress and toughness for different cracked geometries.

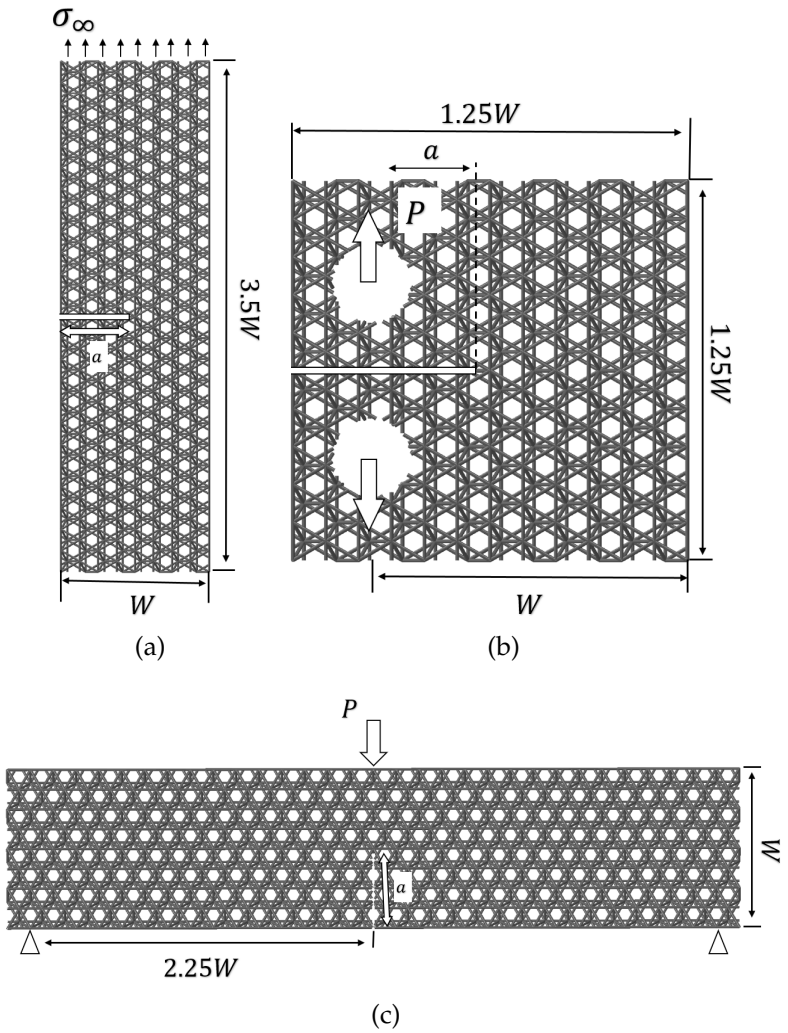

Figure 5.20: Different model geometries created for orientation-y: (a)Single edge notch tension(SENT), (b)Compact tension(CT) model, (c)Single edge notch bending(SENB) model.

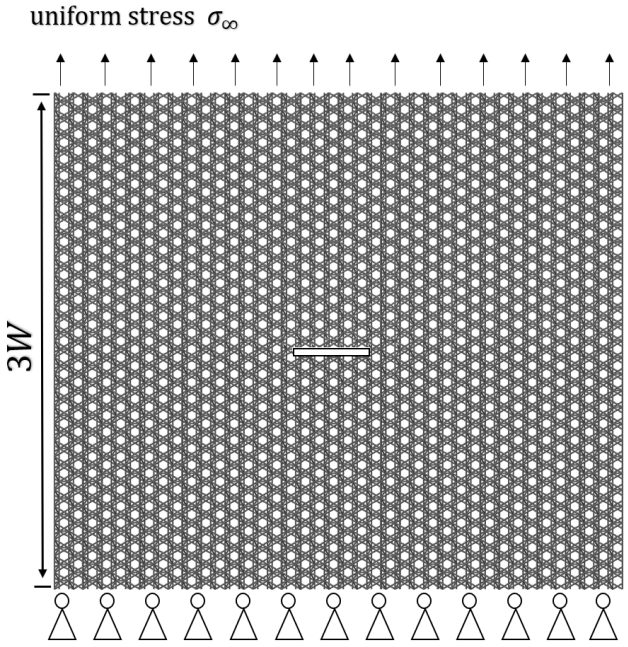

(a)

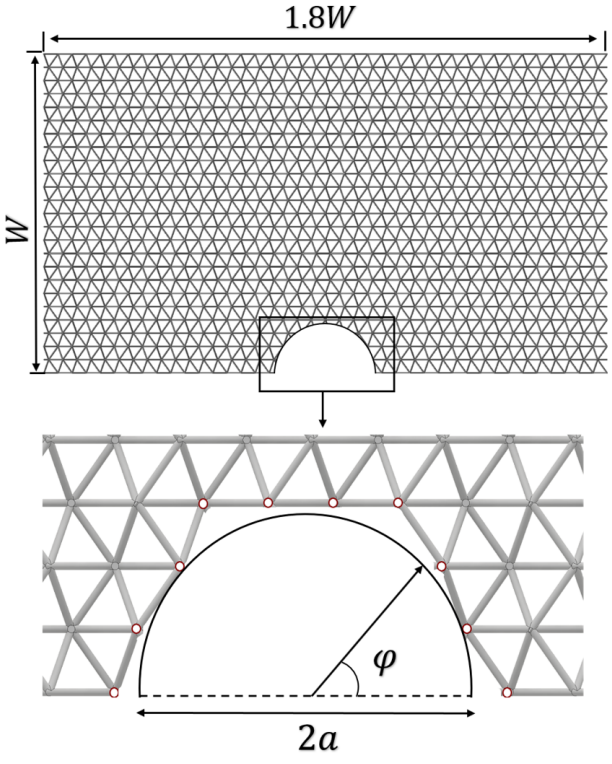

(b)

Figure 5.21: Thumbnail crack model for orientation-y (a) front view of the model (b) top view of the model with details of crack front

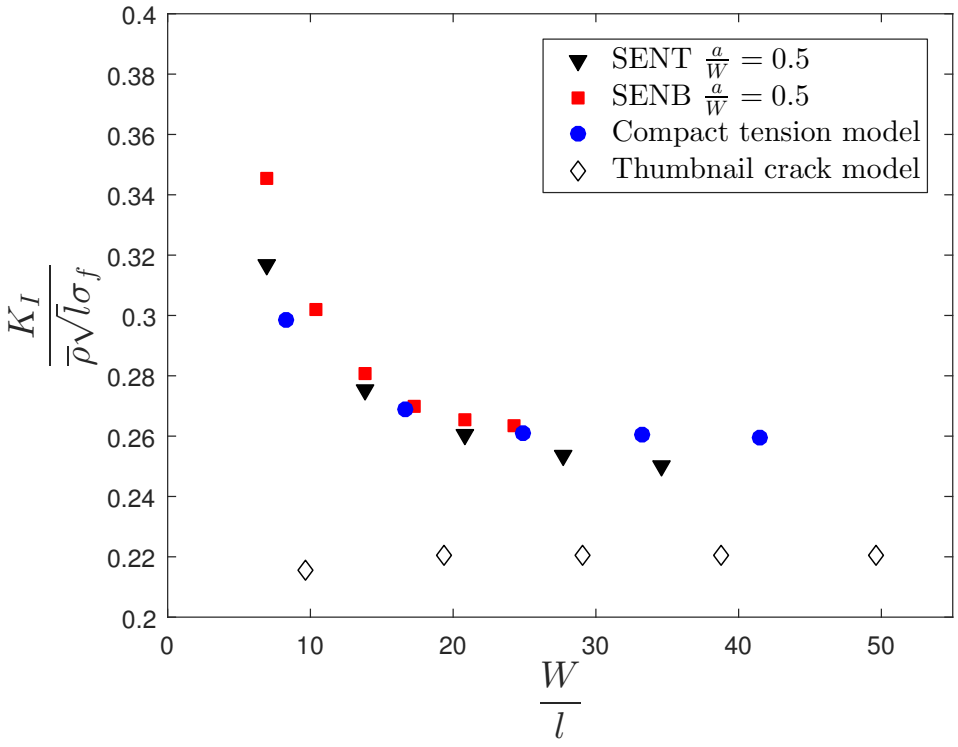

Figure 5.22: Scaled toughness vs model size for different geometries.

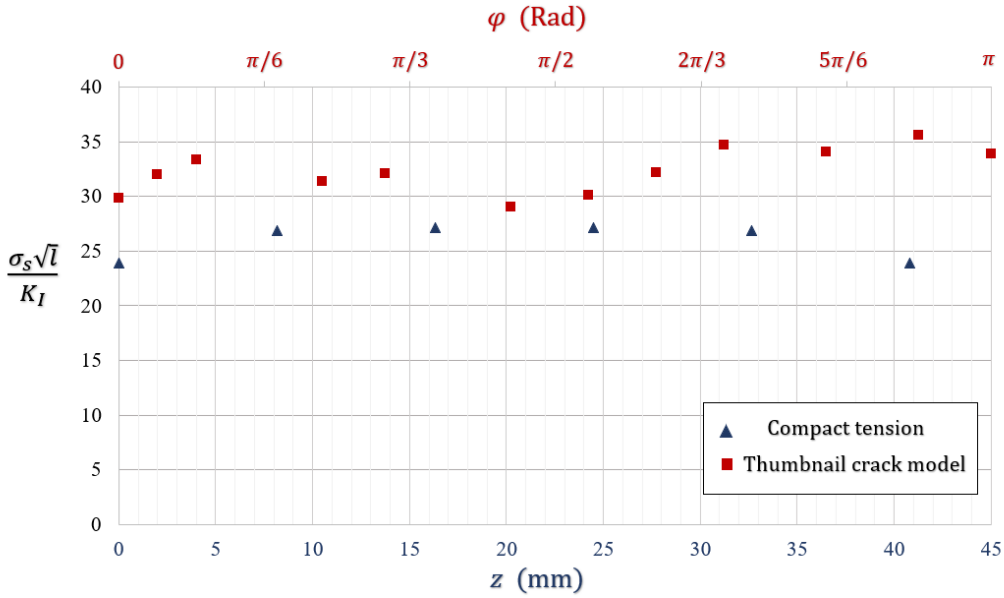

Figure 5.23: Axial stress in the struts along the crack front of thumbnail crack model ($W = 20l$) and compact tension model ($W = 17l$).

The evaluated toughness are shown in Figure 5.22. It was found the toughness measured from the SENT, SENB and CT models asymptote to a very similar value, while the toughness obtained from the thumbnail crack model was approximately 15% lower. This indicates that a significant error will be incurred when using the K_{IC} measured from CT specimen to characterise the fracture strength of the thumbnail crack model. This discrepancy is attributed to the changing condition of strut connectivity along the curved crack front, leading to an increased stress in the struts with low connectivity. Furthermore, the unit cell is not axisymmetric with regards to the vertical axis which results in an asymmetric stress field.

Figure 5.23 shows the comparison of axial stress in the struts along the crack front for compact tension and thumbnail crack model. The stress was normalised by K_I and $\sqrt{l}$, where the K_I was taken at $\varphi = 0$ for the thumbnail crack model. As shown in the Figure 5.23, the axial stress in the struts are almost identical at the crack front for the compact tension model. A slightly increased stresses have seen in the struts at the middle due to the influence of out-of-plane constraint. In contrast, axial stresses in the struts along the curved crack front are highly uneven and asymmetric. The most heavily loaded strut have seen at $\frac{5\pi}{6} < \varphi < \pi$, where the stress is significantly higher than the maximum stress reached in the compact tension model.

It was also noticed that the toughness measured from the deeply notched SENB and CT models are approximately 5% higher then that of the SENT model, due to the influence of a positive T-stress. To demonstrate the effect of T-stress on K_I of the lattice, a modified boundary layer analysis(BLA) has been performed. Due to the large computation effort required for large scale three-dimensional model, a two-dimensional triangular lattice was used; A large circular triangular lattice model was created with $R = 100l$, as shown in Figure 5.24, which has been found to be sufficiently large to achieve converged result [52]. The node displacements and rotations were applied to the outer boundary based on K_I asymptotic field with additional T-stress terms:

$$
\begin{aligned}
u_x(R,\theta) &= K_I \frac{1-v}{E}\sqrt{\frac{R}{2\pi}} cos(\frac{\theta}{2})(3-4v-cos(\theta)) + T\frac{1-v^2}{E} R cos(\theta) \\
u_y(R,\theta) &= K_I \frac{1-v}{E}\sqrt{\frac{R}{2\pi}} sin(\frac{\theta}{2})(3-4v-cos(\theta)) - T\frac{v(1+v))}{E} R sin(\theta) \\
\phi &= \frac{\partial u_x}{\partial y} - \frac{\partial u_y}{\partial x}
\end{aligned}
\tag{5.8}
$$

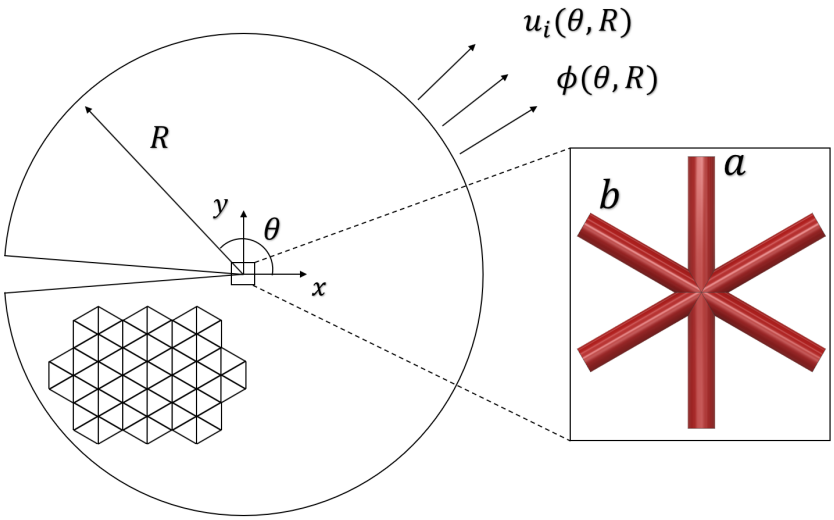

Figure 5.24: Boundary layer analysis of a two-dimensional triangular lattice

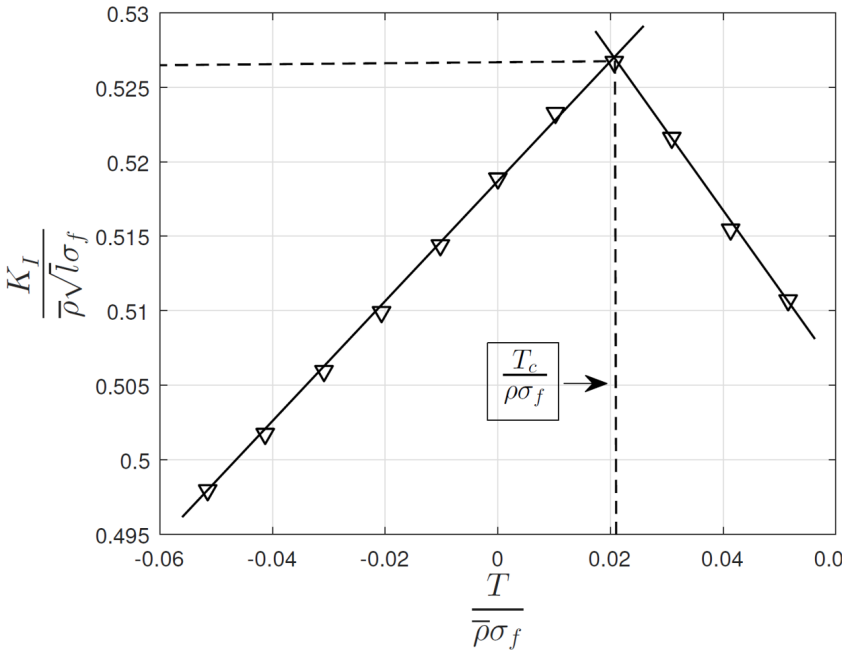

Figure 5.25: Two parameters fracture criterion for two-dimensional triangular lattice structure

The K_I was evaluated for the model subjected to different magnitude of T-stress, and the results were shown in Figure 5.25. It has been found that the location of the most heavily loaded strut switched from strut a to strut b when T-stress increases. When strut a is the most heavily loaded strut, an increase in T-stress results in an increase in load carried by strut b and a reduction in the load carried by strut a, leading to an increased in apparent toughness. When T-stress is higher than the critical value, T_c, shown in Figure5.24, strut b becomes the most heavily loaded strut and an increase in T-stress results in an increase in load carried by the strut, leading to a decrease in apparent toughness. The critical T-stress, T_c , was indicated in Figure 5.25, and the K_I became more sensitive to the change of T-stress for $T > T_c$. A similar phenomenon has also been reported in the work of Fleck and Qiu[5] where the stress in the most heavily loaded strut in a triangular lattice reduces linearly with increasing T-stress.

5.5 Crack growth simulation

This section aims to simulate brittle fracture behaviours of the lattices using the SENT and thumbnail crack models created in orientation-x, -y and -z. The fracture was simulated by reducing the element bending and axial stiffness to zero when the axial stress reached the failure stress, σ_f at an integration point. This was implemented using a user defined field variable(UDFV) subroutine in the Abaqus. Timoshenko beam elements were used and the failure stress, σ_f,was set to 140 MPa.

In the SENT and the thumbnail models a fixed displacement was applied on the top surface, while the bottom surfaces were constrained in the loading direction. Crack paths are shown by highlighting the failed elements in Figure 5.26 and 5.28. More detailed visualisations are given in Figure 5.27. The crack path depends on both the structural orientation and geometry. In the SENT model, the crack paths of orientation-x and orientation-z structures were perpendicular to the loading direction, as shown in Figure 5.26(a) and (c). However, the crack in the orientation-y structure deviated from the original orientation by 30°, shown Figure 5.26(b). This agrees with the experiment observation from the Section 5.2 on compact tension specimen. The performance of the thumbnail crack was also found to be orientation dependent. In the orientation-y and -z structures, the crack paths deviated from the horizontal plane, particularly in orientation-z structure, where the crack path was conical, as shown in Figure 5.28(c). The fracture response curves were plotted for each orientation. There was no significant orientation dependency observed in terms of fracture load in the SENT, shown in Figure 5.29.

In the thumbnail crack model, orientation-z shows a significantly higher fracture resistance compared to the other orientations, because the initial crack propagation is along a macroscopically conical surface, leading to an increasing number of struts at the crack front. The peak nominal stress (load over the net area of the top surface) was achieved after the conical propagation stage gave way to the horizontal fracture surfaces. The peak load of the orientation-z model cannot be adequately characterised using the toughness, K_{IC}, measured from the lattice models with linear crack front such as the CT and SENT models. However, it is still unclear how much these observations are affected by limited model sizes (width and depth). The thumbnail crack model used in the simulation contains about 1.6 million nodes and 1.7 million elements, and a large number of increments are required to ensure the accuracy of the prediction. Thus,the fracture behaviour in a larger thumbnail crack model was not conducted in this work. Open source FE solvers such as ParaFEM may be considered in the future work to reduce computation time.

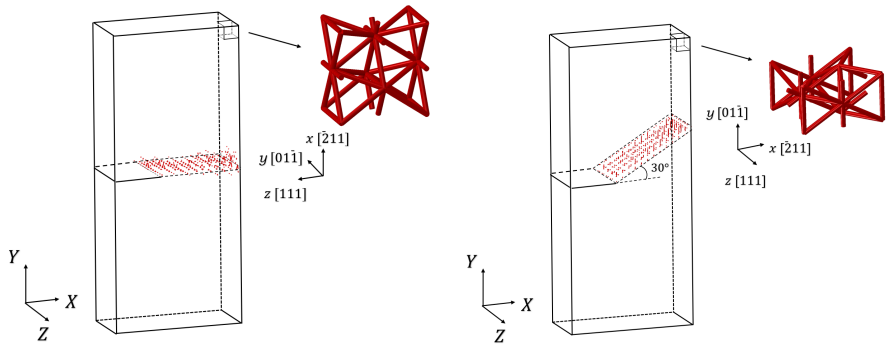

(a) orientation-x (b) orientation-y

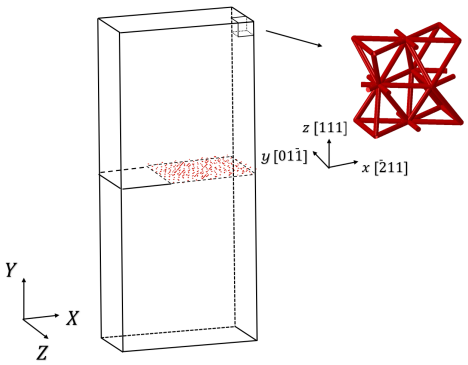

(c) orientation-z

Figure 5.26: The crack paths in the SENT model for three lattice orientations, $W = 13l$ and $a/W = 0.25$.

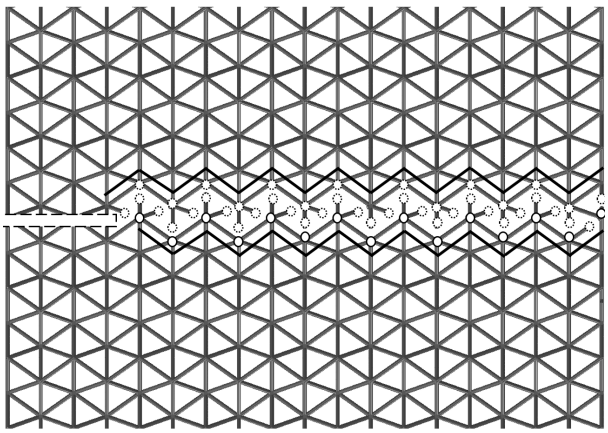

(a) orientation-x

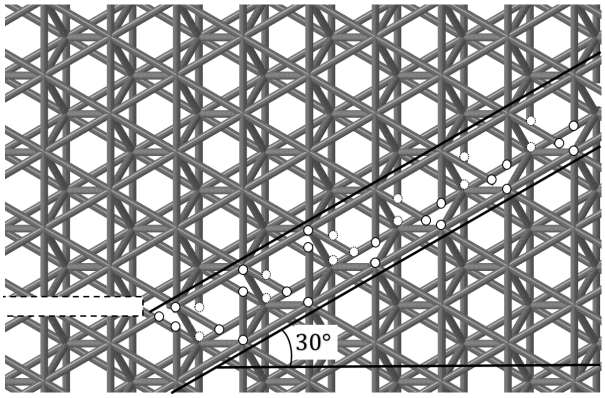

(b) orientation-y

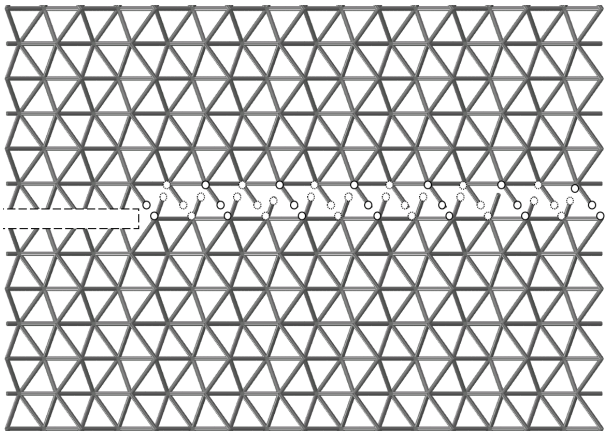

(c) orientation-z

Figure 5.27: The detailed crack paths in the SENT models for the three orientations in $X-Y$ plane.

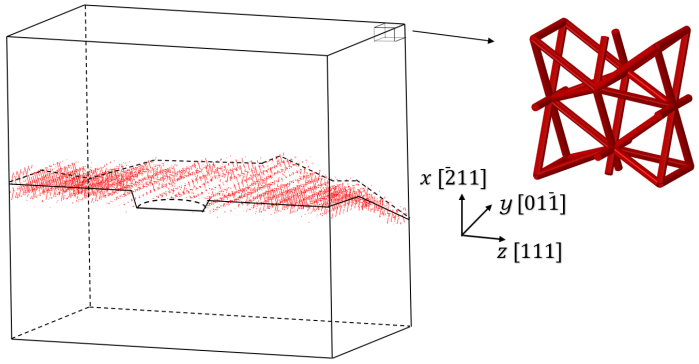

(a) orientation-x

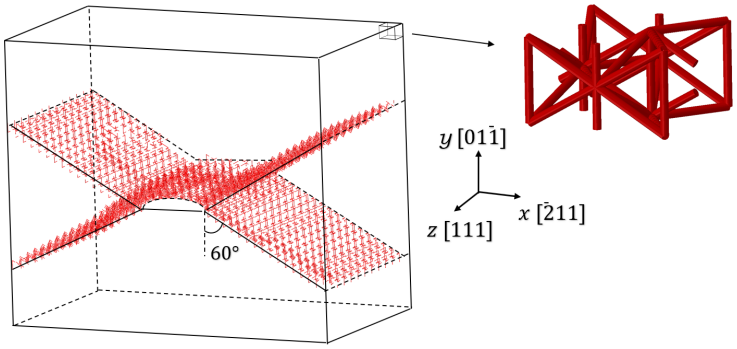

(b) orientation-y

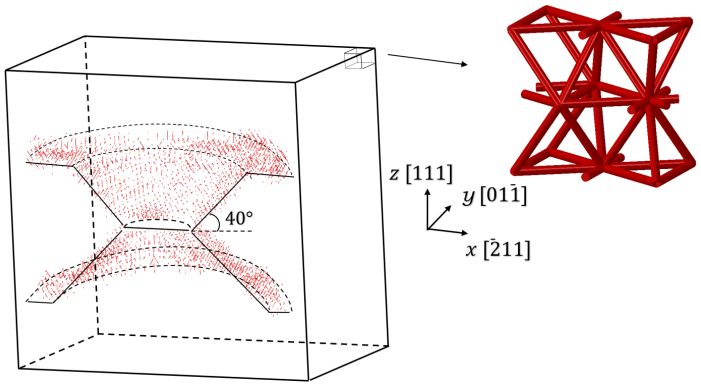

(c) orientation-z

Figure 5.28: The crack paths in the thumbnail crack model for the three lattice orientations, $W = 20l$ and $a = 4l$.

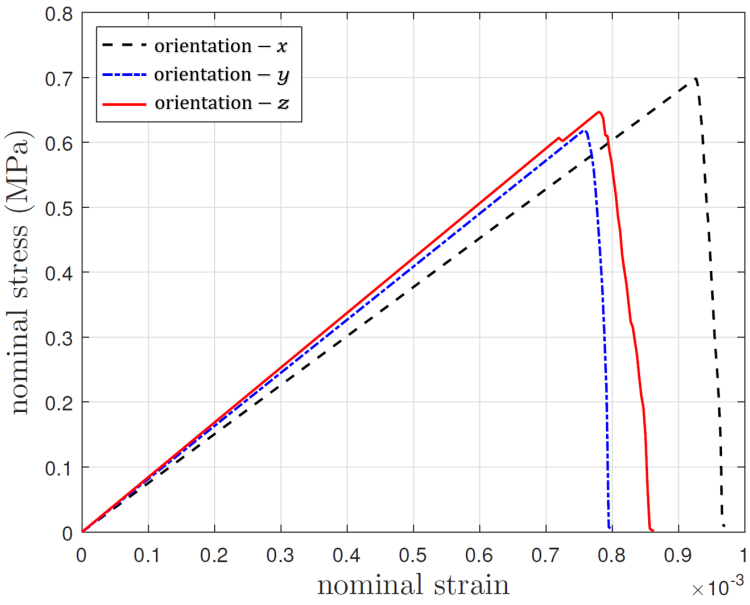

Figure 5.29: The fracture responses of SENT models.

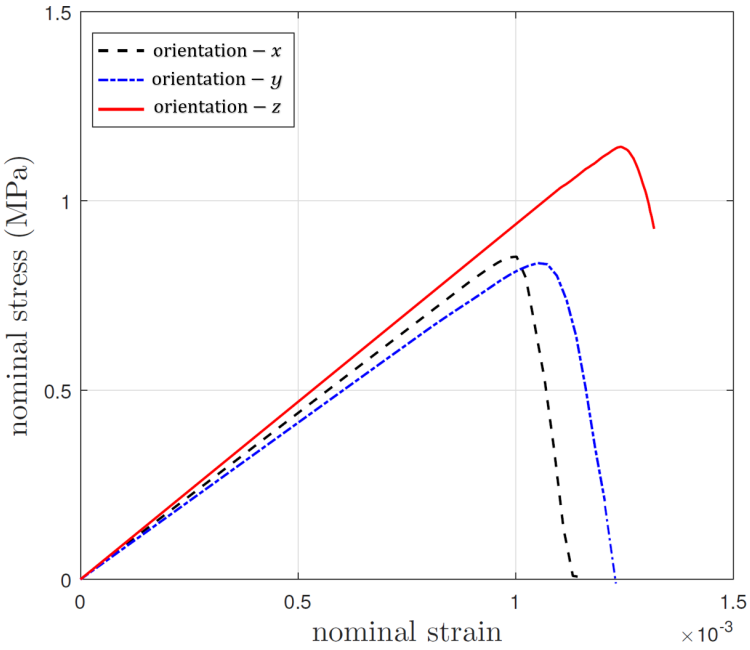

Figure 5.30: The fracture responses of thumbnail crack models.

5.6 Concluding remarks

This chapter investigated the fracture behaviour of the octet-truss lattice. The fracture toughness has been experimentally measured from compact tension specimens fabricated using the selective laser melting (SLM) technique. A similar work has been conducted by M.O'Masta et.al.[4] where the K_{IC} of a orientation-*FCC* structure fabricated using snap-fit method was measured from a three-point bending fracture test. The specimen fabricated by selective laser melting showed a reasonable dimensional accuracy and significantly smaller volume of joints compared to lattices made by snap-fit method. Hence the properties are adequately predicted by the discrete FE models using beam elements.

The experiment results reveals that the change of lattice orientation leads to significant differences in crack paths, while the influence on the toughness is small. The measured toughness is plotted on the material property chart to compare with the property of other categories of materials including the fracture toughness of titanium octet-truss lattice measured by M.O'Masta et.al, as shown in Figure 5.31. A relatively high fracture toughness is measured from the Aluminium octet-truss lattices compared to nature materials and foams at the same density.

The influence of specimen geometry on the lattice toughness was explored. A very similar results were evaluated from from the compact tension(CT), single edge notch bend(SENB) and single edge notch tension(SENT) models. A small discrepancy was noticed between these results which was attributed to the different level of T-stresses exhibited in each model geometry. The boundary layer analysis(BLA) revealed that the maximum axial stress in the strut changes linearly with T-stress.

Furthermore, a sufficiently large T-stress could lead to the switch in location of the most heavily loaded strut. The critical T-stress, T_c, was evaluated, such that for $T < T_c$, the K_I linearly increased with T-stress due to the reduction of strut bending at the crack tip. The location of the maximum stress was reached in a different strut for $T > T_c$, and with further increase in the T-stress resulted in a reduced K_I.

The thumbnail crack model exhibited a significant different fracture behaviour compared to CT and SENB models. This is attributed to the variation of structures along the curved crack front, which generated more complexity compared to the model with linear crack front. The toughness evaluated using the thumbnail crack model was found to be 15% lower than the CT and SENB models. Also a very different crack path was observed from the orientation-z lattice, where the crack path is conical.

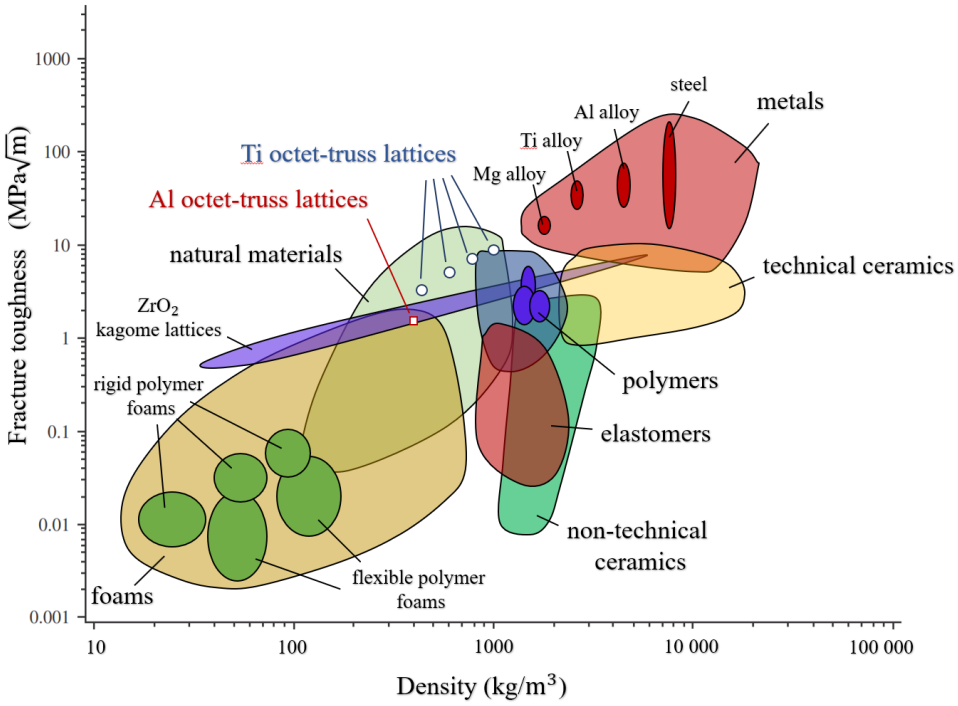

Figure 5.31: Material property chart of the fracture toughness,K_{IC}, against density. The property values were sourced from [1], and the fracture toughness of Ti octet-truss lattice was based on the measurement from M.O'Masta et.al.[4].

Chapter 6

Conclusions

6.1 Overall conclusions

The central thesis of this dissertation is to present experimental study to explore mechanical properties of two and three-dimensional lattices. The property of lattices does not solely depend on unit cell geometry, but is also on the number of cells included in models, and crucially on the lattice orientation. The experimental outcomes produced from this dissertation also demonstrated the reliability of proposed numerical and analytical models.

Chapter 2 reviewed current researches associated with the mechanical behaviours of periodic lattices. In the analytical and numerical analysis, the lattices have been modelled as interconnected beams, and their mechanical properties were therefore derived according to the beam theory. The same methodology was applied to investigate fracture behaviours of lattices including fracture toughness, crack path and crack-tip field. However, not many existing literatures characterised the properties of lattices fabricated by modern manufacturing techniques and provided guidance regarding how reliable the numerical predictions are.

Following on from this, Chapter 3 presented a comprehensive study to illustrate mechanical properties of two-dimensional triangular lattices. The influence of lattice orientation on the mechanical properties was considered in the numerical analysis. The results suggested that the lattice modulus was isotropic but the yield strength was strongly dependent on the orientation. It was noticed that the 30° orientation exhibited the highest yield strength suggesting this lattice orientation was the most weight efficient. This conclusion has been further approved by the unaxial tensile tests. The specimens produced from water-cutting technique showed a reasonable dimensional accuracy and the measured properties agreed well with that predicted by discrete FE models using beam elements. This agreement significantly increases the confidence of using this numerical method for future studies.

The discrete beam model has been applied to explore fracture toughness of the triangular lattices. It has been illustrated in Chapter 3 that the dependency of the fracture toughness upon the lattice orientation was affected by the ductility of the strut material. For brittle triangular lattices, the change in lattice orientation only produced a small influence on fracture toughness, while the evaluated fracture toughness varied by 40% with the change of lattice orientation when the strut material exhibited significant plasticity. The elastic modulus and yield strength of three-dimensional octet-truss lattice were described in Chapter 4. The results once again highlight the significance of the lattice orientation effect. It was noticed that the modulus can be varied by 20% while the yield strength can be doubled when the lattice orientation was changed. Furthermore, the effect of finite cell number has been seen that an increased modulus and yield strength were evaluated from the model with reduced number of cells.

Chapter 5 started with presenting an experimental study to demonstrate the fracture behaviour of the octet-truss lattices. Despite the existence of imperfections such as surface roughness and porosity observed on the lattice specimens fabricated by selective laser melting process, the fracture toughness and crack paths can be well predicted by discrete FE models. The octet-truss lattices comprised of brittle struts exhibited almost isotropic fracture toughness. This phenomenon agreed well with the conclusion drawn from Chapter 3 on two-dimensional triangular lattices. Further, a distinct initial rising part in K_R was noticed. A similar phenomenon has been commonly seen in metal foams due to the effect of crack bridging [107]. However, in the octet-truss lattices, the increase in fracture resistance was attributed to the change of strut arrangement ahead of crack tip. Consequently, a stronger structural configuration was formed with more evenly distributed load across the crack front, leading to the reduction of stress in the most heavily loaded strut. This toughening mechanism can be potentially adopted in the future topology design for achieving a high toughness.

Finally, the numerical analysis illustrated that the identical toughness can be evaluated from different model geometries. The results suggested that the fracture strength of the lattices can be adequately predicted using the linear elastic fracture mechanics(LEFM) based on the toughness value measured from any standard fracture specimen. However, it was noted that the toughness evaluated from models with a linear crack front overestimated the fracture strength of a thumbnail crack model, where a highly uneven stress distribution has been seen along the curved crack front due to the changing condition of connectivity. An increased stress was noticed at the strut where its local connectivity was low, leading to a reduction in fracture resistance. This set of numerical results further enhanced confidence of applying LEFM on lattice models with linear crack front, but raised concern of implementing the same methodology to predict fracture strength when the crack geometry was changed.

6.2 Recommendations for future work

1. The present work reveals that the LEFM is inadequate to be used for predicting the fracture strength for the thumbnail crack models. Future work could perform an experimental study to validate this phenomenon and explore a methodology to assess the influence of the complexity of crack tip structure ahead of a curved crack front.

2. The fracture performances of two-dimensional triangular lattice is explored in this study. It is noticed that some struts are under compression when a tensile load is applied to the lattice. Hence, a numerical analysis could carry out to explore the condition that the strut buckling occur prior to the fracture of the tensile loaded struts and investigate how the macroscopic fracture performances could be affected by the local buckling behaviour.

3. The crack path is found to be orientation dependent in this study. It deviates from its initial direction in some lattice orientations, while grows horizontally in others. A structure could be designed by comprising of different orientated cells to achieve a desired crack path, and improve fracture performances.

4. In this study, fracture behaviour is investigated using models with a single crack. The interaction of multiple cracks is not clear. The future work could carry on a numerical study to explore the influence of parallel cracks and illustrate how stress at the most heavily loaded strut could be shielded by the surrounding cracks.

Bibliography

[1] N. A. Fleck, V. S. Deshpande, and M. F. Ashby. Micro-architectured materials: past, present and future. *Proceedings of the Royal Society A: Mathematical, Physical and Engineering Sciences*, 466, 2010.

[2] Michael F.Ashby Lorna J. Gibson. *Cellular solids: Structure and properties*. Cambridge University Press, second edition, 1997.

[3] N.A.Fleck H.C.Tankasala, V.S.Deshpande. Crack-tip Fields and Toughness of Two-Dimensional Elasto-plastic Lattices. *Journal of Applied Mechanics*, 82:1–10, 2015.

[4] M.R. O'Masta, L. Dong, L. St-Pierre, H.N.G. Wadley, and V.S. Deshpande. The fracture toughness of octet-truss lattices . *Journal of the Mechanics and Physics of Solids*, 98:271 – 289, 2017.

[5] Norman A. Fleck and XinMing Qiu. The damage tolerance of elastic-brittle, two-dimensional isotropic lattices. *Journal of the Mechanics and Physics of Solids*, 55(3):562–588, 2007.

[6] I. Quintana Alonso and N.A. Fleck. Damage tolerance of an elastic-brittle diamond-celled honeycomb. *Scripta Materialia*, 56, 2007.

[7] Xiaodong Cui, Zhenyu Xue, Yongmao Pei, and Daining Fang. Preliminary study on ductile fracture of imperfect lattice material. *International Journal of Solids and Structures*, 48(25-26):3453–3461, 2011.

[8] H. YANO, A. HIROSE, and S. INABA. High-strength wood-based materials. *Journal of Materials Science Letters*, 16:1906–1909, 1997.

[9] Seema Jain, Rakesh Kumar, and U. C. Jindal. Mechanical behaviour of bamboo and bamboo composite. *Journal of Materials Science*, 27:4598–4604, 1992.

[10] T. Gutu. A study on the mechanical strength properties of bamboo to enhance its diversification on its utilization. *International Journal of Innovative Technology and Exploring Engineering*, 2, 2013.

[11] T. Gutu. Carbonization of wood for advanced materials applications. *Carbon*, 35:259 – 266, 1997.

[12] Sajad Arabnejad, R Burnett Johnston, Jenny Ann, Baljinder Singh, Michael Tanzer, and Damiano Pasini. Acta Biomaterialia High-strength porous biomaterials for bone replacement : A strategy to assess the interplay between cell morphology , mechanical properties , bone ingrowth and manufacturing constraints. *Acta Biomaterialia*, 30:345–356, 2016.

[13] Peter Heinl, Lenka Mu, Robert F Singer, Frank A Mu, and Carolin Ko. Cellular Ti – 6Al – 4V structures with interconnected macro porosity for bone implants fabricated by selective electron beam melting. *Acta Biomaterialia*, 4:1536–1544, 2008.

[14] Ahmed K Noor, Samuel L Venneri, Donald B Paul, and Mark A Hopkins. Structures technology for future aerospace systems. *Computers and Structures*, 74:507–519, 2000.

[15] Kostopoulos V. The buckling response of lattice fuselage structures : Validation of finite element models by using smeared unit cell analytical methodology. *Journal of Aeronautics Aerospace*, 6(1):1–5, 2017.

[16] Nathan Wicks and John W Hutchinson. Optimal truss plates. *International Journal of Solids and Structures*, 38:5165–5183, 2001.

[17] Ed Chen Wai-fah. *Structural Engineering Handbook-Space Frame Structures*. ASME Press, New York, third edition, 2000.

[18] J. Schwerdtfeger, P. Heinl, R. F. Singer, and C. Körner. Auxetic cellular structures through selective electron-beam melting. *physica status solidi (b)*, 247:269–272, 2010.

[19] Xiaoyu Zheng, Howon Lee, Todd H. Weisgraber, Maxim Shusteff, Joshua DeOtte, Eric B. Duoss, Joshua D. Kuntz, Monika M. Biener, Qi Ge, Julie A. Jackson, Sergei O. Kucheyev, Nicholas X. Fang, and Christopher M. Spadaccini. Ultralight, ultrastiff mechanical metamaterials. *Science*, 344(6190):1373–1377, 2014.

[20] Alex Slann, William White, Fabrizio Scarpa, Katarzyna Boba, and Ian Farrow. Cellular plates with auxetic rectangular perforations. *physica status solidi (b)*, 252(7):1533–1539, 2015.

[21] S.K. Maiti, L.J. Gibson, and M.F. Ashby. Deformation and energy absorption diagrams for cellular solids. *Acta Metallurgica*, 32:1963 – 1975, 1984.

[22] V. S. Deshpande, M. F. Ashby, and N. A. Fleck. Foam topology: Bending versus stretching dominated architectures. *Acta Materialia*, 49(6):1035–1040, 2001.

[23] Zuhal Ozdemir, Everth Hernandez-Nava, Andrew Tyas, James A. Warren, Stephen D. Fay, Russell Goodall, Iain Todd, and Harm Askes. Energy absorption in lattice structures in dynamics: Experiments. *International Journal of Impact Engineering*, 89, 2016.

[24] L Kh Rysaeva, A I Klyavlina, F Kh Galiachmetov, J A Baimova, D S Lisovenko, and V A Gorodtsov. Deformation behaviour of re-entrant carbon honeycomb structures. *Conference Series: Materials Science and Engineering*, 447, 2018.

[25] O. A. Bauchau and J. I. Craig. Euler-bernoulli beam theory. *Springer Netherlands*, 19:173–221, 2009.

[26] Digby D. Symons and Norman A. Fleck. The Imperfection Sensitivity of Isotropic Two-Dimensional Elastic Lattices. *Journal of Applied Mechanics*, 75(5):051011, 2008.

[27] Gérald Gurtner and Marc Durand. Stiffest elastic networks. *Proceedings of the Royal Society A: Mathematical, Physical and Engineering Sciences*, 470, 2014.

[28] M. Beran and J. Molyneux. Use of classical variational principles to determine bounds for the effective bulk modulus in heterogeneous media. *Quart. Appl. Math.*, 24, 1966.

[29] Z. Hashin and S. Shtrikman. A variational approach to the theory of the elastic behaviour of multiphase materials. *Journal of the Mechanics and Physics of Solids*, 11, 1963.

[30] V.S. Deshpande, N.A. Fleck, and M.F. Ashby. Effective properties of the octet-truss lattice material. *Journal of the Mechanics and Physics of Solids*, 49:7181 – 7196, 2001.

[31] Thomas Tancogne-Dejean and Dirk Mohr. Elastically-isotropic truss lattice materials of reduced plastic anisotropy. *International Journal of Solids and Structures*, 138:24 – 39, 2018.

[32] A.-J. Wang and D. L. McDowell. In-Plane Stiffness and Yield Strength of Periodic Metal Honeycombs. *Journal of Engineering Materials and Technology*, 126(2):137–156, 2004.

[33] R.G. Hutchinson and N.A. Fleck. The structural performance of the periodic truss. *Journal of the Mechanics and Physics of Solids*, 54:756 – 782, 2006.

[34] Liang Dong, Vikram Deshpande, and Haydn Wadley. Mechanical response of ti–6al–4v octet-truss lattice structures. *International Journal of Solids and Structures*, 60-61, 2015.

[35] S. Lee, F. Barthelat, J.W. Hutchinson, and H.D. Espinosa. Dynamic failure of metallic pyramidal truss core materials – experiments and modeling. *International Journal of Plasticity*, 22:2118 – 2145, 2006.

[36] Nathan Wicks and John W Hutchinson. Optimal truss plates. *International Journal of Solids and Structures*, 38:5165 – 5183, 2001.

[37] N. A. Fleck, V. S. Deshpande, and M. F. Ashby. Reexamining the mechanical property space of three-dimensional lattice architectures. *Acta Materialia*, 140, 2017.

[38] Minh-Son Pham, Chen Liu, Iain Todd, and Jedsada Lertthanasarn. Damage-tolerant architected materials inspired by crystal microstructure. *Nature: International journal of science*, 565, 2019.

[39] C. L. Kane and T. C. Lubensky. Topological boundary modes in isostatic lattices. *Nature Physics*, 10:39–45, 2014.

[40] P.R. Onck, E.W. Andrews, and L.J. Gibson. Size effects in ductile cellular solids. Part I: modeling. *International Journal of Mechanical Sciences*, 43(3):681–699, dec 2001.

[41] E W Andrews, G Gioux, P Onck, and L J Gibson. Size effects in ductile cellular solids. Part II : experimental results. *International Journal of Mechanical Sciences*, 43:0–1, 2001.

[42] C. Chen, T.J. Lu, and N.A. Fleck. Effect of imperfections on the yielding of two-dimensional foams. *Journal of the Mechanics and Physics of Solids*, 47:2235 – 2272, 1999.

[43] Alan Arnold Griffith and Geoffrey Ingram Taylor. The phenomena of rupture and flow in solids. *Philosophical Transactions of the Royal Society of London. Series A, Containing Papers of a Mathematical or Physical Character*, 221, 1921.

[44] C. E. Inglis. Stresses in a plate due to the presence of cracks and sharp corners. *SPIE Milestone Series*, 137, 1913.

[45] G.R. Irwin. Analysis of stresses and strains near the end of a crack traversing a plate. *Journal of applied mechanics*, 24, 1957.

[46] H.M. Westergaard. Bearing pressures and cracks. *Journal of applied mechanics*, 6, 1939.

[47] M.L. Williams. On the stress distribution at the base of a stationary crack. *Journal of applied mechanics*, 24, 1957.

[48] H. P. Rossmanith. *Fracture research in retrospect: an anniversary volume in honour of G.R. Irwin's 90th birthday*. CRC Press, 2014.

[49] Hiroshi Tada George R.Irwin. *The Stress Analysis Of Cracks Handbook (Third Edition).pdf*. ASME Press, New York, third edition, 2000.

[50] M.L. Williams. T-stress effects in mixed mode i/ii/iii brittle fracture. *Engineering Fracture Mechanics*, 144, 2015.

[51] J. Y. Huang, J. S.and Lin. Mixed-mode fracture of brittle cellular materials. *Journal of Materials Science*, 31, 1996.

[52] I. Schmidt and N. A. Fleck. Ductile fracture of two-dimensional cellular structures. *International Journal of Fracture*, 111(4):327–342, 2001.

[53] I. Schmidt and N.A. Fleck. Ductile fracture of two-dimensional cellular structures. *International Journal of Fracture*, 111, 2014.

[54] ASTM E1820 - 18: Standard Test Method for Measurement of Fracture Toughness. *American Society for Testing and Materials*, 2019.

[55] Naomi E R Romijn and Norman A Fleck. The fracture toughness of planar lattices : Imperfection sensitivity. 55:2538–2564, 2007.

[56] I Quintana-alonso, S P Mai, N A Fleck, D C H Oakes, and M V Twigg. The fracture toughness of a cordierite square lattice. *Acta Materialia*, 58:201–207, 2010.

[57] Fabian Lipperman, Michael Ryvkin, and Moshe B Fuchs. Fracture toughness of two-dimensional cellular material with periodic microstructure. *International Journal of Fracture*, 146:279–290, 2007.

[58] Fabian Lipperman, Michael Ryvkin, and Moshe B. Fuchs. Nucleation of cracks in two-dimensional periodic cellular materials. *Computational Mechanics*, 39, 2007.

[59] G.D.Acharya Shubham V. Rupani, Shivang S. Jani. Design, modelling and manufacturing aspects of honeycomb sandwich structures: A review. *International Journal of Scientific Development and Research*, 2, 2017.

[60] Haydn N.G. Wadley, Norman A. Fleck, and Anthony G. Evans. Fabrication and structural performance of periodic cellular metal sandwich structures. *Composites Science and Technology*, 63:2331 – 2343, 2003.

[61] Lawrence E. Murr, Sara M. Gaytan, Diana A. Ramirez, Edwin Martinez, Jennifer Hernandez, Krista N. Amato, Patrick W. Shindo, Francisco R. Medina, and Ryan B. Wicker. Metal fabrication by additive manufacturing using laser and electron beam melting technologies. *Journal of Materials Science and Technology*, 28:1 – 14, 2012.

[62] Li Peng, Yang Taiping, Li Sheng, Liu Dongsheng, Hu Qianwu, Xiong Weihao, and Zeng Xiaoyan. Direct laser fabrication of nickel alloy samples. *International Journal of Machine Tools and Manufacture*, 45:1288 – 1294, 2005.

[63] Eleftherios Louvis, Peter Fox, and Christopher J. Sutcliffe. Selective laser melting of aluminium components. *Journal of Materials Processing Technology*, 211:275 – 284, 2011.

[64] Herzog D., Seyda V., Wycisk E., and Emmelmann C. Additive manufacturing of metals. *Acta Mater*, 117:371–392, 2016.

[65] Sri Kolla Prashanth Konda Gokuldoss and Jürgen Eckert. Additive manufacturing processes: Selective laser melting, electron beam melting and binder jetting—selection guidelines. *Materials (Basel)*, 10:672, 2017.

[66] Chunlei Qiu, Sheng Yue, Nicholas J.E. Adkins, Mark Ward, Hany Hassanin, Peter D. Lee, Philip J. Withers, and Moataz M. Attallah. Influence of processing conditions on strut structure and compressive properties of cellular lattice structures fabricated by selective laser melting. *Materials Science and Engineering: A*, 628:188 – 197, 2015.

[67] Ruben Wauthle, Bey Vrancken, Britt Beynaerts, Karl Jorissen, Jan Schrooten, Jean-Pierre Kruth, and Jan Van Humbeeck. Effects of build orientation and heat treatment on the microstructure and mechanical properties of selective laser melted ti6al4v lattice structures. *Additive Manufacturing*, 5:77 – 84, 2015.

[68] Hamza Alsalla, Liang Hao, and Christopher Smith. Fracture toughness and tensile strength of 316l stainless steel cellular lattice structures manufactured using the selective laser melting technique. *Materials Science and Engineering: A*, 5:1 – 6, 2016.

[69] Hashish M. A model for abrasive waterjet (awj) machining. *Journal of Engineering Materials and Technology*, 3, 1989.

[70] Y Ozcelik, M Gursel, R Ciccu, G Costa, and A Bortolussi. Optimization of working parameters of water jet cutting in terms of depth and width of cut. *Proceedings of the Institution of Mechanical Engineers, Part E: Journal of Process Mechanical Engineering*, 226, 2012.

[71] Jignesh K Patel and Abdulhafiz A Shaikh. The influence of abrasive water jet machine parameters on various responses - a review. *International journal of mechanical engineering and robotics research*, 4, 2015.

[72] Imetrum.2012. Video GaugeTM - How it works [ONLINE] Available at: https://www.imetrum.com/video-gauge/how-it-works/.

[73] J.J. Orteu Sutton, M. A. and H. W. Schreier. Image correlation for shape, motion and deformation measurements. *Springer*, 2009.

[74] I Quintana Alonso and N A Fleck. Damage tolerance of an elastic-brittle diamond-celled honeycomb. *Scripta Materialia*, 56:693–696, 2007.

[75] R.B. Fuller. Octet truss. u.s. *Patent No. 2,986,241.*, 1961.

[76] X. L. Wang and W. J. Stronge. Micropolar theory for two-dimensional stresses in elastic honeycomb. *Proceedings of the Royal Society of London. Series A: Mathematical, Physical and Engineering Sciences*, 455:2091–2116, 1999.

[77] S. Elangovan, B.S. Altan, and G.M. Odegard. An elastic micropolar mixture theory for predicting elastic properties of cellular materials. *Mechanics of Materials*, 40:602 – 615, 2008.

[78] M.L.M. François, L. Chen, and M. Coret. Elasticity and symmetry of triangular lattice materials. *International Journal of Solids and Structures*, 60-61:129, 2017.

[79] *ABAQUS/CAE user's manual : version 6.14.* ABAQUS.Inc., 2014.

[80] Inc UVP. Apparatus for production of three-dimensional objects by stereolithography. *Patent No. 4,575,330.*, 1984.

[81] Crivello James V. and Elsa Reichmanis. Photopolymer materials and processes for advanced technologies. *Chemistry of Materials Chem. Mater.*, 26, 2014.

[82] Eun-Dok Lee, Jae-Hyung Sim, Hyeog-Jun Kweon, and In-Hwan Paik. Determination of process parameters in stereolithography using neural network. *KSME International Journal*, 2004.

[83] Mohammad Taufik and Prashant K. Jain. Role of build orientation in layered manufacturing: A review. *International Journal of Manufacturing Technology and Management*, 27:47–71, 2014.

[84] Timoshenko S P and Gere J M. *Theory of Elastic Stability*. Mcgraw-Hill, second edition, 1961.

[85] ASTM E399 - 17 : Standard Test Method for Linear-Elastic Plane-Strain Fracture Toughness KIc of Metallic Materials. *American Society for Testing and Materials*, 2016.

[86] Huaiyuan Gu, Martyn Pavier, and Anton Shterenlikht. Experimental study of modulus, strength and toughness of 2d triangular lattices. *International Journal of Solids and Structures*, 152-153:207 – 216, 2018.

[87] J.P. Kruth, L. Froyen, J. Van Vaerenbergh, P. Mercelis, M. Rombouts, and B. Lauwers. Selective laser melting of iron-based powder. *Journal of Materials Processing Technology*, 149:616 – 622, 2004.

[88] Ruidi Li, Jinhui Liu, Yusheng Shi, Li Wang, and Wei Jiang. Balling behavior of stainless steel and nickel powder during selective laser melting process. *The International Journal of Advanced Manufacturing Technology*, 59, 2012.

[89] C. Y. Yap, C. K. Chua, Z. L. Dong, Z. H. Liu, D. Q. Zhang, L. E. Loh, and S. L. Sing. Review of selective laser melting: Materials and applications. *Applied Physics Reviews*, 2, 2015.

[90] Dongdong Gu and Yifu Shen. Balling phenomena in direct laser sintering of stainless steel powder: Metallurgical mechanisms and control methods. *Materials and Design*, 30, 2009.

[91] Ville-Pekka Matilainen, Heidi Piili, Antti Salminen, and Olli Nyrhilä. Preliminary investigation of keyhole phenomena during single layer fabrication in laser additive manufacturing of stainless steel. *15th Nordic Laser Materials Processing Conference*, 2, 2015.

[92] E.Herny, J.Rideau, and M. Attallah. Title of patent: Production of half-stages of monobloc stator guides by additive manufacturing. *2016-09-15*.

[93] Nesma Aboulkhair. *Additive manufacture of an aluminium alloy: processing, microstructure, and mechanical properties*. PhD thesis, 12 2015.

[94] Ivan Zuiko and Rustam Kaibyshev. Aging behavior of an al–cu–mg alloy. *Journal of Alloys and Compounds*, 759:108 – 119, 2018.

[95] J. F. Nie and B. C. Muddle. Microstructural design of high-strength aluminum alloys. *Journal of Phase Equilibria*, 19, 1998.

[96] Berberan-Santos, M. N. Beer's law revisited. *Journal of Chemical Education*, 67:757, 1990.

[97] Jiang Hsieh. *Computed Tomography: Principles, Design, Artifacts, and Recent Advances*. SPIE press, 2015.

[98] Avizo user guide. [ONLINE] Available at `https://assets.thermofisher.com/TFS-Assets/MSD/Product-Guides/user-guide-avizo-software.pdf`.

[99] Instron strain gauge extensometer product description 2017. [ONLINE] Available at `https://www.instron.us/en-us/products/testing-accessories/extensometers/axial-clip-on/static/2630-106`,.

[100] J. A. Choren, S. M. Heinrich, and M. B. Silver-Thorn. Young's modulus and volume porosity relationships for additive manufacturing applications. *Journal of Materials Science*, 48, 2013.

[101] M. Asmani and C. Kermel and A. Leriche and M. Ourak. Influence of porosity on young's modulus and poisson's ratio in alumina ceramics. *Journal of the European Ceramic Society*, 670:1081 – 1086, 2001.

[102] ASTM E561 - 17: Standard Test Method for KR Curve Determination. *American Society for Testing and Materials*, 2018.

[103] Instron extensometer product description 2017. [ONLINE] Available at `http://www.instron.se/sv-se`,.

[104] T.L.Anderson. *Fracture Mechanics: Fundamentals and Applications*. CRC Press, 4th edition, 2017.

[105] J.S. Huang and L.J. Gibson. Analysis of constraint in single edge notch tension specimens using the t-stress. *International Journal of Pressure Vessels and Piping*, 65(1):13 – 19, 1996.

[106] Xin Wang. Elastic t-stress for semi-elliptical surface cracks in finite thickness plates. 70:731–756, 04 2003.

[107] N. A. FLECK K. Y. G. McCULLOUGH and M. F. ASHBY. Toughness of aluminium alloy foams. *Acta Mater*, 47:2331–2343, 1999.